PACKED TUBULAR REACTOR MODELING AND CATALYST DESIGN USING COMPUTATIONAL FLUID DYNAMICS

Anthony G. Dixon[1], Michiel Nijemeisland[2] and E. Hugh Stitt[2]

[1]**Worcester Polytechnic Institute, Department of Chemical Engineering, Worcester, MA 01609, USA**
[2]**Johnson Matthey Catalysts, Billingham, Cleveland, UK**

Abstract

Computational fluid dynamics (CFD) is rapidly becoming a standard tool for the analysis of chemically reacting flows. For single-phase reactors, such as stirred tanks and "empty" tubes, it is already well-established. For multiphase reactors such as fixed beds, bubble columns, trickle beds and fluidized beds, its use is relatively new, and methods are still under development. The aim of this chapter is to present the application of CFD to the simulation of three-dimensional interstitial flow in packed tubes, with and without catalytic reaction. Although the use of

Advances in Chemical Engineering, vol. 31
ISSN 0065-2377
DOI: 10.1016/S0065-2377(06)31005-8

CFD to simulate such geometrically complex flows is too expensive and impractical currently for routine design and control of fixed-bed reactors, the real contribution of CFD in this area is to provide a more fundamental understanding of the transport and reaction phenomena in such reactors. CFD can supply the detailed three-dimensional velocity, species and temperature fields that are needed to improve engineering approaches. In particular, this chapter considers the development of CFD methods for packed tube simulation by finite element or finite volume solution of the governing partial differential equations. It discusses specific implementation problems of special relevance to packed tubes, presents the validation by experiment of CFD results, and reviews recent advances in the field in transport and reaction. Extended discussion is given of two topics: heat transfer in packed tubes and the design of catalyst particles for steam reforming.

I. Introduction

A. CFD and Packed Reactor Tube Modeling

The design of chemical reactors to make useful chemical products must be able to accommodate new catalysts, new feedstocks, and new product specifications, while facing ever-tighter economic, environmental, safety, and social acceptability constraints. The reactor designer must strive for higher yields, less energy use, smaller reactor capital costs, and other aspects of sustainable processing. To accomplish these objectives, the reactor designer must be able to understand, quantify, and control the individual chemical and physical phenomena present in reactors. An essential part of such a task is the development of predictive models of reactor behavior, based on the true representation of the physical and chemical processes that occur, on different length scales. Capturing the real physics and chemistry is especially important for heterogeneous reactors, such as gas–solid or liquid–solid fixed beds, and gas–liquid–solid trickle beds. It is necessary to know the spatial distribution of reactants, catalysts, inerts, and products in detail (Lerou and Ng, 1996).

A catalytic fixed bed reactor is a (usually) cylindrical tube that is randomly filled with porous catalyst particles. These are frequently spheres or cylindrical pellets, but other shapes are also possible. The use of rings or other forms of particles with internal voids or external shaping is on the increase. During single-phase operation, a gas or liquid flows through the tube and over the catalyst particles, and reactions take place on the surfaces, both interior and exterior, of the particles.

Single-phase catalytic fixed bed reactors are the main reactor type used for large-scale heterogeneously catalyzed gas-phase reactions. Frequently, multitubular

fixed beds with low tube-to-particle diameter ratio (N) are used for strongly exothermic reactions such as partial oxidations and selective hydrogenations as well as strongly endothermic reactions such as steam reforming of methane. In these processes heat must be rapidly transferred into or out of a narrow reactor tube, while the need to reduce compressor costs dictates a low pressure drop along the tube, and so the particle size cannot be too small. These constraints combine to give tubes with low values of N. The presence of the tube wall has a strong influence on heat transfer, reaction rates, and selectivity for these reactor tubes, which have proved to be exceptionally difficult to model.

Current fixed bed reactor models have been based on fairly strong simplifying assumptions, such as pseudo homogeneity, unidirectional plug flow, effective transport parameters, and uniform catalyst pellet surroundings. These simplifications have been motivated in the past by the need for computational savings, which continues to become less of an issue. The complex structure of random-packed tubes has also prompted a simplified approach. These idealized models have led, however, to problems. Even the most advanced models today cannot quantitatively predict reactor behavior if independently determined kinetics and transport parameters are used (Schouten *et al.*, 1994; Landon *et al.*, 1996). The effects of tube and catalyst pellet design changes are masked by the use of effective parameters and simplified models. Reaction engineers are in agreement that the entire field has neglected the role of fluid flow in reactor modeling. For fixed beds, a better understanding of fluid flow through arrays of realistic catalyst particle shapes would be of great help, with special attention to the problematical wall region. The presence of the tube wall causes changes in bed structure, flow patterns, transport rates, and the amount of catalyst per unit volume, and is usually the location of the limiting heat transfer resistance.

New techniques in experimentation and computation that allow us to understand and model fixed-bed phenomena at the particle or subparticle level are needed. The desire to measure fluid flow inside the bed has led several researchers to use noninvasive experimental methods. McGreavy *et al.* (1984, 1986) used laser Doppler velocimetry (LDV) in low-N packed beds, for both liquid and gas experiments, although only results using liquids were presented. Particle tracking methods were used by Rashidi *et al.* (1996) and also by Stephenson and Stewart (1986). The latter authors used marker bubbles as a noninvasive method to measure the radial distribution of flow of a matched-refractive index fluid in transparent packed beds of equilateral cylinders with $N = 10.7$. They found that the local superficial velocity attained its global maximum at $0.2d_p$ from the wall and its global minimum at $0.5d_p$ from the wall. Both studies found an oscillatory radial velocity profile. This type of profile was confirmed recently, again using LDV (Giese *et al.*, 1998), for a column with a tube-to-particle diameter ratio of approximately 9. Comparisons were made with the extended Brinkman model, and good agreement was obtained when an adjustable effective viscosity was introduced into the term for wall effects.

A noninvasive experimental method that has been used to obtain local flow patterns in fixed beds is magnetic resonance imaging (MRI). This method can show flow patterns in complicated geometries. The method has so far been restricted to relatively low flow rates, and to fluids that can produce a suitable signal for measurement, such as water. Gas flow has rarely been investigated by MRI techniques. Generally the packed beds used for MRI have had a considerably higher tube-to-particle diameter ratio, which will result in less pronounced wall effects. Qualitatively the MRI results show generally accepted flow concepts such as flow increase in bed voids, as well as inhomogeneous velocity distribution in different pores (Sederman *et al.*, 1997, 1998). The larger tube-to-particle diameter ratio also allows for a statistical view of the velocity distribution over the column cross section. When averaged over a long evolution time, the data approached Gaussian behavior (Park and Gibbs, 1999). With a tube-to-particle diameter ratio of 6.7 and relatively low flow rates, the velocity profile was roughly parabolic with the maximum being near the center of the tube. Also, negative velocities or reversed flow within the bed were shown (Kutsovsky *et al.*, 1996). Recent applications of the noninvasive MRI technique have been made by Suekane *et al.* (2003) to a cubic-packing fixed bed unit cell and by Yuen *et al.* (2002) to isothermal reacting flows. Ren *et al.* (2005) used NMR methods to obtain profiles of velocity in a narrow tube.

All these methods allow observations of flow inside the fixed bed without disturbing the bed structure and can thus further our understanding, but each is subject to severe limitations. LDV requires windows for optical access and is restricted to beds of very low N where such voids occur naturally. It also requires the fluid to be refractive-index-matched with the transparent material of the column. MR methods are mainly used for liquids, and techniques to allow imaging of fast flows are starting to appear (Gladden *et al.*, 2005). Particle tracking methods require observation and counting of the markers, and problems with choice of fluid similar to those with LDV are found. Experimental methods do not yet let us get to conditions of interest for fixed bed reactor design, i.e., gas-phase high flow rates at elevated temperatures with conduction and reaction in catalyst particles. While experimental techniques continue to improve, a complementary approach is to take advantage of the recent advances in scientific computing to simulate the flow fields. Computational fluid dynamics (CFD) has become a standard tool in the field of chemical engineering. The general setup of most CFD programs allows for a wide range of applications, and several commercial packages have introduced chemical reactions into the CFD code allowing rapid progress in the use of CFD within the field of chemical reaction engineering (Bode, 1994; Harris *et al.*, 1996; Kuipers and van Swaaij, 1998; Ranade, 2002).

The application of CFD to packed bed reactor modeling has usually involved the replacement of the actual packing structure with an effective continuum (Kvamsdal *et al.*, 1999; Pedernera *et al.*, 2003). Transport processes are then represented by lumped parameters for dispersion and heat transfer (Jakobsen

et al., 2002). The reactions that take place in the porous catalyst particles are represented by source or sink terms in the conservation equations (Ranade, 2002) and corrected for volume fraction and particle transport limitations. The velocity field can be obtained from a modified momentum balance (Bey and Eigenberger, 1997) or a form of the Brinkman-Forcheimer-extended Darcy (BFD) equation (Giese *et al.*, 1998). These approaches provide an averaged superficial velocity field, usually in the form of a radially varying axial component of velocity, which is an improvement over the classical assumption of plug flow (constant unidirectional flow). These velocity fields have been used in improved models of fixed bed transport and reaction (Winterberg *et al.*, 2000). The disadvantages of the BFD approach have been the continued lumping of transport processes, thus obscuring the physical basis of the model, and the necessity to introduce an effective viscosity for the bed to bring computed and experimental velocity profiles into agreement (Bey and Eigenberger, 1997; Giese *et al.*, 1998). This form of CFD in fixed beds is an extension of the classical pseudo-continuum approach, in which both fluid and solid phases are modeled as inter-penetrating continua, i.e., as if they coexisted at every point in the tube (Fig. 1a).

An alternative and complementary use of CFD in fixed bed simulation has been to solve the actual flow field between the particles (Fig. 1b). This approach does not simplify the geometrical complexities of the packing, or replace them by the pseudo-continuum that is used in the first approach. The governing equations for the interstitial fluid flow itself are solved directly. The contrast is thus between the interstitial flow field type of simulation and the superficial flow

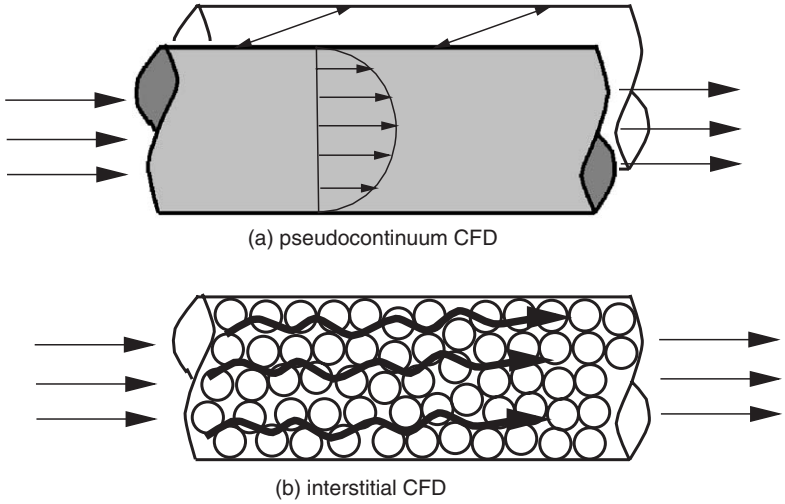

FIG. 1. Comparison of (a) pseudo-continuum and (b) interstitial CFD approaches to packed-tube simulation.

field models of the BFD approach (Tobiś, 2000). The equations of the interstitial approach are well established and relatively straightforward; however, the geometric modeling and grid generation become complicated and the computational demands rise significantly (Ranade, 2002). Owing to the computational requirements, the approach can so far be applied only to small, periodic regions of the reactor. It is therefore useful mainly as a learning tool, from which we can develop detailed insight into fixed bed flow structures and understand how they influence transport and reaction. The understanding from this more rigorous approach to CFD can then be used to inform the simplifying decisions made in the development of the more computationally tractable pseudo-continuum fixed bed models.

B. CFD Approaches to Interstitial Flow in Fixed Beds

The development of CFD calculations of interstitial flow in fixed beds has increased and become more realistic, as greater computational power has become more available over the recent years. Calculations of velocity and pressure profiles for creeping flow between spheres were done by Snyder and Stewart (1966) using Galerkin's method, followed by Sørensen and Stewart (1974) using specially designed collocation methods. They were able to obtain the velocity and temperature profiles in cubic arrays of spheres, a highly symmetric arrangement. Their calculations yielded insight into the behavior of the heat transfer coefficient for particle-to-fluid heat and mass transfer, over a wide range of values of the Peclet number $Pe = RePr$, where Re is the particle Reynolds number, based on superficial velocity ($\rho v_0 d_p/\mu$) and Pr is the Prandtl number ($\mu c_p/k_f$). Flow through cubic arrays of particles was also studied by Lahbabi and Chang (1985) by analytical methods, with focus on flow transitions.

Dalman *et al.* (1986) investigated flow around two spheres near a wall using two-dimensional (2D) finite element models in an axisymmetric radial plane. This study showed that eddies formed between the spheres, which led to regions of poor heat transfer. Lloyd and Boehm (1994) also did a 2D study, with eight spheres in line, to determine the influence of the sphere spacing on the drag coefficients and the particle-fluid heat transfer coefficient. A 3D finite element method was used by Mansoorzadeh *et al.* (1998) to simulate flow past a heated/cooled sphere at moderate Re. They found good agreement between calculated drag coefficients and a literature correlation, and that the axisymmetry of the wake flow broke down at Re = 400. Heat transfer from or to the sphere increased the drag coefficient at higher Re. It was found that heat transfer from the spheres decreased with decreased sphere spacing. McKenna *et al.* (1999) used discrete particle CFD to obtain valuable insight into the effect of particle size on particle-fluid heat transfer during olefin polymerization in a fluidized bed. They used a commercial code, Fluent, to conduct a 2D CFD study of small clusters of catalyst particles and a 3D study of a single catalyst sphere close to a

wall. They explored two ways to include the local energy effects of reaction. The first was by specifying a surface heat flux for systems of two touching particles or three particles with one small hot particle touching two larger, colder ones. Their second approach was to utilize a constant volumetric heat source in particles with solid conduction included, to allow for dilution of active sites and heat generation as the particle grows. Their main finding was that significant heat is removed from these particles by conduction, as well as the usually assumed path of convection.

Three-dimensional (3D) models have been developed more recently. A simple three-sphere model (Derkx and Dixon, 1996) focused on obtaining wall heat transfer coefficients. An eight-sphere model followed (Logtenberg and Dixon, 1998a, b) in which the packing was modeled as two layers of four spheres, perpendicular to the flow in a tube with a tube-to-particle diameter ratio of $N = 2.43$. This study was limited by the absence of contact points between the spheres and the wall and between the spheres themselves. Subsequently, a 3D 10-sphere model was developed, with $N = 2.68$, incorporating contact points between the particles and between the particles and the wall (Logtenberg *et al.*, 1999), which used spherical dead volumes with estimated diameters, around the contact points. These studies focused on using CFD to obtain the traditional radial heat transfer modeling parameters such as the wall heat-transfer coefficient (h_w) and the effective radial thermal conductivity (k_r), and gave reasonable qualitative agreement with experimental estimates. Other heat transfer work in fixed beds has explored the use of CFD to simulate flow and transport in structured packings (Von Scala *et al.*, 1999) and to investigate the effects of roughness gaps in particle–particle heat conduction (Lund *et al.*, 1999).

So far, there have only been a few modeling studies to try to link local fluid flow to bed structure. Chu and Ng (1989) and later Bryant *et al.* (1993) and Thompson and Fogler (1997) used network models for flow in packed beds. Different beds were established using a computer simulation method for creating a random bed. The model beds were then reduced to a network of pores, and either flow/pressure drop relations or Stokes' law was used to obtain a flow distribution.

Several groups have studied the connection between fluid flow and bed structure in complete particle beds. Esterl *et al.* (1998) and Debus *et al.* (1998) applied a computational code by Nirschl *et al.* (1995) to find flow profiles in a square channel, using an adapted chimera grid. This grid consisted of a structured grid, based on the flowing medium, which was overlaid by a separate structured grid, based on the packing particles. Calculated pressure drops were compared against predicted pressure drops using, amongst others, Ergun's relation for a bed with the same porosity; the simulation data gave the same order of magnitude. Simulations were performed in beds with up to 300 spheres, although the bed for which results were discussed consisted of 120 spheres. One of the aspects that may have affected the accuracy of the simulations is that the

bed was only approximately five layers deep, resulting in a flow that mainly consisted of inlet and outlet effects.

Still other research groups (Georgiadis *et al.*, 1996; Maier *et al.*, 1998; Manz *et al.*, 1999; Zeiser *et al.*, 2001) have used the lattice Boltzmann method (LBM) for simulation of flow in a fixed bed of spheres. A dense packing of spheres in a cylindrical column was created from experimental observations, such as MRI, or by computer simulation, for example by using a raining and compression algorithm. The created packing geometry was then divided into an equidistant Cartesian grid, where individual elements were labeled as solid or fluid regions as in a marker-and-cell approach. A high resolution of the grid made it possible to obtain accurate flow profiles. Recently (Zeiser *et al.*, 2002; Freund *et al.*, 2003; Yuen *et al.*, 2003) simple reactions have been added to the simulation, showing species and conversion profiles inside the bed. Limitations of the LBM are that simulations of turbulence are expensive, as the method corresponds to a direct numerical simulation (DNS) approach to the Navier-Stokes equations, and that it is difficult to include heat transfer. Incorporating heat transfer into fixed bed simulations is extremely challenging, due to the need to mesh and solve both convection in the voids and conduction in the particles. For LBM thermal models in the fluid, a multispeed approach must be used, usually from two to four speeds is feasible. Due to the small number of speeds, the variation in temperature is restricted. In addition, LBM methods are inherently transient and thus more computationally expensive than steady-state differential equation-based approaches, and they suffer from instability, which is worse for multispeed methods (Chen and Doolen, 1998).

A growing number of studies are appearing in which CFD methods are being used to simulate multi-physics flow and heat transfer at higher flow rates in fixed beds. Calis *et al.* (2001) applied the commercial code CFX-5.3 to a structured packing of spheres. They simulated flow in a number of channels of square cross-section filled with spherical particles. Several different types of structured packing were investigated, all based on structured packing of spheres. The repetitive sections had varying N, from 1 to 4. Values for pressure drop obtained from the simulations were validated against experimental values. The turbulence models used (k–ε and RSM) showed similar results, with an average error from the experimental values of about 10%. Pressure drop in a structured packing has also been studied by Larachi *et al.* (2003) and Petre *et al.* (2003), who used the Fluent CFD code to obtain flow fields that allowed them to construct submodels of different contributions to the overall pressure drop.

Pressure drop and dispersion were the focus of work by Magnico (2003) who simulated flow at lower Re by direct numerical simulation (DNS) in beds of spheres with an in-house code. Tobiś (2000) simulated a small cluster of four spheres with inserts between them to compare to his experimental measurements of pressure drop. Gunjal *et al.* (2005) also focused on flow and pressure drop through a small cell of spheres, in order to validate the CFD approach by comparison to the MRI measurements in the same geometry made by Suekane

et al. (2003). Romkes *et al.* (2003) extended the study of Calis *et al.* to include calculations for the heat transfer coefficient for a single sphere in an infinite medium, the wall heat transfer coefficient for laminar and turbulent flow in an empty tube, and the particle-to-fluid heat transfer coefficient in a packed tube. Heat transfer in full beds and bed segments has been the main focus of our own work (Dixon and Nijemeisland, 2001; Nijemeisland and Dixon, 2001, 2004) with special emphasis on flow patterns and heat transfer near the tube wall. Guardo *et al.* (2004, 2005) have performed similar calculations for pressure drop and wall heat transfer rates. Our most recent work has extended flow and heat transfer simulations to include source or sink terms in the solid particles, to emulate the energetic effects of reaction (Dixon *et al.*, 2003; Nijemeisland *et al.*, 2004). Several of these contributions will be discussed in more detail below.

The focus of the remainder of this chapter is on interstitial flow simulation by finite volume or finite element methods. These allow simulations at higher flow rates through turbulence models, and the inclusion of chemical reactions and heat transfer. In particular, the conjugate heat transfer problem of conduction inside the catalyst particles can be addressed with this method.

II. Principles of CFD for Packed-Tube Flow Simulation

A. CFD Basics and Turbulence Modeling

CFD may be loosely thought of as computational methods applied to the study of quantities that flow. This would include both methods that solve differential equations and finite automata methods that simulate the motion of fluid particles. We shall include both of these in our discussions of the applications of CFD to packed-tube simulation in Sections III and IV. For our purposes in the present section, we consider CFD to imply the numerical solution of the Navier–Stokes momentum equations and the energy and species balances. The differential forms of these balances are solved over a large number of control volumes. These small control volumes when properly combined form the entire flow geometry. The size and number of control volumes (mesh density) are user determined and together with the chosen discretization will influence the accuracy of the solutions. After boundary conditions have been implemented, the flow and energy balances are solved numerically; an iteration process decreases the error in the solution until a satisfactory result has been reached.

Commercially available CFD codes use one of the three basic spatial discretization methods: finite differences (FD), finite volumes (FV), or finite elements (FE). Earlier CFD codes used FD or FV methods and have been used in stress and flow problems. The major disadvantage of the FD method is that it is limited to structured grids, which are hard to apply to complex geometries and

are mostly used for stress calculations in beams, etc. A 3D structured grid results in a grid with all rectangular elements. The rectangular elements can undergo limited deformation to fit the geometry, but the adaptability of the grid is limited.

The FV and FE methods support both structured and unstructured grids, and therefore can be applied to a more complex geometry. An unstructured grid is a 2D structure of triangular cells or a 3D structure of tetrahedral cells, which is interpolated from user-defined node distributions on the surface edges or a triangular surface mesh, respectively. The interpolation part of the creation process is less directly influenced by the user in an unstructured mesh than in a structured mesh because of the random nature of the unstructured interpolation process. This aspect does however allow the mesh to adapt more easily to a complex geometry. The FE method is in general more accurate than the FV method, but the FV method uses a continuity balance per control volume, resulting in a more accurate mass balance. FV methods are more appropriate for flow situation, whereas FE methods are used more in stress and conduction calculations, where satisfying the local continuity is of less importance.

The equations for both laminar and turbulent flows, and the finite volume methods used to solve them, have been presented extensively in the literature (Patankar, 1980; Mathur and Murthy, 1997; Ranade, 2002; Fluent, 2003). The following summary focuses on aspects of particular concern for simulation of packed tubes and also those options chosen for our own work.

1. Navier–Stokes Equations

The general equation used for conservation of mass (the continuity equation) may be written as follows:

$$\frac{\partial \rho}{\partial t} + \frac{\partial (\rho u_i)}{\partial x_i} = S_m \tag{1}$$

The source term S_m contains the mass added through phase changes or user-defined sources. In general, and in the simulations described here, the source term was equal to zero.

The equation for conservation of momentum in direction i and in a non-accelerating reference frame is given by

$$\frac{\partial (\rho u_i)}{\partial t} + \frac{\partial (\rho u_i u_j)}{\partial x_j} = -\frac{\partial p}{\partial x_i} + \frac{\partial \tau_{ij}}{\partial x_j} + \rho g_i + F_i \tag{2}$$

In this balance p is the static pressure, τ_{ij} is the stress tensor, and ρg_i is the gravitational body force. F_i is an external body forces component; it can include forces from interaction between phases, centrifugal forces, Coriolis forces, and

user-defined sources. For single-phase flow through packed tubes it is usually zero. The stress tensor τ_{ij} for a Newtonian fluid is defined by

$$\tau_{ij} = \left[\mu\left(\frac{\partial u_i}{\partial x_j} + \frac{\partial u_j}{\partial x_i}\right)\right] - \frac{2}{3}\mu\frac{\partial u_l}{\partial x_l}\delta_{ij} \tag{3}$$

Here μ is the molecular viscosity; the second term on the right-hand side of the equation is the effect of volume dilation.

2. *RANS and the Standard k–ε Turbulence Model*

A time-dependent solution of the Navier–Stokes equations for high-Reynolds-number turbulent flows in complex geometries is currently beyond our computational capabilities. Two methods have been developed to transform the Navier–Stokes equations so that the small-scale turbulent fluctuations do not have to be directly simulated. These are Reynolds averaging (RANS) and filtering or Large-Eddy simulation (LES). Both methods introduce additional terms in the governing equations that need to be modeled in order to achieve closure. LES has not yet been applied to packed-tube modeling to any significant extent.

With RANS the solution variables in the Navier–Stokes equations are decomposed into mean, $\bar{u}_i$, and fluctuating u_i' components, and integrated over an interval of time large compared to the small-scale fluctuations. When this is applied to the standard Navier–Stokes equations (Eqs. (1)–(3)), the result is

$$\frac{\partial(\rho u_i)}{\partial t} + \frac{\partial(\rho u_i u_j)}{\partial x_j} = -\frac{\partial p}{\partial x_i} + \frac{\partial}{\partial x_j}\left[\mu\left(\frac{\partial u_i}{\partial x_j} + \frac{\partial u_j}{\partial x_i}\right) - \left(\frac{2}{3}\mu\frac{\partial u_l}{\partial x_l}\right)\right] + \frac{\partial(-\rho\overline{u_i'u_j'})}{\partial x_j} \tag{4}$$

The velocities and other solution variables are now represented by Reynolds-averaged values, and the effects of turbulence are represented by the "Reynolds stresses," $(-\rho\overline{u_i'u_j'})$ that are modeled by the Boussinesq hypothesis:

$$-\rho\overline{u_i'u_j'} = \mu_t\left(\frac{\partial u_i}{\partial x_j} + \frac{\partial u_j}{\partial x_i}\right) - \frac{2}{3}\left(\rho k + \mu_t\frac{\partial u_i}{\partial x_i}\right)\delta_{ij} \tag{5}$$

The k–ε turbulence model was developed and described by Launder and Spalding (1972). The turbulent viscosity, μ_t, is defined in terms of the turbulent kinetic energy, k, and its rate of dissipation, ε.

$$\mu_t = \rho C_\mu \frac{k^2}{\varepsilon} \tag{6}$$

The turbulent kinetic energy and its dissipation rate are obtained from the adapted transport equations.

$$\frac{\partial(\rho k)}{\partial t}+\frac{\partial(\rho u_i k)}{\partial x_i}=\frac{\partial}{\partial x_i}\left[\left(\mu+\frac{\mu_t}{\sigma_k}\right)\frac{\partial k}{\partial x_i}\right]+G_k+G_b-\rho\varepsilon \tag{7}$$

$$\frac{\partial(\rho\varepsilon)}{\partial t}+\frac{\partial(\rho u_i \varepsilon)}{\partial x_i}=\frac{\partial}{\partial x_i}\left[\left(\mu+\frac{\mu_t}{\sigma_\varepsilon}\right)\frac{\partial \varepsilon}{\partial x_i}\right]+C_{1\varepsilon}\frac{\varepsilon}{k}\left\{G_k+(1-C_{3\varepsilon})G_b\right\}-C_{2\varepsilon}\rho\frac{\varepsilon^2}{k} \tag{8}$$

In these equations, G_k is the generation of turbulent kinetic energy, k, due to turbulent stress, and is defined by

$$G_k=-\rho\overline{u_i' u_j'}\frac{\partial u_j}{\partial x_i} \tag{9}$$

G_b is the generation of turbulent kinetic energy, k, due to buoyancy,

$$G_b=\beta g_i\frac{\mu_t}{Pr_t}\frac{\partial T}{\partial x_i} \tag{10}$$

Here, Pr_t is the turbulent Prandtl number for temperature or enthalpy and β is the thermal expansion coefficient,

$$\beta=-\frac{1}{\rho}\left(\frac{\partial\rho}{\partial T}\right)_p \tag{11}$$

The default values of the constants $C_{1\varepsilon}=1.44$, $C_{2\varepsilon}=1.92$, $C_\mu=0.09$, $\sigma_k=1.0$, $\sigma_\varepsilon=1.3$, and $Pr_t=0.85$ have been established from experimental work with air and water, and have been found to work well for a wide range of wall-bounded and free shear flows (Launder and Spalding, 1972).

In a system with both heat and mass transfer, an extra turbulent factor, k_t, is included which is derived from an adapted energy equation, as were ε and k. The turbulent heat transfer is dictated by turbulent viscosity, μ_t, and the turbulent Prandtl number, Pr_t. Other effects that can be included in the turbulent model are buoyancy and compressibility.

The energy equation is solved in the form of a transport equation for static temperature. The temperature equation is obtained from the enthalpy equation, by taking the temperature as a dependent variable. The enthalpy equation is defined as,

$$\frac{\partial(\rho h)}{\partial t}+\frac{\partial(\rho u_i h)}{\partial x_i}=\frac{\partial}{\partial x_i}(\lambda+\lambda_t)\frac{\partial T}{\partial x_i}-\frac{\partial\sum_j h_j J_j}{\partial x_i}+\frac{Dp}{Dt}+(\tau_{ik})_{\text{eff}}\frac{\partial u_i}{\partial x_k}+S_h \tag{12}$$

In this equation S_h includes heat of chemical reaction, any interphase exchange of heat, and any other user-defined volumetric heat sources. λ_t is defined as the thermal conductivity due to turbulent transport, and is obtained from the turbulent Prandtl number

$$\lambda_t = \frac{c_p \mu_t}{Pr_t} \tag{13}$$

The enthalpy h is defined as

$$h = \sum_j Y_j h_j \tag{14}$$

where Y_j is the mass fraction of species j and,

$$h_j = \int_{T_{ref}}^{T} c_{p,j} dT \tag{15}$$

For problems involving gradients in chemical species, the convection-diffusion equations for the species are also solved, usually for $N-1$ species with the Nth species obtained by forcing the mass fractions to sum to unity. Turbulence can be described by a turbulent diffusivity and a turbulent Schmidt number, Sc_t, analogous to the heat transfer case.

3. *Alternative Turbulence Models*

The Reynolds-averaged approach is widely used for engineering calculations, and typically includes models such as Spalart–Allmaras, $k-\varepsilon$ and its variants, $k-\omega$, and the Reynolds stress model (RSM). The Boussinesq hypothesis, which assumes μ_t to be an isotropic scalar quantity, is used in the Spalart–Allmaras model, the $k-\varepsilon$ models, and the $k-\omega$ models. The advantage of this approach is the relatively low computational cost associated with the computation of the turbulent viscosity, μ_t. For the Spalart–Allmaras model, one additional transport equation representing turbulent viscosity is solved. In the case of the $k-\varepsilon$ and $k-\omega$ models, two additional transport equations for the turbulence kinetic energy, k, and either the turbulence dissipation rate, ε, or the specific dissipation rate, ω, are solved, and μ_t is computed as a function of k and either ε or ω. Alternatively, in the RSM approach, transport equations can be solved for each of the terms in the Reynolds stress tensor. An additional scale-determining equation (usually for ε) is also required. This means that seven additional transport equations must be solved in 3D flows.

Our group has made extensive use of the RNG $k-\varepsilon$ model (Nijemeisland and Dixon, 2004), which is derived from the instantaneous Navier–Stokes equations using the Renormalization Group method (Yakhot and Orszag, 1986) as opposed to the standard $k-\varepsilon$ model, which is based on Reynolds averaging. The

major differences, in application, from the standard k–ε model are different empirical constants in the k and ε balances and extra terms in the turbulent dissipation balance (ε). The Renormalization group methods are a general methodology of model building based on the stepwise coarsening of a problem. The main idea is that the RNG theory is applicable to scale-invariant phenomena that do not have externally imposed characteristic length and time scales. In the case of turbulence, the RNG theory is applicable to the small-scale eddies, which are independent of the larger scale phenomena that create them.

The RNG theory as applied to turbulence reduces the Reynolds number to an effective Reynolds number (Re_{eff}) by increasing an effective viscosity (μ_{eff}). Through this process the small-scale eddies are eliminated, which reduces computational demand considerably. The new equation for the variation of the effective viscosity is as follows:

$$\mu_{eff}(\ell) = \mu_{\text{mol}}\left[1 + \frac{3A\varepsilon}{4\mu_{\text{mol}}^3}(\ell^4 - \ell_d^4)\right]^{1/3} \quad (\ell \geq \ell_d) \tag{16}$$

where A is a constant derived by the RNG theory, ℓ is the eddy length scale, and ℓ_{d} is the Kolmogorov dissipation scale. So in this case when the eddy length scale is the Kolmogorov scale, the effective viscosity is the molecular viscosity. This equation then gives the interpolation formula for $\mu_{\text{eff}}(\ell)$ between the molecular viscosity μ_{mol} valid at dissipation scales and the high Reynolds number limit $L \gg \ell_{\text{d}}$.

Using the definition for the turbulent viscosity ($\mu_{\text{t}} = \mu_{\text{eff}} - \mu_{\text{mol}}$), which gives a result similar to the standard k–ε model with only a small difference in the modeling constant, the effective viscosity is now defined as a function of k and ε in Eq. (16) in algebraic form.

$$\mu_{\text{eff}} = \mu_{\text{mol}}\left[1 + \sqrt{\frac{C_\mu}{\mu_{\text{mol}}}}\frac{k}{\sqrt{\varepsilon}}\right]^2 \tag{17}$$

The differential form of this equation is used in calculating the effective viscosity in the RNG k–ε model. This method allows varying the effective viscosity with the effective Reynolds number to accurately extend the model to low-Reynolds-number and near-wall flows.

The transport equations for the turbulent kinetic energy, k, and the turbulence dissipation, ε, in the RNG k–ε model are again defined similar to the standard k–ε model, now utilizing the effective viscosity defined through the RNG theory. The major difference in the RNG k–ε model from the standard k–ε model can be found in the ε balance where a new source term appears, which is a function of both k and ε. The new term in the RNG k–ε model makes the turbulence in this model sensitive to the mean rate of strain. The result is a model that responds to the effect of strain and the effect of streamline curvature,

a feature that is nonexistent in the standard k–ε model. The inclusion of this effect makes the RNG k–ε model more suitable for complex flows.

The RNG model provides its own energy balance, which is based on the energy balance of the standard k–ε model with similar changes as for the k and ε balances. The RNG k–ε model energy balance is defined as a transport equation for enthalpy. There are four contributions to the total change in enthalpy: the temperature gradient, the total pressure differential, the internal stress, and the source term, including contributions from reaction, etc. In the traditional turbulent heat transfer model, the Prandtl number is fixed and user-defined; the RNG model treats it as a variable dependent on the turbulent viscosity. It was found experimentally that the turbulent Prandtl number is indeed a function of the molecular Prandtl number and the viscosity (Kays, 1994).

Guardo *et al.* (2004, 2005) have compared various turbulence models for a four-layer packed tube with $N = 3.92$ containing 44 spheres. In their first report (Guardo *et al.*, 2004) they compared laminar, standard k–ε, and Spalart–Allmaras models, and in the follow-up work (Guardo *et al.*, 2005) they extended this to cover the Spalart–Allmaras, standard k–ε, RNG k–ε, and realizable k–ε and k–ω models. Based on comparisons of computed pressure drop to the predictions of the Ergun equation, they conclude that the Spalart–Allmaras equation is preferable. This is explained by the fact that it is formulated to be valid all the way to solid surfaces, thus avoiding problems with wall functions (discussed below). Our comparisons of the standard k–ε, RNG k–ε, and RSM models (Nijemeisland and Dixon, 2001) showed that there were no significant differences in the results. Similar results for their geometry were found by Calis *et al.* (2001). The RNG k–ε model was chosen in our work because it deals better with flow with high streamline curvature and high strain rates, such as would be expected in packed tubes.

4. *Wall Functions*

Turbulent flows in packed tubes are strongly influenced by the solid surfaces, both the tube wall and the surfaces of the packing. Collectively, solid surfaces are referred to as "walls" in the CFD literature, and in this section we will continue that tradition. Besides the no-slip boundary condition on the velocity components that has to be satisfied, the turbulence is also changed by the presence of the wall. Very close to the wall, the tangential velocity fluctuations are reduced by viscous damping and the normal fluctuations are reduced by kinematic blocking. In the outer part of the near-wall region, in contrast, turbulence is increased by the production of turbulence kinetic energy due to the large gradients in mean velocity.

The near-wall region is conceptually subdivided into three layers, based on experimental evidence. The innermost layer is the viscous sublayer in which the flow is almost laminar, and the molecular viscosity plays a dominant role. The outer layer is considered to be fully turbulent. The buffer layer lies between

the viscous sublayer and the fully turbulent layer, and the effects of molecular viscosity and turbulence are equally important. To numerically resolve a solution in the sublayer requires a very fine mesh, since the sublayer is thin and gradients there are large. Models that are modified to enable the viscosity-affected region to be resolved with a mesh all the way to the wall, including the viscous sublayer such as the Spalart–Allmaras and k–ω models, are termed low-Reynolds number models.

To save computational effort, high-Reynolds number models, such as k–ε and its variants, are coupled with an approach in which the viscosity-affected inner region (viscous sublayer and buffer layer) are not resolved. Instead, semiempirical formulas called "wall functions" are used to bridge the viscosity-affected region between the wall and the fully turbulent region. The two approaches to the sublayer problem are depicted schematically in Fig. 2 (Fluent, 2003).

The standard wall function (Launder and Spalding, 1974) has been widely used for industrial flows. The wall function is based on the assumption that the velocity obeys the log law-of-the-wall

$$U^* = \frac{1}{\kappa}\ln(Ey^*) \tag{18}$$

where

$$U^* \equiv \frac{U_P C_\mu^{1/4} k_P^{1/2}}{\tau_w/\rho} \tag{19}$$

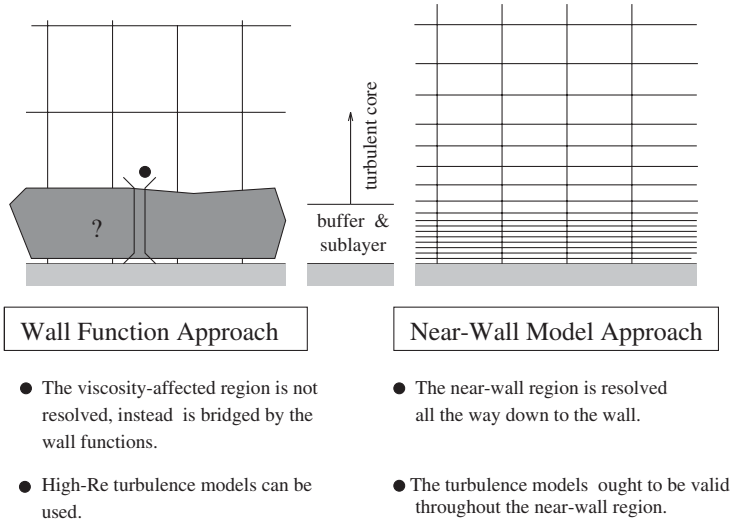

FIG. 2. Near-wall treatments (reproduced from Fluent Inc., Version 6.1 Manual, 2003, by permission).

$$y^* \equiv \frac{C_\mu^{1/4} k_P^{1/2} y_P}{\nu} \tag{20}$$

and κ and E are universal constants, and U_P is the mean velocity at P, the centroid of the cell next to the wall, and y_P is the distance of point P from the wall. We shall follow the original reference and present the wall functions in terms of y^* and U^*, although the usual notation in the turbulence field is to use $y^+ \equiv \frac{\sqrt{\tau_w/\rho}\, y_P}{\nu}$ and $U^+ \equiv \frac{U_P}{\sqrt{\tau_w/\rho}}$.

It is important to place the first near-wall grid node far enough away from the wall at y_P to be in the fully turbulent inner region, where the log law-of-the-wall is valid. This usually means that we need $y^* > 30$–60 for the wall-adjacent cells, for the use of wall functions to be valid. If the first mesh point is unavoidably located in the viscous sublayer, then one simple approach (Fluent, 2003) is to extend the log-law region down to $y^* = 11.225$ and to apply the laminar stress–strain relationship: $U^* = y^*$ for $y^* < 11.225$. Results from near-wall meshes that are very fine using wall functions are not reliable.

The heat flux to the wall and the wall temperature are related through a wall function

$$\frac{(T_w - T_P)\rho c_p C_\mu^{0.25} k_P^{0.5}}{\dot{q}_w''} = Pr_t\left[\tfrac{1}{\kappa}\ln(Ey^*) + P\right] + \tfrac{1}{2}\rho Pr \frac{C_\mu^{0.25} k_P^{0.5}}{\dot{q}_w''}\left\{Pr_t U_P^2 + (Pr - Pr_t)U_c^2\right\} \tag{21}$$

where P can be computed using (Launder and Spalding, 1974)

$$P = \frac{\pi/4}{\sin(\pi/4)}\left(\frac{A}{\kappa}\right)^{0.5}\left(\frac{Pr}{Pr_t} - 1\right)\left(\frac{Pr_t}{Pr}\right)^{0.24} \tag{22}$$

where T_P is the temperature at the cell adjacent to the wall, T_w is the temperature at the wall, Pr_t is the turbulent Prandtl number, U_c is the mean velocity magnitude at the edge of the thermal conduction layer, and A, κ and E are universal constants. An analogous approach is used for species transport.

The standard wall function is of limited applicability, being restricted to cases of near-wall turbulence in local equilibrium. Especially the constant shear stress and the local equilibrium assumptions restrict the universality of the standard wall functions. The local equilibrium assumption states that the turbulence kinetic energy production and dissipation are equal in the wall-bounded control volumes. In cases where there is a strong pressure gradient near the wall (increased shear stress) or the flow does not satisfy the local equilibrium condition an alternate model, the nonequilibrium model, is recommended (Kim and Choudhury, 1995). In the nonequilibrium wall function the heat transfer procedure remains exactly the same, but the mean velocity is made more sensitive to pressure gradient effects.

Apart from refinements to the standard wall function approach, such as the nonequilibrium model, there has been little progress in the 30 years since its first development. Craft *et al.* (2002) have suggested that this is because those who work on fundamental phenomena in the near-wall region regard any wall functions as a basically inadequate approach, whereas for industrial applications for which resolution of the boundary layer is usually impractical, the more advanced wall functions have not given clearly better results than the simpler original formulation. More recently, there has been a renewed interest in developing improved wall functions, based on sub-grid models of the near-wall cell (Craft *et al.*, 2002) or on analytical integration of simplified boundary-layer equations to get profiles to be used in the near-wall cell (Utyuzhnikov, 2005). The development of improved wall function treatments, especially for situations where the near-wall node must be located in the "buffer" region, will be of great importance to the application of CFD to packed tubes, as will be further discussed below in the context of mesh generation. An "enhanced wall function" option that uses blending functions to obtain a single equation valid for all three near-wall layers has been developed in Fluent, but has yet to be extensively tested for packed-tube flows.

5. *Finite Volume Methods and Codes*

There is considerable difference of opinion in the CFD research community regarding the use of commercial CFD codes versus the development of in-house code. The main advantage of the latter is that the user has complete control of the code, and can modify it as he/she sees fit. This approach is therefore essential for those whose research is directed toward the development of improved turbulence models, wall functions, or numerical algorithms. The downside of the in-house code is that it is usually restricted to specialized, if not simple, computational domains, and that post-processing and visualization facilities are usually primitive, in the absence of a third-party post-processing package. When the research is directed more toward the use of CFD methods to obtain insight or detailed information about a complex geometry such as a packed tube, the mesh generation and post-processing facilities available in commercial codes can be invaluable. Some of the commercial codes that have been used for packed-tube simulations are those by Fluent Inc. (FLUENT, FIDAP), ANSYS, Inc. (CFX), and Computational dynamics, Ltd. (Star-CD). Other codes that are often used originate in the governmental or academic sectors, e.g., CFDLIB from Sandia National Labs and PHOENICS, which is available as both shareware and commercially from Simuserve Ltd. CFD codes, can be modified to include extra terms, such as the Ergun terms for porous regions (Tierney *et al.*, 1998). Some have interfaces for user-defined code (e.g., FLUENT) while others make the original source code available (e.g., CFDLIB).

The two main approaches to CFD for packed-tube simulations have been LBM and FV methods. The LBM codes are in-house codes; the methods behind

them are well described in Chen and Doolen (1998) and are beyond the scope of this chapter. FV methods that directly discretized the Navier–Stokes equations have been extensively described by Patankar (1980), Mathur and Murthy (1997), and Ranade (2002). Briefly, the governing equations are integrated over control volumes to obtain discrete algebraic equations that conserve the quantity on the control volume. Variables are stored on a collocated grid with a local pressure gradient correction. The pressure–velocity coupling is achieved by the SIMPLE or the SIMPLEC scheme, and the equations are stabilized by underrelaxation. Second-order centered differences are used for spatial discretization of the viscous terms, while interpolation of face values from cell center values is done by first- or second-order upwind differences for the convective terms. The equations are solved iteratively, and either the energy equation can be a part of the main iteration in a coupled calculation or the flow field can be calculated first and then substituted into the energy equation in a segregated calculation. The solution of the large sets of algebraic equations is carried out by multigrid schemes, to accelerate convergence by computing corrections on a series of coarse grid levels. This is particularly important for unstructured meshes, as the line iterative methods used for structured meshes are unavailable. Multigrid methods use the property that on coarse meshes the global error can be reduced quickly, while on fine meshes the local error can be reduced by fine-grid relaxation schemes. Further details of the computational methods may be found in standard references, and are not repeated here as our focus is on the use and specialization of CFD methods for packed tubes, and the issues arising from this application area.

B. Packed Bed CFD Model Development

To create a useful CFD simulation the model geometry needs to be defined and the proper boundary conditions applied. Defining the geometry for a CFD simulation of a packed tube implies being able to specify the exact position and, for nonspherical particles, orientation of every particle in the bed. This is not an easy task. Our experience with different types of experimental approaches has convinced us that they are all too inaccurate for use with CFD models. This leads to the conclusion that the tube packing must either be computer-generated or be highly structured so that the particle positions can be calculated analytically.

Some groups have worked with models of unit cells of periodic repeating packing, such as cubical or rhombohedral, which are representative of the bed far from the containing walls (Tobiś, 2000; Gunjal *et al.*, 2005). Others have developed models of complete tube cross-sections in relatively short-axial segments of tubes with low enough N to be completely structured, for example $N = 2$ (Nijemeisland and Dixon, 2001) and $1 \leq N \leq 2$ in a square cross-section channel (Calis *et al.*, 2001). Several groups used computer-generated packings,

at $N = 7$ (Esterl *et al.*, 1998) and at $N = 2.42$ and $N = 4$ in square channels (Calis *et al.*, 2001) and at $N = 5.96$ and $N = 7.8$ in circular tubes (Magnico, 2003). Others used various *ad hoc* methods based on a combination of structure and experimental observation to guide model development for $N = 4$ (Dixon and Nijemeisland, 2001) and $N = 3.92$ (Guardo *et al.*, 2004, 2005). In this section we briefly review and illustrate some of these approaches, including our wall-segment (WS) approach that aims to retain the essential near-wall phenomena in a reduced-size model.

1. *Computer-generated Packed Tubes*

The geometric complexity of random-fixed bed structures has usually been handled by a statistical description of the geometry, in terms of void fraction profiles and pore size distributions. This approach gives a practical way to implement bed structure into the flow model by retaining the statistical characteristics of the void space without having to introduce the real void structure, since that is complicated and its 3D structure will vary with repacking (Jiang *et al.*, 2002). For CFD simulation, however, the exact structure of a particular instance of the bed must be known. For truly random large-N beds, the CFD results would then have value only if averaged over an ensemble of realizations of the possible bed structures.

For low-N packed tubes, a different point of view can be taken. The packing of such tubes is quite far from random, as the ordering of the particles imposed by the tube walls can extend from two- to five-particle diameters into the packing. In addition, the packing of the particles against the tube wall results in a small number of repeatable structures. Thus, if the focus of the research is the phenomena in the near-wall region, then CFD simulations in quite-structured arrays of particles can be regarded as a good representation of the full-size tube. The advantage of computer generation of such arrays is that we get complete information on the position and orientation of the particles, with high accuracy.

The drawbacks of the routine use of computer-generated packs are as follows: several algorithms do not allow for the influence of containing walls or require such walls to be planar (rectangular ducts); few algorithms exist for nonspherical particles; it is difficult to generate dense or loose packing as required, and a particular algorithm usually gives one or the other case; and validation of the computer results still requires some development. Despite these problems, packing algorithms are being used to provide geometric models for CFD simulations. Some of these instances are reviewed in this section, along with some of the more recent advances in computer generation algorithms.

The approaches to computer-generated packings have been classified into two main classes (Liu and Thompson, 2000): sequential deposition (SD) and collective rearrangement (CR). Typical of SD are the drop-and-roll algorithms, in which particles are added one by one to the packing and allowed to move until they find a gravitationally stable position. These algorithms usually result

in loose packings of porosity $\varepsilon = 0.42$ or higher. The CR algorithms (sometimes called Monte Carlo methods) typically begin with a prescribed number of particles that are moved randomly to either eliminate overlaps if the initial arrangement allowed them, or decrease voidage if the initial arrangement was nonoverlapping. A prescribed voidage can often be achieved, but it may be at some considerable computational cost.

It is also possible to classify the algorithms by whether the container is rectangular or cylindrical, and by whether the particles are spherical or nonspherical. One of the earliest algorithms that has been used for CFD geometry generation is an SD method for spheres in rectangular ducts (Chan and Ng, 1986), which was used by Esterl *et al.* (1998) and Debus *et al.* (1998). Soppe (1990) used a hybrid method, combining the raining technique and Monte Carlo rearrangement, again for spheres in a rectangular duct. This method was adapted by Freund *et al.* (2003) on a 3D equidistant orthogonal lattice to give packings of spheres with $1.1 < N < 20.3$. Reyes and Iglesia (1991) also used an SD algorithm for slow settling of hard spheres, but extended the methodology to cylindrical container walls and arbitrary-size distributions of spheres. Nolan and Kavanagh (1992) developed a CR algorithm for spheres in a cylinder, and then extended it to nonspherical particles (Nolan and Kavanagh, 1995) by representing arbitrary shapes as assemblies of component spheres with varying size distributions. Spedding and Spencer (1995) used SD for spherical packings in cylinders with no edge effects, since N was equal to 50 in their simulations of liquid rivulet flow over spheres.

Periodic boundary conditions for the walls were used by Yang *et al.* (1996) who wanted an efficient method for large numbers of random-size spheres packed into a hexahedral domain. They used a hybrid algorithm with random placement to generate the initial distribution of spheres and rearrangement to stable positions via a drop-and-roll procedure to eliminate overlaps. Liu and Thompson (2000) studied the extent to which the choice of boundary conditions affected internal-packing structure for spheres in rectangular ducts in CR algorithms. They found that even with periodic boundaries, intended to remove structure from the packings, CR algorithms could induce a self-assembly process that resulted in packings with ordered structures.

Mueller (1997) paid particular attention to wall effects in his use of an SD method for spheres in cylindrical tubes. His algorithm starts with a base layer of spheres, and then adds each new sphere to one of the two different types of positions, wall sphere positions and inner sphere positions, maintaining stability under gravity. He compared different procedures for determining the next site for addition of a new sphere. Best results were obtained when spheres were added to the lowest vertical positions of the two types of positions according to a set percentage. A more recent refinement of the method (Mueller, 2005) uses a packing parameter for the layers above the base layer, and gave good agreement with experimental voidage profiles for $2 \leq N \leq 20$. Mueller's approach seems to be the most useful for generating packed tubes of spheres at low N for CFD

simulations, and it was adopted by Magnico (2003) for his simulations at $N = 5.96$ and $N = 7.8$. Maier *et al.* (1998) used a CR technique to generate spherical bead packs in cylinders with nonpermeable walls and rectilinear domains with periodic boundaries, which they then used in their own, lattice Boltzmann simulations.

Nonspherical particle packings present more difficulties than spherical ones and have thus received less attention. Notable efforts have been made by Nandakumar *et al.* (1999) and Jia and Williams (2001). Nandakumar *et al.* (1999) represented arbitrary packing objects by a 3D polygonal model with a set of triangular surfaces. Their method did not simulate the dynamics of the packing process, but rather sought stable equilibrium positions for the objects using a collision detection algorithm. They obtained good agreement with experimental data for packings of spheres, Raschig rings and Pall rings. Jia and Williams (2001) took a completely different, digital approach, in which both particle shapes and packing space were digitized. Shapes could be represented by a collection of pixels (in 2D) and particles moved in random directions on a square lattice, with higher probability of moving "down" to simulate the gravity-induced packing process. Extensions to 3D and mixed particle sizes have been reported by Caulkin *et al.* (2006). Finally, Theuerkauf *et al.* (2006) reported on the use of the discrete element method (DEM) to generate packing structures in packed beds of spheres for use in CFD modeling, for low-N beds. DEM is a well-established method that uses particle mechanical properties to influence a final packing structure during a settling/deposition type process. The particles can be of arbitrary shape, and a soft contact approach is used, which allows particles to overlap during the process. The authors used a commercial DEM code, and have presented results on packings of cylinders by DEM in conferences. This appears to be a very promising method, which was validated by comparison to experimental radial voidage profiles.

2. *Complete Wall Models of Packed Tubes*

In packed beds with regular particles, such as spheres, several packing structures can be identified. First, a wall-induced structure is regularly found, in which the spheres arrange themselves along the wall in staggered rings (Mueller, 1997). A dense sphere packing can be identified in the center of the bed, when this is located far enough from the wall. The third structure is a more random transition between the very regular wall and center structures. In the literature, the majority of research is directed toward determining where the transition from the wall-induced structure to the central structure takes place. This is important when a radial porosity profile is used in modeling, in order to determine when to use the bed average porosity value. Generally, it is concluded that the effect of the wall has dissipated at about four particle diameters from the wall (Benenati and Brosilow, 1962) with only minimal contribution at about two particle diameters from the wall (Schuster and Vortmeyer, 1981).

In beds with very high N, the central structure will dominate throughout the bed. In low-N beds the wall-induced structure will dominate as the influence of the wall on the structure penetrates relatively deep into the bed. As an example, consider a tube with a diameter of 100, in arbitrary units, and two different spherical packing materials with diameters of 10 ($N = 10$) and 1 ($N = 100$); further assume that the wall-induced structure is recognizable as such for four layers of spheres from the wall. In the $N = 10$ bed the first four layers at the wall occupy 96 volume % of the bed. In the $N = 100$ bed, the wall-influenced region only makes up 15.6 volume % of the bed.

Once the structure of the bed is understood, it must be implemented as a computational geometry. For this the exact positions of the spheres must be established so that they can be placed in the CFD simulation geometry. For the $N = 4$ bed that we studied (Dixon and Nijemeisland, 2001) there was a regular structure in the bed, which made it possible to obtain the sphere locations using geometric relations. The geometry layout was divided into a nine-sphere wall induced structure and a three-sphere central structure. The nine-sphere wall layer was redistributed regularly along the wall. The specific tube-to-particle diameter ratio allowed for an almost exact fit of nine spheres along the tube wall, as shown in Fig. 3.

All the spheres in a layer were supported by two spheres of the layer below and the column wall, creating a stable packing structure. As the tube-to-particle diameter ratio of the bed was only four, the entire packing structure was controlled by the influence of the wall. Nevertheless, the packing was divided into an immediate wall layer and a central section, but this should not be taken to imply that the central structure was not wall influenced. Although a three-sphere planar structure would almost fit within the nine-sphere wall layer, there was just not enough room at the same axial coordinate. When, however, the

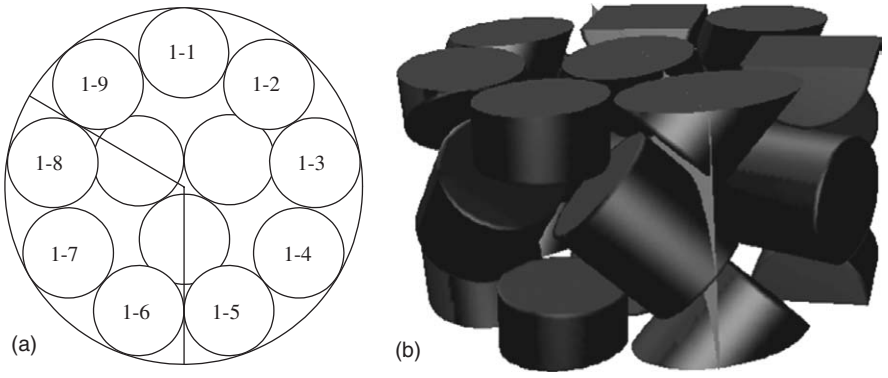

FIG. 3. Complete wall $N = 4$ geometries: (a) top view of a layer of spheres, with nine wall spheres marked, showing, three spheres in the center region; (b) perspective view of the two-layer full bed of cylinders.

axial coordinate of this three-sphere structure was located between two nine-sphere wall layers, there was enough room. It was eventually found that the three-sphere central stacking was supported by the nine-sphere wall layers. The additional spacing in the central structure results in identical layer spacing of both the nine-sphere wall layers and the three-sphere center layers, creating a stable overall structure. The three-sphere central structure was a spiral repetitive structure in which spheres were supported by only one sphere from the central structure and two spheres from the wall structure. The spiral nature of the structure necessitated a larger overall bed, to be able to accommodate periodic boundaries. The spiral needed six layers for the central layer spheres to return to their original positions; therefore, the full-bed model had to be made over six layers, or 72 spheres in total.

More recently, we have created full-bed periodic two-layer models for packings of cylindrical particles (Taskin *et al.*, 2006). The geometry shown in Fig. 3b was created specifically for comparison of the WS model with cylindrical particles described in the following section, with the structures identical within a 120° segment of the bed.

3. *Wall Segments*

Experience in CFD modeling in packed tubes has taught us that the number of control volumes increases rapidly with the increasing size of the geometry. To be able to solve for certain details in the model, such as areas where particles in the packing touch each other or the tube wall, a high level of detail is necessary for the required accuracy of the simulation. More particles in a model simulation will lead to more high-detail areas, increasing the computational size of a complete-wall, full-bed simulation very quickly.

This led us to the conclusion that we needed to formulate a model that focused on a small number of catalyst particles and their direct neighbors, for an accurate description of the heat transfer and flow processes taking place on the local scale. The near-wall region is the most interesting area since this is where the largest heat transfer gradient occurs. A smaller model was needed with representative particle and periodic boundaries so that it could be compared with any near-wall position in the full-bed geometry. The cylindrical shape of the geometry pointed to the use of a wedge-shaped segment. A WS consisting of a third of the tube circumference (120° segment) and two axial layers of particles would allow for appropriate detail throughout the simulation geometry. The relationship of the WS to the complete wall geometry is shown in Fig. 3. Within the WS geometry an appropriately large buffer zone around the area of interest was used to limit the effects of the boundary conditions on the flow properties in that area. The smaller WS geometry also gave us the freedom to adjust the mesh density to the requirements of the different packing situations.

The major added difficulty of this approach was the addition of several new boundaries on which appropriate boundary conditions had to be implemented.

The most important parts of creating a segment model are the application of the physical boundary conditions and the positioning of the internals to allow for the symmetry and periodic boundary conditions. Without properly applying boundary conditions the simulation results cannot be compared to full-bed results, both as a concept and as a validation, since the segment now is not really a part of a continuous geometry. Our approach was to apply symmetry boundaries on the side planes parallel to the main flow direction, thereby mimicking the circumferential continuation of the bed, and translational periodic boundaries on the axial planes, as was done in the full-bed model.

For a WS model, periodic boundary conditions on the top and bottom boundaries are necessary, and a layout that allows for these conditions as well as the symmetry conditions is needed. The $N = 4$ full-bed model had nine-sphere wall layers and three-sphere center layers, as described in the previous section. The 120° section would contain three wall-layer spheres and one center-layer sphere, for a fully symmetrical layout. In the full-bed model six layers were necessary to create periodic conditions, because of the spiral structure in the three-sphere center layers. Using six layers in the segment model, however, would defeat the purpose of creating a segment model (reduction of size), so it was chosen to slightly adjust the central layer positions to allow for periodic boundary conditions over two layers of spheres, as shown in Fig. 4. There are several sphere segments from the three-sphere central layer that can be seen in the top view. One of the spheres from the central layer structure is completely enclosed in the segment model. The two other spheres, toward the symmetry walls of the segment, are truncated both by the symmetry wall and the top and bottom of the model. The smaller dashed semicircles

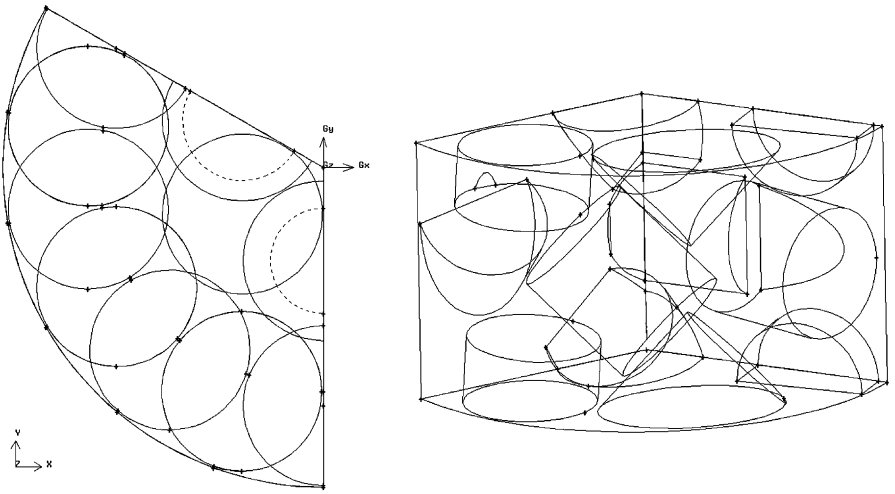

FIG. 4. The 120° wall-segment (WS) model: top (spheres) and front (cylinders).

within the sphere-outlines depict the intersection of the spheres with the top and bottom planes.

To simulate industrial packed tubes, we wanted to extend our WS approach to cylindrical particles, based on the model created for the $N = 4$ spheres WS. A 120° segment with two axial layers of particles and translational periodic boundaries on the column inlet and outlet was used for the cylindrical particle beds. An experimental study was performed by packing cylindrical particles with a 1:1 ratio in a bed with a tube-to-cylinder diameter ratio of 4. Dense particle packing structures were created using the Unidense method. From a large selection of packing structures, it could be seen that there were distinct common particle situations near the tube wall, such as the 45° angled particle, or axially aligned particles. The most common arrangement of cylindrical particles near the wall of the column proved to be the one with the round surface of the cylinder against the wall of the column with the particle axis at an angle with the axis of the column (see Fig. 4). To represent this most common orientation the base geometry was created with the main particle axis at a 45° angle with the column axis, as shown. The peripheral particles were then placed in the geometry, based on situations encountered in the physical examples, allowing for the periodic boundary conditions.

4. *Contact Points*

In a packed tube there are a large number of contact points where the particles touch each other and the tube wall. This results in very narrow regions in the computational domain, which creates problems in meshing the packed tube geometry. Automatic mesh generation can result in volumes that are extremely skewed around the contact points, meaning that some of their surfaces can be much larger than others within the one tetrahedron. Manual mesh generation at contact points would involve an unrealistic amount of work as the number of contact points increases rapidly as the number of particles in a tube increase to more realistic levels.

Magnico (2003) included contact points with a fine structured mesh and successfully carried out DNS simulations of laminar flow at low to moderate Re. However, Esterl *et al.* (1998) and Calis *et al.* (2001) both reported that gaps were introduced between the spheres in their geometries. Tobiś (2000) was able to avoid the problem, as his experimental set-up had particles glued together which he modelled in his CFD simulation. Gunjal *et al.* (2005) did not report their treatment of the problem, but from their figures it seems that they, too, introduced gaps between the spheres. A different approach seems to have been used by Guardo *et al.* (2004), who actually increased the sizes of their spheres by 1% so that they overlapped slightly. They encountered no convergence difficulties, but the impact of this change on heat transfer and velocity distributions has not yet been reported. For our simulations, it was not possible to obtain

convergence under turbulent flow conditions when actual contact points of the spheres with each other or the wall were incorporated.

Our approach (Nijemeisland and Dixon, 2001) was to create a gap between the different entities in the geometry, and then verify that the flow field was not disturbed by the gap. To choose the correct gap size a number of different models were created with a small number of spheres, and differing diameters, to allow for different gap sizes. The largest sphere size that would permit a turbulent model to be solved was 99.5% of the original sphere size. Other models were created with sphere sizes of 99%, 97% and 95%. These models were compared using velocity distribution histograms of fluid elements near the contact points. The fluid elements for comparison were selected by limiting the fluid zone to a small area approximately 0.5 cm square around the contact point (Fig. 5a). In the five different geometries air was flowed through the bed at a Reynolds number of about 20. Velocity magnitude data were taken from the different geometries and compared.

It was shown that when the gaps were larger (the 95% and 97% sphere sizes) the velocity distribution tended to move to higher velocities. Both the 99.5% and 99% sphere size models showed negligible difference from the touching model's velocity distribution (see Fig. 5b). For our heat transfer studies at moderate Re it was decided to create models with 99% spheres. This was chosen because this gap size allowed for easier construction and faster convergence than the 99.5% spheres model, without any loss in accuracy. Calis *et al.* (2001) also chose to reduce their spheres to 99% of the full size. For our later work under more extreme steam reforming simulation conditions, higher pressure and higher flow rates, it was necessary to re-evaluate the particle size reduction. It was found that at these high flow rates a 99% reduction of the spheres would

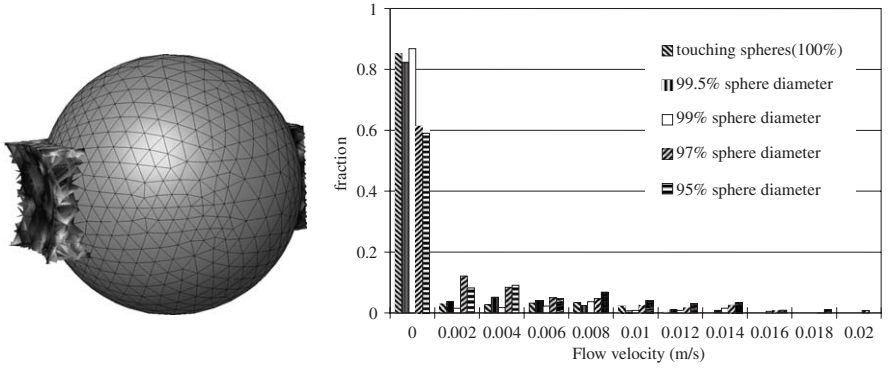

FIG. 5. (a) Selected elements around the sphere contact points for mesh comparison; (b) Velocity histograms for comparison of the different gap sizes, $v_{in} = 0.01$ m/s. Reprinted from Chemical Engineering Journal, Vol. 82, Nijemeisland and Dixon, Comparison of CFD simulations to experiment for convective heat transfer in a gas-solid fixed bed, pp. 231–246, Copyright (2001), with permission from Elsevier.

result in considerable amounts of flow in the gaps, creating an unrealistic flow field. The gap size was reduced until the no-flow area around the contact point was re-established. The resulting particle size reduction was 99.5%. These results demonstrate the necessity to evaluate the approach to contact points on small reduced models before implementing it on the simulation model.

C. Packed Bed CFD Simulation Issues

1. Packed Bed Flow Regimes

When running a CFD simulation, a decision must be made as to whether to use a laminar-flow or a turbulent-flow model. For many flow situations, the transition from laminar to turbulent flow with increasing flow rate is quite sharp, for example, at $Re = 2100$ for flow in an empty tube. For flow in a fixed bed, the situation is more complicated, with the laminar to turbulent transition taking place over a range of Re, which is dependent on the type of packing and on the position within the bed.

Several studies have looked at questions such as the transition to turbulence, the level of turbulence intensity in the void space, and the delineation of flow regimes in fixed bed flow. Some of the earliest works investigated turbulence intensity for gas flow in beds of spheres. Mickley *et al.* (1965) used hot-wire anemometry for air flow in a rhombohedral packing at $Re = 4{,}780$ and 7,010. They concluded that the dispersion coefficients for the bed were determined by "side-stepping" of the fluid stream as it passes between particles, as eddy diffusivity in the voids was much smaller than the bed dispersion. They found that eddy shedding did not occur in the packing voids, and that high local heat transfer coefficients in spherical packings must be due to turbulence intensity in the voids, which was as high as 50%, measured behind the seventh layer. Van der Merwe and Gauvin (1971) also found no eddy shedding except on the first bank of spheres in their regular packings over the range $2{,}500 < Re < 27{,}000$, and turbulence intensity values around 25%. Turbulence measurements at much lower Re (50–1470) were made by Kingston and Nunge (1973) in a rhombohedral array, who found that particle geometry and packing configuration had a large effect on maximum intensity and transition Re.

Early studies of the transition to turbulence relied on flow visualization techniques for liquid flow through arrays of spheres. Jolls and Hanratty (1966) found a transition from steady to unsteady flow in the range $110 < Re < 150$ for flow in a dumped bed of spheres at $N = 12$, and they observed a vigorous eddying motion that they took to indicate turbulence at $Re = 300$. In regular beds of spheres, Wegner *et al.* (1971) found completely steady flow with nine regions of reverse flow on the surface of the sphere for $Re = 82$, and similar flow elements but with different sizes in an unsteady flow at $Re = 200$. Dybbs and Edwards (1984) used laser anemometry and flow visualization to study flow

regimes of liquids in hexagonal packings of spheres and rods. They determined that there are four flow regimes for different ranges of Reynolds number, based on interstitial or pore velocity $Re_i = Re/\varepsilon$:

(1) $Re_i < 1$: Viscous or creeping flow in which pressure drop is linearly proportional to interstitial velocity and flow is dominated by viscous forces;
(2) $10 \leq Re_i \leq 150$: Steady laminar inertial flow in which pressure drop depends nonlinearly on interstitial velocity and and boundary layers in the pores become pronounced with an "inertial core" appearing in the pores;
(3) $150 \leq Re_i \leq 300$: Unsteady laminar inertial flow in which laminar wake oscillations appear in the pores and vortices form at around $Re_i = 250$;
(4) $Re_i > 300$: Highly unsteady flow, chaotic and qualitatively resembling turbulent flow.

These results are in reasonable agreement with the earlier work in terms of Re, and also the authors make the point that some workers used the term "turbulent" to cover the unsteady range.

This general classification of flow regimes appears to have been generally accepted, with some reservations about the transitions. Latifi *et al.* (1989) sought to remove the influence of the observer by using microelectrodes as electrochemical sensors, to get more precise regime transitions. They later corrected their results (Rode *et al.*, 1994) to include the transfer function of the electrochemical probe and gave the transition to time-dependent chaotic flow as $110 < Re < 150$, but noted that this was not necessarily fully developed turbulence. They made measurements on the tube wall and found that flow was extremely nonhomogeneous at different spatial locations in a packed tube. This result was confirmed by Seguin *et al.* (1998a) in their study of the end of the stable, laminar regime, which they found to occur at $Re = 113$ inside the bed, but at $Re = 135$ at the wall. A similar study from the same group (Seguin *et al.*, 1998b) to determine the transition to the turbulent regime found that the transition was gradual and not at the same Re at all locations. They obtained stabilization of the fluctuation rate, corresponding to local turbulence, at 90% of the electrodes for $Re > 600$.

The effects of inertia on flows in both ordered and random arrays of spheres have been approached by lattice-Boltzmann simulations for small Re (Hill *et al.*, 2001a) and for moderate Re (Hill *et al.*, 2001b). These studies illustrate the scaling of drag force with Re, and especially extend the experimental results to beds of more dilute solid fraction. An interesting point of view was provided by Niven (2002), who claimed that the transition to nonlinear behavior was not due to turbulence, but to expansion, contraction, and changes in direction of the flow, i.e., an increase in inertial forces relative to viscous ones. This viewpoint has been challenged by Stevenson (2003), who suggests that the transition from laminar flow to turbulence may occur at much lower Re in a packed tube than

an empty one, due to the reduced viscous damping of radial velocity components caused by flow instabilities.

The detail of the fluid mechanical studies of flow in particle arrays stands in sharp contrast to the highly simplified pictures used for reaction engineering. From the above survey, it appears that it would be safe to set up CFD simulations with a steady laminar flow model for $Re < 100$, and to use RANS turbulence models for $Re > 600$, and simply to avoid the unsteady intermediate range. A similar point of view was taken by Gunjal *et al.* (2005), who used a laminar model up to $Re_i = 204.74$ and turbulent models for $Re_i = 1{,}000$ and 2,000. They also argued that the onset of unsteady flow is delayed by particles packing closely together, and that the fluid is confined and stabilized by neighboring spheres. Magnico (2003) suggests that the stationary hypothesis can be used up to larger Re, and regarded as a coarse approximation. At present, the use of CFD in the transition range can be informed by the intended use of the simulations. If details of the flow environment of the particles are essential, then a very fine mesh should be used and unsteady laminar calculations must be performed. So far this approach has not been taken, to our knowledge. Alternatively, if improved bed-scale modeling is sought, which incorporates more realistic fluid flow on the scale of particles or larger, then an approximate steady flow can be obtained by either turbulent or laminar models, and often both are used and compared to see if the bed scale flow features are the same.

2. *Mesh Generation*

An important part of CFD modeling is the construction of the mesh, especially in complex geometries such as fixed beds. The mesh strongly affects the accuracy of the simulation. It has to be chosen with enough detail to describe the processes accurately and with a degree of coarseness that enables solution within an acceptable amount of time. When an optimal density has been found, refining the mesh will increase the model size without displaying more flow detail. When it is coarsened, the mesh may obscure possibly essential parts of the flow detail. The mesh determines a large part of creating an acceptable simulation.

The two main types of mesh are structured and unstructured. In a structured mesh there are families of grid lines, and grid lines of the same family do not cross each other and cross each member of the other families only once (Ranade, 2002). Block-structured grids allow local refinement of structured grids. Unstructured grids are typically made up of tetrahedral cells in 3D, and can be locally refined anywhere. They are very suitable for complex geometries such as those found in packed tubes. The Chimera grid in Fig. 6a was used by Agarwal (1999) to illustrate types of grids for aircraft wings. Similar Chimera grids were used by Nirschl *et al.* in simulations of a single sphere between moving walls, and by Esterl *et al.* (1998) and Debus *et al.* (1998) for packed tube simulations. Each sphere had its own prismatic fitted mesh to resolve the

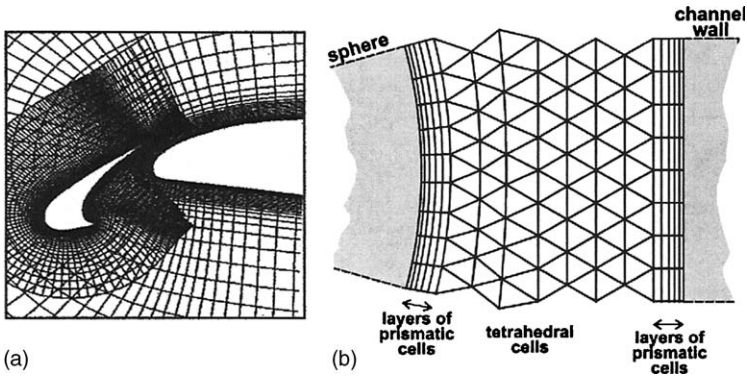

FIG. 6. Examples of types of meshes developed to resolve laminar flow around particles: (a) Chimera grid. Reprinted, with permission, from the Annual Review of Fluid Mechanics, Volume 31 © 1999 by Annual Reviews www.annualreviews.org; (b) Unstructured grid with layers of prismatic cells on particle surfaces. Reprinted from Chemical Engineering Science, Vol. 56, Calis *et al.*, CFD Modeling and Experimental Validation of Pressure Drop and Flow Profile in a Novel Structured Catalytic Reactor Packing, pp. 1713–1720, Copyright (2001), with permission from Elsevier.

boundary layers, which was overlaid on a coarser main mesh for the tube. They had to work with a very fine mesh to capture the gradients in the laminar flow in the narrow gaps between the particles.

The grid shown in Fig. 6b was developed by Calis *et al.* (2001) and consisted of five layers of prismatic cells on the walls of the spheres and tube, and unstructured tetrahedral cells in between. To obtain grid-independent pressure drops under laminar flow they had to restrict the first layer of prismatic cells to be 0.052 mm thick. The thickness then increased for the following four layers. The tetrahedral cells were 0.4 mm in size. In their later work (Romkes *et al.*, 2003), which included heat transfer, they had to reduce the size of the first layer of prismatic cells by a factor of three under laminar flow.

Other workers have also commented on the need for fine meshes on the wall surface in laminar flow. Magnico (2003) claimed that the spatial resolution or cell size must be less than $d_p/40$, while for LBM simulations, Zeiser *et al.* (2002) recommended cell size between $d_p/30$ and $d_p/20$ and Freund *et al.* (2003) used a grid of size $d_p/30$. These cell sizes are in line with the experiences of Tobiś (2000) who used mesh sizes of 1 mm and 2 mm with particles of diameter 38 mm, and our own experience in which we used average cell sizes in the range 0.5–1 mm depending on the simulation conditions, for particles of 25.4 mm diameter.

The preferred range for the thickness of the near-wall cell layer is $y^+ > 30$. However, this is difficult to achieve in packed tubes. The cells sizes are constrained by the need to fit in between the gaps and/or narrow spaces between particles, so they cannot be too large. This can result in the y^+ values being too small for proper application of wall functions. The alternative to use small enough cells to resolve the boundary layer ($y^+ < 1$) increases the computational

cost unacceptably, at present. For turbulent flow, Calis *et al.* (2001) employed the $k-\varepsilon$ model with wall functions on a tetrahedral mesh of size 1.0 mm.They noted that the velocity varies widely near particle surfaces, so that y^+ can also vary by a factor of over 40. Their average y^+ was in the range 4.4–440 for their range of *Re*. Guardo *et al.* (2004) report $4<y^+<12$, and our simulations result in similar values for y^+. Romkes *et al.* (2003) said that the y^+ criterion for the use of wall functions was met in their work only at the highest *Re*, and for their lowest *Re* they obtained $y^+<1$.

The effects on the computed flow of applying the wall functions outside their preferred range are not yet clear. Guardo *et al.* (2005) claim that the Spalart–Allmaras model performs well under such conditions, due to the coupling of wall functions with damping functions. They found good predictions of pressure drop despite the range of y^+, and that this quantity was not sensitive to near-wall cell size. The heat transfer coefficient, in contrast, was very sensitive. Romkes *et al.* (2003) found that heat transfer under turbulent flow was only weakly dependent on y^+. Clearly this area requires further investigation.

We determined an appropriate mesh density for our simulations by comparing results from several different mesh sizes (Derkx and Dixon, 1996; Logtenberg and Dixon, 1998a, 1998b; Logtenberg *et al.*, 1999). An optimal mesh density was chosen from these previous studies on small particle clusters and additional studies for the WS simulation geometries used later (Nijemeisland and Dixon, 2004). Typical examples are shown in Fig. 7 for the unstructured grids.

It was shown that there were no differences between the flow solutions whether a completely fine mesh was used or a locally refined mesh. This mesh had a node spacing equal to the size of the gap at the sphere contact points at these locations, gradually grading toward a four times coarser node spacing near the voids in the geometry. The node distributions on the sphere surface were also graded from fine near the contact point to coarser away from the

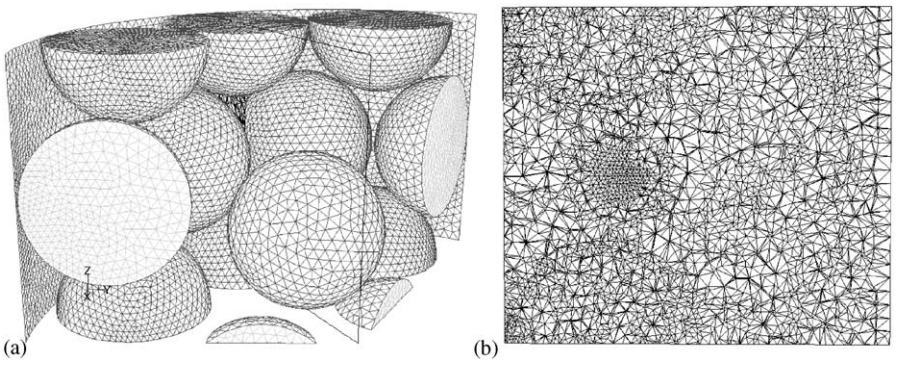

FIG. 7. Typical examples of unstructured meshes: (a) the surface mesh on a number of spheres and a section of the cylinder and (b) a section of the interior mesh in a plane indicated in part (a).

contact points, resulting in a graded mesh both in the fluid region as well as in the solid region, the inside of the particles. The results of the graded meshing can be seen in Fig. 7b. Mesh gradation was defined using a first–last-ratio principle, in the pre-processing GAMBIT package. In this method a changing node density on an edge in the geometry is created by two user-specified parameters, an average node spacing, and the size ratio between the first and the last node on the edge. The average node spacing in the graded mesh was set to 0.03 inch, and the first–last-ratio was set to 0.25, resulting in a factor 4 difference in node spacing between the fine and coarse regions. The indicated settings create a mesh where the node spacing is 0.015 inch near the contact points (the finely meshed regions) and 0.06 inch at the coarsely meshed regions.

3. *Conjugate Heat Transfer*

When conjugate heat transfer through solid particles in the tube is to be included, the energy balance must be solved in the solid particles, in addition to the fluid flow regions. The energy balance for a solid region is defined by:

$$\frac{\partial(\rho h)}{\partial t} = \frac{\partial}{\partial x_i}\left(\lambda \frac{\partial T}{\partial x_i}\right) + S_h \tag{23}$$

The last term S_h is the volumetric heat source, which may include user-defined energy source terms. The sensible enthalpy, h, is defined as

$$h = \int_{T_{\text{ref}}}^{T} c_p dT \tag{24}$$

which is consistent with Eq. (14) since $c_p = \sum_j Y_j c_{p,j}$.

The inclusion of heat transfer in the particles means that the solid regions must also be meshed, in addition to the fluid regions. This can considerably increase the mesh size. If the solid particles are only subjected to simple conduction, steady-state gradients within them are not likely to be large, and it may be expected that a coarse grid would suffice. This may not be true if heat effects of reaction are to be included via the source terms. The use of a fine mesh in the fluid region, especially in the vicinity of the contact points, requires the use of a matching fine mesh in the solid particles. Even with mesh coarsening toward the center of the particles, the increase in mesh size may be substantial. One way to deal with this may be to use nonconformal grids, in which the grid points in the solid do not have to coincide with the grid points in the fluid at the fluid–solid interface. This may be a limited remedy, as curvature in the surfaces of the particles will limit the extent to which there can be a mismatch between the grids.

4. *Boundary Conditions*

A no-slip boundary condition is used on all impermeable solid surfaces, but the choice of boundary conditions for the inlet and outlet of the model is not so

straightforward. It is generally accepted that when flow enters a structured or randomly packed fixed bed, an area near the entrance of the bed has an undeveloped flow profile as the fluid is adjusting from one flow environment to another. A similar situation is found near the exit of the bed, where a sudden change in pressure drop is experienced and the flow ''relaxes'' before it actually exits the bed. In a full model, in which an actual bed inlet and outlet were modeled, a large portion of the bed would need to be modeled just to eliminate entrance and exit effects from the central portion of the bed that was the main focus of the study. In a real industrial packed tube, in contrast, the entrance and exit of the bed are usually small compared to the length, and an active bed may be preceded or followed by inert packed sections that condition the flow.

In our $N = 4$ models we use translational periodic flow boundaries at both the flow inlet and flow outlet of the column, in which all variables except pressure are identical at the periodic planes. The total mass flow is supplied to the model at the inlet boundary, to give the desired Reynolds number. By imposing the translational periodic boundaries a generic, developed flow solution is obtained. Since the translational periodic boundary defines the column inlet to be identical to the column outlet, there is no flow development in the bed; a steady-state flow situation is obtained. The periodic boundaries remove the effects of an entrance or exit effect in the bed. The overall size of the model can now be greatly reduced. Other groups have used periodic conditions at the inlet and outlet of a packed tube (Magnico, 2003) or on the flow surfaces of unit cells (Tobiś, 2000; Gunjal *et al.*, 2005), whereas Guardo *et al.* (2004) set a constant velocity at their tube inlet and a constant pressure at the outlet. Calis *et al.* (2001) and Nijemeisland and Dixon (2001) simulated lengths of empty tube before and after their packed regions.

Clearly, the pressure itself cannot be periodic even if the geometry of the model is periodic. Instead, the pressure drop is periodic. The local pressure gradient is decomposed into two parts: the gradient of a periodic component, superimposed on the gradient of a linearly varying component. The linearly varying component of the pressure corresponds to the familiar packed-tube pressure drop. Its value is not known before the simulation; it must be iterated on until the mass flow rate that was specified is achieved in the computational model.

When heat transfer is included in the CFD model for a packed tube, the tube wall is heated (or cooled for some applications). Either temperature or heat flux is given at the wall. The gas heats up as it passes through the tube, and the temperature field cannot be treated as periodic. Since we want to investigate the energy penetration into the bed from the wall, it is necessary to reinstate the generic bed section as a section in a larger bed, defining different inlet and outlet conditions. For the fluid, the inlet temperature should be specified. This could also be done for the solid particles; however, an alternative is to choose the inlet heat flux to be zero for the solid regions. Outlet conditions are required for the solid regions only, and again a zero heat flux condition can be used. For full-bed

models this has the disadvantage that a considerable part of the simulated tube may be atypical of the bed as a whole, due to the uniform inlet temperature profile. In addition, for short-bed segments, the temperature profile may not develop enough for the effects of flow throughout the entire model to be felt. To calculate the development of the temperature profile into the bed, a series of simulations have to be performed.

To overcome thermal entry effects, the segments may be virtually "stacked" with the outlet conditions from one segment that becomes the inlet conditions for the next downstream section. In this approach, axial conduction cannot be included, as there is no mechanism for energy to transport from a downstream section back to an upstream section. Thus, this method is limited to reasonably high flow rates for which axial conduction is negligible compared to the convective flow of enthalpy. At the industrial flow rates simulated, it is a common practice to neglect axial conduction entirely. The objective, however, is not to simulate a longer section of bed, but to provide a developed inlet temperature profile to the test section.

5. *Convergence*

The discretized equations of the finite volume method are solved through an iterative process. This can sometimes have difficulty converging, especially when the nonlinear terms play a strong role or when turbulence-related quantities such as k and ε are changing rapidly, such as near a solid surface. To assist in convergence a relaxation factor can be introduced:

$$\phi_p^{\text{new}} = \alpha_\phi \phi_p^{\text{new}} + (1 - \alpha_\phi)\phi_p^{\text{old}} \tag{25}$$

The relaxation factor (α_ϕ) is a multiplier for the change in the solution variable. When this factor is less than unity, the process is called under-relaxed. When under-relaxed, the iteration process is slower, since the step change is small, but less likely to diverge. Commercial codes, such as Fluent, will typically recommend values for the under-relaxation factors that work well with a wide range of flows. For packed-tube simulations, we have usually needed to reduce the default values by a small amount, usually 0.2. Some simulations, however, did not converge until very small values, of the order of 0.1 or lower, were used and values in this range for pressure and velocity under-relaxation factors have also been suggested by Gunjal *et al.* (2005).

To determine when a solution is converged usually involves examining the residual values. The residual value is a measure of the imbalance in the discretized equation, summed over all the computational cells in the domain. Residuals can be obtained for continuity, velocity components, and turbulence variables. Again, it is common practice to set a "cut-off" value for the normalized residual values. When the set value is reached, the iteration process is stopped. Our experience with packed-tube simulations, especially if low

under-relaxation factors are used, is that the cut-off values should be set very low, and the iteration continued until the residuals have leveled out. This will normally be a good deal higher for turbulent flows than for laminar ones, and flow residuals are higher than those for energy. In addition, it is a good idea to monitor other measures of convergence besides the residuals, such as pressure drop and/or an averaged wall shear stress or exit temperature (Guardo *et al.*, 2004; Gunjal *et al.*, 2005). We have seen apparently level residuals, while the pressure drop slowly changed, and a substantially different final flow field was eventually obtained, often after several thousand iterations. Following apparent convergence, it is essential to check both mass and energy balances, as well as performing grid independence studies and comparing to experimental results, to have confidence in the solution. Just because a simulation has converged, does not mean that it is necessarily reliable.

Convergence of the discretized system can sometimes be problematic, especially for some of the turbulence models. In such cases, using a laminar flow solution as an initial guess for the turbulent flow field can be helpful. Similarly, when using options such as nonequilibrium wall functions or enhanced wall treatment, convergence can be facilitated by first obtaining a solution using the k–ε model with standard wall functions, and then switching to the desired model.

D. Validation of CFD Simulations for Packed Beds

1. Flow Field Validation

Since the CFD methodology is not specifically designed for application in constrained geometries, such as particle packed beds, it is necessary to verify if the simulated results are valid. Although the CFD code is based on fundamental principles of flow and heat transfer, some of the boundary issues are modeled using empirical data not necessarily appropriate for fixed bed applications. Validation of CFD flow calculations has generally taken one of the two forms. In the first, noninvasive velocity measurements inside the packed bed have been made, and compared to velocities computed from a model of either the entire experimental bed or a representative part of it. In the second form, computed pressure drops have been compared to either measured values or established correlations for pressure drop in fixed beds, such as the Ergun equation (Ergun, 1952).

The direct experimental verification of the computed flow field requires noninvasive measurements of velocity components inside the packed tube. One very promising technique for this is magnetic resonance (MR) as described in a recent review by Gladden (2003). She showed pictures of 3D MR visualization of axial velocity for flow of water in packings of spheres, and her group has used MR to connect the 3D structure of a packed bed to the transport phenomena in

it (Sederman *et al.*, 1998) and to validate their lattice Boltzmann code for low-*Re* simulations of water flowing through arrays of spheres (Manz *et al.*, 1999). They have also combined MR spectroscopy with imaging to get noninvasive measurements of chemical conversion inside the bed (Yuen *et al.*, 2002).

Maier *et al.* (1998) also used LBMs to simulate flow through a column of beads for $N = 10$, which they then compared to the NMR data of Lebon *et al.* (1996). They obtained encouraging agreement for the qualitative features such as negative velocities; however, they saw differences in peak values of normalized velocity, some of which they attributed to longitudinal dispersion. Most recently, Gunjal *et al.* (2005) conducted CFD simulations of laminar flow through a simple cubic unit cell corresponding to the set-up used by Suekane *et al.* (2003) in their MRI studies. Comparisons were made over the range $12.17 \leq Re_i \leq 204.74$ and showed good agreement for axial components of velocity. At the highest flow rate inertial flow was dominant, with jet-like flow being observed in both experiments and simulations. Some discrepancies were seen at the lowest flow rate, which may have been attributable to experimental difficulties in maintaining a constant low flow rate. Overall, the CFD simulations correctly captured the inertial flow structures, including vortices. Comparisons were also made between the finite-volume CFD calculations and the LBM simulations of Hill *et al.* (2001a), with good results.

Freund *et al.* (2003) chose to validate their LBM simulations using laser Doppler anemometry (LDA) measurements. Experiments for two packings of spheres at $N = 4$ and $N = 6.15$ were used, at a flow rate corresponding to $Re = 50$. Good agreement was found for the radial profiles of axial velocity, with the simulations reproducing the typical oscillations in velocity in the wall region. Some discrepancies were seen near the bed center, but the authors noted that while packing structure of experiment and model were identical near the wall due to the ordering there, some differences existed in the bed center.

No direct validations have yet been reported for the unsteady laminar or turbulent flow regimes, due to lack of experimental data at the higher flow rates. Measurements of pressure drop, however, can provide an indirect means of checking on the computations at higher flows, although most comparisons have, in fact, been made at relatively low flow rates. Many groups compare their results to the original Ergun (1952) equation for pressure drop (Gunjal *et al.*, 2005, Guardo *et al.*, 2004; 2005), or to later modifications or different correlations that take wall effects into account (Esterl *et al.*, 1998; Freund *et al.*, 2003; Magnico, 2003). In general, good agreement is claimed, especially for the lower *Re* range; however, many comparisons are presented on log-log graphs where it is harder to see differences.

There are few reported comparisons to experimental pressure drop data taken by the same workers. An exception is Calis *et al.* (2001) who compared CFD, the Ergun correlation and experimental data for $N = 1$–2. They found 10% error between CFD and experimental friction factors, but the Ergun equation

over-predicted by 80%, which they attributed to a poor prediction of the turbulent contribution. Their results extended to $Re = 40{,}000$.

The validation of CFD codes using pressure drop is most reliable when actual experimental data are taken in equipment identical to the situation that is being simulated. Existing literature correlations such as the Ergun equation are known to have shortcomings with respect to wall effects, particle shape effects, application to ordered beds and validity at high *Re*. The applicability of literature correlations to typical CFD simulation geometries needs to be examined critically before fruitful comparisons can be made.

2. *Heat Transfer Validation*

In this section a short description of a comparison between experimental and simulation results for heat transfer is illustrated (Nijemeisland and Dixon, 2001). The experimental set-up used was a single packed tube with a heated wall as shown in Fig. 8. The packed bed consisted of 44 one-inch diameter spheres. The column (single tube) in which they were packed had an inner diameter of two inches. The column consisted of two main parts. The bottom part was an unheated 6-inch packed nylon tube as a calming section, and the top part of the column was an 18-inch steam-heated section maintained at a constant wall temperature. The 44-sphere packed bed fills the entire calming section and part of the heated section leaving room above the packing for the thermocouple cross (Fig. 8) for measuring gas temperatures above the bed.

A radial temperature measurement consisted of establishing and recording a steady-state temperature profile for a combination of a specific bed length, Reynolds number, and angle of thermocouple cross. A total of four

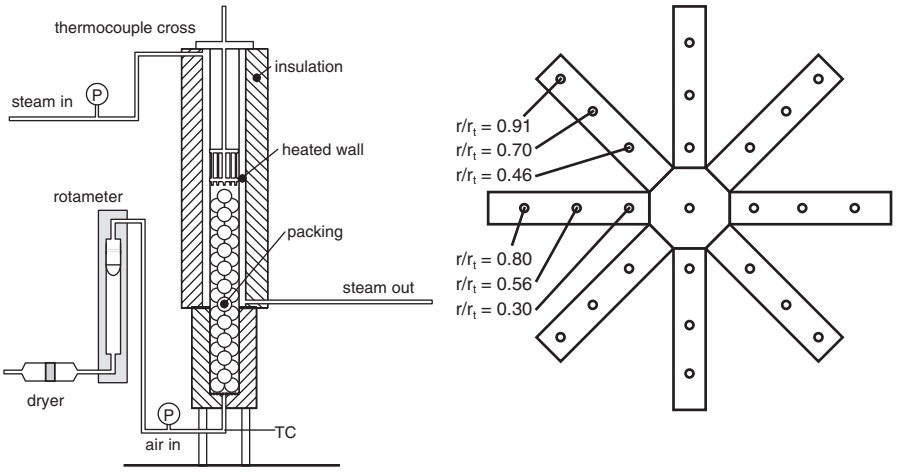

FIG. 8. Experimental setup and detail of the thermocouple cross.

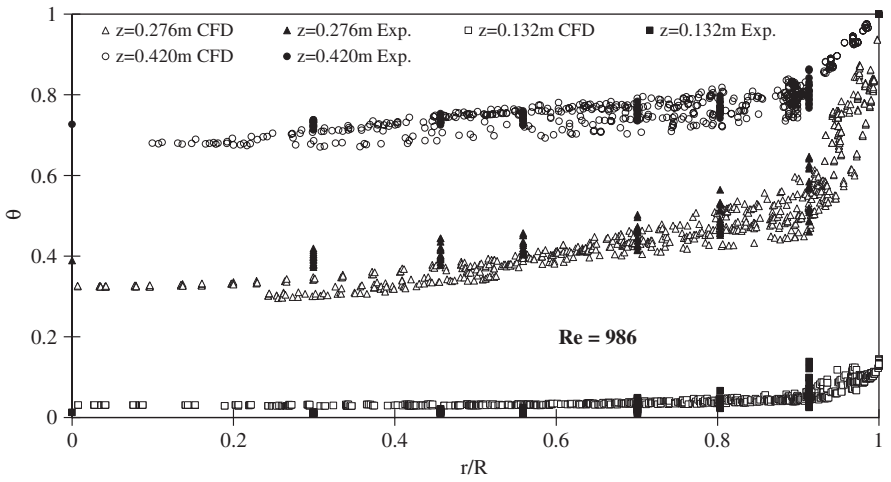

FIG. 9. Simulated and experimental radial temperature profiles at $Re = 986$.

thermocouple-cross positions were used for a measurement by rotating the cross 15°, 30°, and 45° from the initial orientation. By rotating the thermocouple cross a good spread of data points was ensured, giving a full picture of the angular spread of the radial temperature profile. Particle Reynolds numbers were varied from 373 to 1922; bed lengths were varied from 0.132 through 0.42 m.

Fig. 9 shows comparisons of CFD results with experimental data at a Reynolds number of 986 at three of the different bed depths at which experiments were conducted. The profiles are plotted as dimensionless temperature versus dimensionless radial position. The open symbols represent points from CFD simulation; the closed symbols represent the points obtained from experiment. It can be seen that the CFD simulation reproduces the magnitude and trend of the experimental data very well. There is some under-prediction in the center of the bed; however, the shapes of the profiles and the temperature drops in the vicinity of the wall are very similar to the experimental case. More extensive comparisons at different Reynolds numbers may be found in the original reference. This comparison gives confidence in interstitial CFD as a tool for studying heat transfer in packed tubes.

3. Wall-Segment vs. Full-Bed Validation

When simulations are done in a WS model, the results need to be validated against a full-bed model. The main reason for this is not only to see if the WS model results are representative for a full bed but also to check that the symmetry boundaries, which are relatively close to all parts of the segment model, do not influence the solution.

a. Comparing segment results to full-bed results. A fine mesh was created for the WS and the full-bed models. For the full bed, the mesh was too large for the 32-bit computers so it was reduced in size by excluding the solid parts (the particle internals) from the mesh. This mesh is referred to here as the ''no-sphere'' mesh. The finest possible mesh for the full bed that was created including all bed internals will be referred to as the ''re-mesh''. The ''no-sphere'' full-bed fine mesh was 2.6 million control volumes (cv), while the WS reduced this to only 756,700 cv. The full bed with the fine mesh was over 6 million cv, which was not implemented at the time (but has since become possible with a 64-bit machine), while the full bed with the coarse mesh was 1.97 million cv. In the initial comparisons velocity profiles were compared for both the full-bed meshes mentioned above (the no-sphere mesh and the re-mesh) as well as the WS model. Only velocity profile comparisons were eligible, since the no-sphere mesh could not give comparable energy solutions.

A section in the full-bed models was isolated that was comparable to the WS model. The layout of these different sections was identical, except that the WS model had a two-layer periodicity and the full-bed models had a six-layer periodicity. To be able to make direct comparisons of velocity profiles, several ''sample-points'' needed to be defined. In the three different models seven tangential planes were defined and on each plane three axial positions were defined. This reduced the data to single radial velocity profiles at corresponding positions in all three models, as shown in Fig. 10, for the WS model. Identical planes were defined in the full-bed models. Some spheres and sample planes 4 and 5 are not displayed to improve the visibility of the sample planes and lines. In the right-hand part of the figure, plane 4 is shown with the axial positions at which data were taken and compared.

Simulation data were collected and plotted from the three models. Flow magnitudes were plotted separately for the three different components of the flow, the axial velocity, v_z, the radial velocity, v_r, and the tangential velocity, v_θ for seven planes with three data-lines each. Selected results are shown in Fig. 11

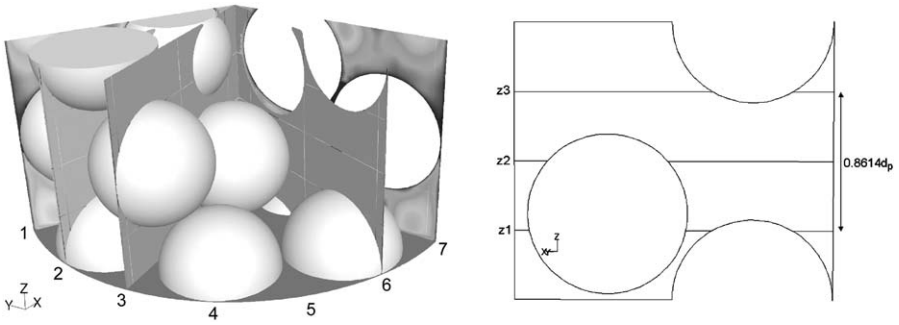

FIG. 10. Comparison section with seven tangential planes and axial profile lines indicated.

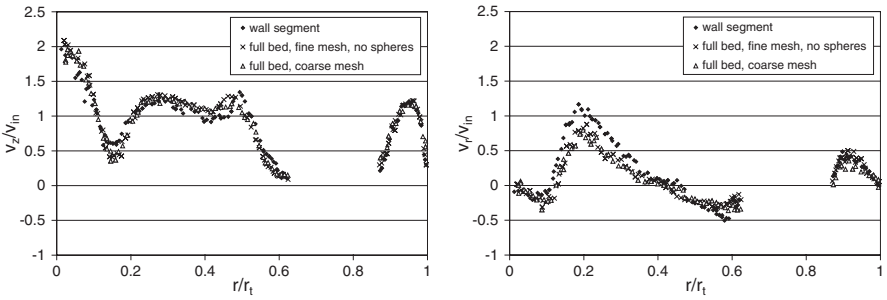

FIG. 11. Full-bed and WS mesh comparisons of axial and radial velocity components (at $Z3$).

for the axial and radial velocity components. All simulations were performed at a particle Reynolds number of 420, under atmospheric conditions with no temperature gradients. The superficial velocity in the simulations with a Reynolds number of 420 is 0.58 m/s, and this was used to normalize the different velocity components.

The velocity profile plots show interruptions in the velocity profile, where the solid packing was located. In general, the data of the three different cases agreed very well qualitatively; velocity highs and lows are shown at the same points in the bed. Quantitatively, the data of the two full-bed models are practically identical, indicating that the solutions were completely mesh independent.

The data from the WS model in some cases deviated slightly from the full-bed models. This could be explained by the slightly different layout of the WS model. Some spheres had to be relocated in the WS model to create a two-layer periodicity from the six-layer periodicity in the full-bed models. The differences in velocity magnitudes were mainly found in the transition area between the wall layers and the center layers. The effect of slightly larger gaps between spheres from the nine-sphere wall layers and the three-sphere central layers, due to the sphere relocations, had a noticeable effect on the velocity profile. Differences were also found in the central layer area where the sphere positions were not identical.

b. Wall-segment mesh independence. In the previous section, two meshes were compared for the full-bed models. Similarly for the WS model, two separate meshes were created: a fine mesh, as reported above, and a coarse mesh with the same mesh density as the full-bed coarse mesh. In Fig. 12, flow profiles of the fine mesh (labeled WS) are compared to the results from the coarse mesh. Also included in this comparison are the results from a simulation performed in a scaled-down version of the fine mesh model. A simulation geometry was created at 1/8th the size of the original model, to see if the absolute size of the model had a significant influence on the solution of the physical models, including the wall

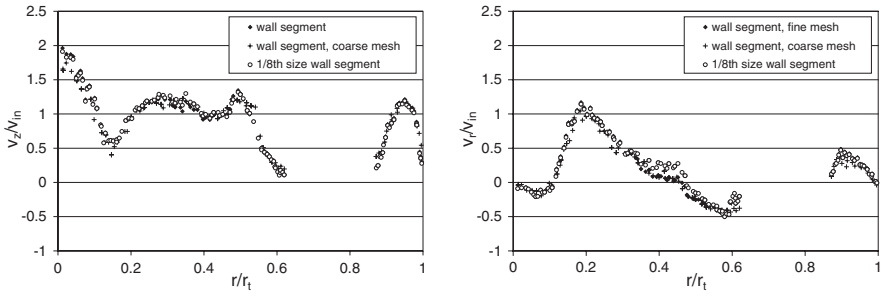

FIG. 12. Wall-segment mesh comparisons for axial and radial velocity components.

functions, which resolve the wall boundary layers. The results in Fig. 12 show complete mesh independence of the WS geometry and no effect of the scaling.

III. Low-*N* Packed Tube Transport and Reaction Using CFD

The broad objective of using CFD to simulate interstitial flow in packed tubes is to obtain a more fundamental understanding of the phenomena, taking place within them. Some more specific uses of this approach are (i) to obtain information (data) for conditions under which experiments are difficult or impractical, such as high temperatures or pressures; (ii) to obtain simulated measurements where sensors cannot be located without disturbing the bed packing, which would invalidate the measurements being sought; and (iii) to examine the individual contributions to transport and reaction in isolation, or to break down complex transport processes into their contributing mechanisms, in order to establish more fundamental correlations for them. In this section we want to examine the progress so far toward (iii) above, as CFD offers a very promising means of making further progress on problems that have resisted traditional approaches.

A. Hydrodynamics and Pressure Drop

As we have seen earlier, it is quite common for CFD pressure drop results to be compared to well-established empirical correlations of experimental data as part of the validation of the simulations. Some studies, in contrast, have used CFD to obtain the contributing mechanisms to pressure drop. One area in particular where this has been fruitful is structured packings. Corrugated-sheet structured packings have been studied by Petre *et al.* (2003) and Larachi *et al.* (2003). A layer of this type of structured packing is made of an ensemble of a large number of "Toblerone-like" triangular flow channels having identical

cross-sections. These channels are the result of the voids between two adjacent corrugated sheets that are placed together at opposite orientations.

Structured packing is expensive, so good geometric design of the elements is important, to optimize performance. Design is still empirical, however, and the limits of the correlations and design data are uncertain, since the constants for describing hydrodynamics and mass transfer have been obtained by calibrating models using laboratory experiments. CFD allows the rigorous fluid transport equations to be solved locally, to better understand the phenomena.

Petre *et al.* (2003) have presented an approach that combines a mesoscale and a microscale predictive approach. They identify recurrent mesoscale patterns in the packing, termed representative elementary units (REU), such as criss-crossing junctions, two-layer transitions, entrance regions, etc. They choose these REUs by identifying important dissipative phenomena at different parts of the packing. They then use CFD to simulate each REU over a wide range of Reynolds number from creeping to turbulent regimes. The next step is the conjecture that total resistance to flow can be obtained from adding the resistances of individual REUs. The simulations for each REU gave pressure drop at the microscale, from which they extracted a correlation for its loss coefficient. These coefficients were then used to predict the additive contribution to the total bed pressure drop. The results were checked to see that they were not dependent on the sizes of the REUs, and the bed pressure drops were compared to literature experimental data with good agreement, to within 10–20%. A follow-up paper (Larachi *et al.*, 2003) used this approach together with CFD to evaluate proposed geometric design changes of structured packings in terms of energy loss and pressure drop.

Fig. 13 shows typical results in a plot of pressure drop per unit length against the gas flow factor F_s ($= v\rho^{0.5}$). Four types of REUs were identified and simulated, and correlations were developed. The pressure drop arising from criss-crossing elements was the largest contribution to pressure drop of the four. The total pressure drop predicted from the individual contributions was in excellent agreement with literature data.

Returning to more conventional tube packings, several investigators have looked at the contributions to pressure drop in arrays of spheres. Esterl *et al.* (1998) suggested that CFD could be used to numerically test the assumptions made in deriving the analytical result that dissipation of energy is 75% due to elongational effects and 25% due to shear effects. Dhole *et al.* (2004) investigated the contributions to drag of power-law fluids in distended beds of spheres at intermediate Re. Since their packings had high void fractions, they could use an idealized cell model where each sphere was surrounded by an envelope of fluid. Their main focus was to write the drag coefficient as the sum of a pressure component and a frictional component, and determine how these behaved as functions of the power law fluid index. Gunjal *et al.* (2005) analyzed the relative contributions of shear drag and form drag for their unit cell packings of cubic and rhombohedral spheres. They found that the viscous

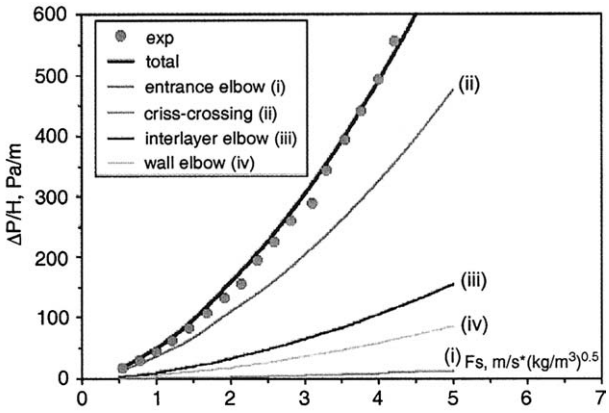

FIG. 13. Breakdown into the contributing dissipation mechanisms of dry pressure drops in vessels containing Montz B1-250.45 structured packings. Reprinted from Chemical Engineering Science, Vol. 58, Petre *et al.*, Pressure Drop Through Structured Packings: Breakdown Into the Contributing Mechanisms by CFD Modeling, pp. 163–177, Copyright (2003), with permission from Elsevier.

contribution was between 21% and 27% of the total, and was relatively constant in the laminar regime of $12 < Re < 200$.

The influence of bed geometry on frictional resistance has been studied systematically (Tobiś, 2000, 2001, 2002) using turbulence promoters placed between spheres in a cubic model packing. The experimental and CFD study began with turbulent air flow through six model packings (Tobiś, 2000), which consisted of a base cubic arrangement of spheres with different turbulence promoters—rectangular bands, triangular prisms, or cylindrical tubes—inserted between them. Wall effects were partially reduced by experimental design, and the remaining effects were eliminated by analysis and did not play a part in this work. The CFD calculations were checked against experiment and different mesh sizes, and turbulence models were used and gave good agreement with each other. The author tested the Ergun equation and concluded that the friction factor could not be correlated using bed porosity ε and hydraulic diameter d_h as the only measures of bed structure, which goes to explain why the constants in the Ergun equation scatter between the various experimental investigations in the literature. A second study (Tobiś, 2001) used only the thin bands as inserts, but covered more arrangements, and different numbers of bands were used in the packing. The tested packings were identified as being made up of three arrangements of representative elementary units (REUs). CFD was used to predict the friction factors for the elementary REUs, and then these micro results were combined to get the macro pressure drop. It was concluded that local bed anisotropy and/or clear passages through the bed affect the pressure drop. Complex bed structures can be handled by the macro-correlation/micro-CFD approach, where local bed anisotropy is taken into account by micro-CFD, and channeling by formulas to

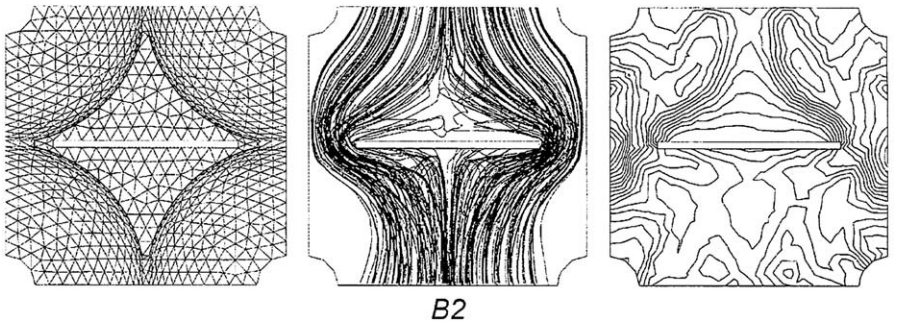

FIG. 14. CFD predictions of turbulent flow (meshed REU geometry, air pathlines with spheres hidden for clarity, contours of turbulent kinetic energy k) for configuration B2. Copyright 2001 From Turbulent Resistance of Complex Bed Structures by J. Tobiś. Reproduced by permission of Taylor and Francis, Inc., http://www.taylorandfrancis.com.

combine the friction factors for the REUs. Typical results are shown in Fig. 14, for a horizontal band REU, configuration B2.

The first part of this figure shows the triangular surface mesh with periodic conditions on the sides. The middle picture shows a view slightly tilted forward to show path lines of flow accelerating around the sides of the insert, and relatively slow flow in the wake region. Corresponding to these the third picture presents the high amounts of turbulence kinetic energy in the flow trailing from the sides of the insert. The author noted that the turbulence kinetic energy was not homogeneous in these complex packings. There was flow circulation in regions much smaller than the inter-particle space, and flow channeling through clear passages in the packing that provided evidence that there was not complete mixing in the packing interstitial space.

In the most recent paper in the series (Tobiś, 2002), the method was extended to chessboard periodic structures to look at different spatial arrangements of the same packing elements. Experiments showed that pressure drop depended not only on the resistance of the individual REUs but also on their spatial arrangement. The experiments were compared to interstitial flow simulations by CFD, superficial flow modeling by the modified Forchheimer equation, and a simplified structural method involving macrocorrelations. Although limiting cases of the macrocorrelations were useful, only the CFD simulations could reproduce observed experimental results, and further development of the structural approach to provide less expensive models is needed.

Contributions to pressure drop have also been studied by lattice Boltzmann simulations. Zeiser *et al.* (2002) postulated that dissipation of energy was due to shear forces and deformational strain. The latter mechanism is usually missed by capillary-based models of pressure drop, such as the Ergun equation, but may be significant in packed beds at low Re. For a bed of spheres with $N = 3$, they found that the dissipation caused by deformation was about 50% of that

caused by shear, over the range $0.1 < Re < 20$. The deformation contribution decreased as *Re* increased. Later work by the same group (Freund *et al.*, 2003) over a higher range of *Re* concluded that correlations for pressure drop cannot account for the influences of local structure on global pressure drop. The authors saw small changes in bed void fraction causing much larger changes in pressure drop than could be explained by the nonlinear terms, which pointed to local effects. An extremely thorough investigation of drag force on spheres, and its dependence on *Re*, has been performed by Hill *et al.* (2001a, b), also using LBMs. These studies examined the effects of fluid inertia at small to moderate *Re*, on flow in ordered and random arrays of spheres over a wide range of void fractions.

Although most CFD work has focused on pressure drop, several studies have also reported radial profiles of axial velocity, which are also of interest for simplified 1D models of fixed bed fluid flow. Zeiser *et al.* (2002) found an oscillating profile, with two peaks at $d_p/8$ and d_p from the wall, for a tube with $N = 3$. Magnico (2003) found a qualitatively similar result for $N = 5.96$ and $N = 7.8$, but in those results the near-wall peak was lower, which differs from all other workers. Zeiser *et al.* (2001) gave fairly qualitative pictures for $N = 5$ and $N = 6$, while Freund *et al.* (2003) also found a maximum close to $d_p/8$ for $N = 4$ and $N = 6.15$. Overall, most studies show the near-wall peak at $d_p/8$ with a magnitude of about 2.5–3 times the superficial average velocity, which is lower than BFD-type models unless an effective viscosity is introduced. Good agreement has been demonstrated in a few studies with LDA experiments, when they have been available for the same geometry. The similarity of the velocity profiles near the wall for beds of spheres is not surprising, given the analogous result for porosity. Toward the bed center, where the wall ordering decreases, the agreement is not so good. Also, beds of cylinders and other shapes of particles might be expected to give interesting results that may not be the same as for spheres.

B. Mass Transfer, Dispersion, and Reaction

A number of studies have used CFD results to obtain information on dispersion or mass transfer in packed tubes, in addition to the usual hydrodynamic results. Some relatively recent work has also included reaction. This area is so far not as well developed as the pressure drop and flow fields results of the previous section; however, some promising first steps have been taken.

Structured packings were studied using CFD by Van Baten *et al.* (2001), who wished to determine the radial liquid residence time distribution of a KATAPAK-S-like structure for comparison to conventional fixed beds for use in heterogeneously catalyzed reactive distillation processes. Such structured packings consist of catalyst particles sandwiched between corrugated sheets of wire gauze that are sealed around the edge. A group of these sandwiches is then

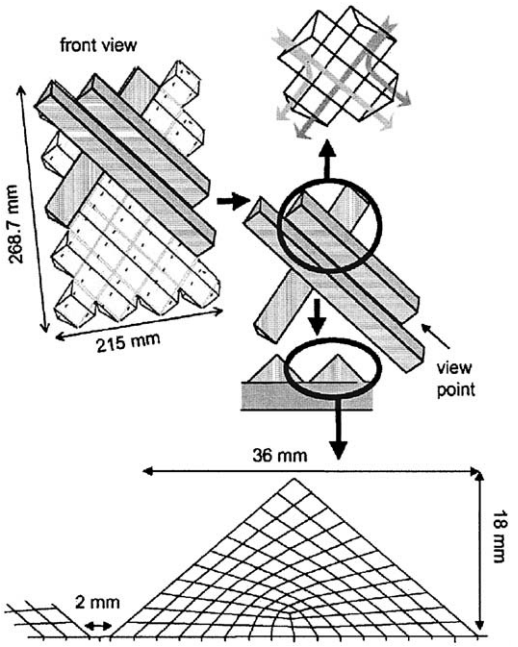

FIG. 15. The KATAPAK-S structure and its computational grid. Reprinted from Chemical Engineering Science, Vol. 56, van Baten *et al*., Radial and Axial Dispersion of the Liquid Phase within a KATAPAK-S® Structure: Experiments vs. CFD Simulations, pp. 813–821, Copyright (2001), with permission from Elsevier.

bound together. An illustration of the "criss-cross" structure is given in Fig. 15 below. The "Toblerone" structure consisting of intersecting and connecting triangular tubes has many similarities with the packings investigated by Petre *et al.* (2003) and Larachi *et al.* (2003) that are discussed above. The computational grid used for the simulations is also shown.

In these simulations, the authors used the pseudo-continuum approach for the catalyst packing inside the criss-cross structure. The body force describing the resistance to flow offered by the packing was modeled by the Ergun equation. The equation of continuity for a tracer was included with the equations of conservation for total mass and momentum, so their simulation tracked unsteady liquid flow through the illustrated assemblage of triangular tubes. Liquid entered the system through the top eight tubes and exited through the bottom eight tubes. At steady state, a pulse tracer was injected and tracer outlet concentrations were monitored to obtain the RTD curves at different horizontal positions. From these the axial and radial dispersion coefficients were estimated. The authors found good agreement between the coefficients estimated from CFD simulations and those estimated from experiments, and determined that the radial dispersion coefficient for the KATAPAK-S was about an order of

magnitude higher than that in co-current down-flow trickle beds, which represented a desirable feature.

Dispersion in conventional packed beds of spheres has also been simulated by CFD. Manz *et al.* (1999) compared lattice Boltzmann simulations to NMR velocimetry and propagator measurements. Their flows were at $0.4 < Re < 0.77$ with $182 < Pe < 350$. Over these ranges, they evaluated contributions to the dispersion tensor: mechanical dispersion, i.e., dispersion arising from the stochastic variations of the velocity field due to the structure of the packing; Taylor dispersion, i.e., diffusion of fluid molecules across streamlines; and holdup dispersion, caused by blocked regions of flow in the packing. At larger length scales, dispersion was dominated by mechanical dispersion, while at smaller length scales dispersion was determined by Taylor dispersion. At the largest length scales, they suggested that holdup could play a significant role.

Zeiser *et al.* (2001) also used LBM to examine dispersion. They simulated a simple cubic packing only one sphere wide, with periodic boundary conditions perpendicular to the main flow direction to emulate an infinite array, and 40 spheres in the main flow direction to allow dispersion to develop. A pulse was simulated across the transverse plane, which eventually became Gaussian and allowed extraction of the longitudinal dispersion coefficient. They obtained a correlation in terms of $Pe^{1.83}$, whereas Taylor dispersion would predict Pe^2. This may mean that similarly to Manz *et al.* (1999), mechanical dispersion begins to play a role even at quite low Re. In a more recent paper (Freund *et al.*, 2005) the same group used LBM to obtain flow fields in a simple cubic packing of spheres, and in a random packing of $N = 5$. They then used a particle tracking algorithm, together with the flow fields, to obtain 3D concentration fields from which they obtained axial and radial dispersion coefficients. They found good agreement with experiment for dispersion in the cubic array, for which flow was relatively simple, but for the more complex flows in the random bed the agreement was less good, although still reasonable compared to the scatter of the data. Freund *et al.* (2005) also performed simulations that gave residence time behaviour, and warned that the residence time and dispersion coefficients obtained from the popular tracer injection technique could depend on the tracer injection location.

Dispersion in packed tubes with wall effects was part of the CFD study by Magnico (2003), for $N = 5.96$ and $N = 7.8$, so the author was able to focus on mass transfer mechanisms near the tube wall. After establishing a steady-state flow, a Lagrangian approach was used in which particles were followed along the trajectories, with molecular diffusion suppressed, to single out the connection between flow and radial mass transport. The results showed the ratio of longitudinal to transverse dispersion coefficients to be smaller than in the literature, which may have been connected to the wall effects. The flow structure near the wall was probed by the tracer technique, and it was observed that there was a boundary layer near the wall of width about $d_p/4$ (at $Re_i = 7$) in which there was no radial velocity component, so that mass transfer across the layer

would be by molecular transport only. At higher flow rates the layer was too thin to be resolved by the author's structured mesh, but even at $Re_i = 200$ it was noted that the tracer particles were not easily transported across the region one sphere diameter thick next to the wall. Maier *et al.* (2003) also investigated wall effects on hydrodynamic dispersion using LBM for tubes at higher N, in the range 10–50, but at relatively low *Re*. They also found that the presence of the tube wall enhances dispersion, due to the effects on bed structure and velocity profile.

The inclusion of chemical reaction into CFD packed-tube simulations is a relatively new development. Thus far, it has been reported only by groups using LBM approaches; however, there is no reason not to expect similar advances from groups using finite volume or finite element CFD methods. The study by Zeiser *et al.* (2001) also included a simplified geometry for reaction. They simulated the reaction $A + B \rightarrow C$ on the outer surface of a single square particle on the axis of a 2D channel (Fig. 16).

The chemical species were treated as passive scalar tracers in the unsteady LBM equations. The reaction was simulated as being mass-transfer limited at low $Re = 166$, with diffusivities in the ratios $D_A : D_B : D_C = 1 : 3 : 2$. The concentration fields shown in Fig. 16 are different for each species due to the different diffusivities. The slow-diffusing species A is transported mainly by convection and regions of high or low concentration correspond to features of the flow field. A more uniform field is seen for the concentration of faster

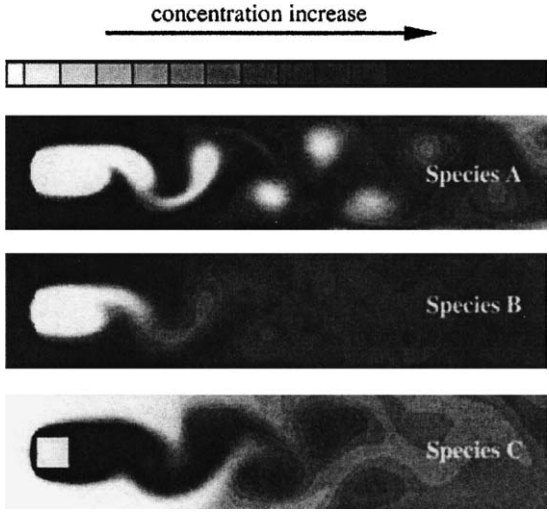

FIG. 16. Snapshot of the 2D concentration field for reactive fluids. Reprinted from Chemical Engineering Science, Vol. 56, Zeiser *et al.*, CFD-Calculation of Flow, Dispersion and Reaction in a Catalyst Filled Tube by the Lattice Boltzmann Method, pp. 1697–1704, Copyright (2001), with permission from Elsevier.

diffusing species B, while species C with intermediate diffusivity has a concentration field between the other two. The main conclusion was that the inhomogeneous flow field led to a nonuniform concentration distribution around the particle, in contrast to the usual assumption of uniform surroundings for catalyst particles in standard reactor models.

A sequel to this study was presented later by the same group (Freund *et al.*, 2003), this time for the simple first-order reaction $A \rightarrow B$ in a cylindrical bed of spheres with $N = 5$. The reaction was again taken to be mass-transfer limited and to occur on the surfaces of the catalyst particles, but at a very low flow rate at $Re = 6.5$. It was found that concentration peaks occurred near the wall at values close to the inlet value of species A, indicating that channeling was taking place. There were also local peaks of product concentration that indicated areas of high reactivity that could give rise to hotspots in practice.

Yuen *et al.* (2003) used MR visualization techniques to obtain information on local chemical conversion for the liquid-phase esterification of methanol and acetic acid in an optically opaque 3D fixed bed of catalyst spheres. They used LBM simulations to obtain a flow field within the fixed bed of catalyst, which was validated by comparison to flow data also obtained from MR visualization. Their experimental data showed significant fractional variations in conversion in the tube, at the same axial planes, which they were able to relate to heterogeneities in the flow field. They compared local conversion and locally averaged fluid velocity over various length scales. When correlating over the length scale of the entire bed, the effects of local fluid mixing were lost in comparison to heterogeneities in the macroscopic flow field. Correlations at the smallest length scale, the size of the packing (about 600–850 μm) showed only a weak link between flow and conversion, as local mixing caused by the bed structure was incomplete at this scale. An intermediate scale of 1.5 mm × 1.5 mm × 500 μm gave a correlation between the conversion and velocity data that was well fitted by a model based on the assumption of a kinetically controlled esterification reaction. A suggested explanation for this result was that over these volumes effective mixing between fluid streamlines had occurred.

C. Heat Transfer

There are only a few research groups that investigate heat transfer in packed tubes using CFD, as it involves larger models, and the LBMs cannot, at present, accommodate the energy balance. The added complication of meshing the solid particles for the conjugate heat transfer problem makes heat transfer CFD studies more computationally expensive. Most heat transfer CFD work is done in small sections of packing, representing REUs or periodic elements of the bed.

Lund *et al.* (1999) reported finite element simulations of conduction between two contacting spheres without fluid flow. They modeled a small separation between the spheres to allow for interparticle micro-asperity gaps, and then the

thermal conductivity of some of the center-most gap gas elements was increased to that of the solid particles, to include the effect of deformation contact area. From the CFD simulations they derived a correlation for effective bed thermal conductivity that included the effects of the micro-asperity fluid gap, the deformation contact diameter, and the thermal conductivities of solid and fluid. They also considered different packing arrangements to obtain the dependence on bed voidage.

One of the earliest heat transfer problems addressed by CFD is the particle-to-fluid heat transfer coefficient. Many experimental studies had disagreed on the limiting value of the particle to fluid Nusselt number ($Nu_p = h_p d_p/k_f$) as Re decreased to zero. The work of Sørensen and Stewart (1974) provided definitive calculations for creeping flow that gave the limiting value for spheres in a cubic packing, and showed that it should be nonzero. CFD simulations at higher Re for simple cubic and face-centered cubic arrangements were performed by Gunjal *et al.* (2005). Their results for the FCC packing were in reasonable agreement with literature correlations as far as the magnitude of Nu_p, but the trend with Re was somewhat different. The simulations for the SC packing gave Nu_p values well below the predicted ones. The authors explained these differences by the different flow structures in the interstitial space for the different packing arrangements.

Some investigators have considered the particle-fluid heat transfer for a single particle in an infinite medium or in a channel. This is a useful case for the testing of CFD models and grids, as analytical solutions are available for the limiting case $Re \to 0$. Romkes *et al.* (2003) simulated particle–fluid heat transfer for a single particle in tubes of various sizes intended to approach an infinite domain, and also for composite structured packings (CSP) made up of square channels packed with spheres to give $1 < N < 2.05$. They also carried out mass transfer experiments with CSP using sublimation of naphthalene from test particles. The CSP structures are designed to reduce pressure drop for packed bed reactor operations, but this also has the effect of reducing heat and mass transfer rates between particle and fluid. Therefore, it is important to test existing correlations for these transport coefficients, and develop new ones if needed.

For the single sphere, Romkes *et al.* (2003) found that over the range $1 < Re < 10^5$ the average heat transfer rate computed by CFD was within 10% of that predicted by well-established literature correlations. They also found that the local heat transfer rate varied along the sphere surface and depended on the angle relative to the stagnation point, in qualitative agreement with prior work. They presented this dependence for high and low Re and showed flow and heat transfer maps for various Re. For the CSP simulations, ''test'' particles with higher surface temperatures were simulated, analogously to the mass transfer experiments. The authors found that consistent results were obtained for different locations and numbers of active particles, as long as they were not in the first two layers, for which the flow field had not established periodic behavior, or

the last layer in the tube, for which exit effects had an influence. Good agreement with experiment was obtained when simulated Nusselt numbers were compared to experimental Sherwood numbers, to about 15%. Correlations were obtained for each packing (N value) separately, and an overall correlation for $N < 2.00$. The main lesson learned was that low-N beds are special cases, the usual packed-tube particle-fluid transport correlations deviated considerably from both experiment and CFD simulation.

Our own group's work has focused on wall-bed heat transfer in low-N fixed bed tubes. At the high flow rates of industrial practice in such applications as partial oxidation and steam reforming, the bulk of the resistance to radial heat transfer lies in the vicinity of the tube wall; hence, this is a very important problem. The standard approach to modeling radial heat transfer has been to conduct experiments in heated or cooled tubes, measure radial temperature profiles at various axial positions in the tube, and fit a 2D pseudo-homogeneous model for temperature, under the assumption of plug flow. The fitting parameters have been the effective radial thermal conductivity, k_r, and the apparent wall heat transfer coefficient, h_w. The model equations and a discussion of the limitations of this effective or lumped approach have been presented recently (Dixon and Nijemeisland, 2001), although there are literally hundreds of papers presenting variations on the experimental techniques, the types of model fitted, and the theoretical justifications. Despite this effort, it is generally accepted that approaches to wall heat transfer are empirical and in strong disagreement with each other.

Our initial hopes for the use of CFD for packed-tube simulation were to generate more accurate and consistent radial temperature profiles, free of experimental artifacts, from which better estimates of k_r and h_w could be obtained. In our earliest work we estimated these parameters in dimensionless form as k_r/k_f and Nu_w ($= h_w d_p/k_f$), from temperature fields for flow around small clusters of three particles (Derkx and Dixon, 1996) and eight particles (Logtenberg and Dixon, 1998a). This work was later extended to include the effects of temperature-dependent fluid properties (Logtenberg and Dixon, 1998b) and to a cluster of ten contacting particles (Logtenberg *et al.*, 1999). The results from these studies showed reasonable agreement in magnitude between the parameters estimated from the CFD simulations, and values predicted from commonly used correlations. Trends with Re were followed reasonably well for k_r/k_f but were off for Nu_w, which could be attributed to the use of small clusters of particles that could not fully represent the flow patterns of full beds. We would now regard these efforts as early attempts to check if CFD gave reasonable results for the bed-scale temperature field, by comparing the derived heat transfer parameters to literature values.

With increased computer power, our next step was to construct full beds of particles: $N = 2$ for validation studies as described above in Section II.D.2, and $N = 4$ for further investigation of the temperature fields and near-wall transport processes as described above in Section II.B.2. Some early flow maps and path

lines were given in Dixon and Nijemeisland (2001) while temperature fields were reported in Nijemeisland and Dixon (2004). The intention was to extract radial temperature profiles and fit the pseudo-homogeneous model to estimate the heat transfer parameters as previously. Similar work has been published recently by Guardo *et al.* (2004, 2005). However, we soon faced a dilemma—How should the CFD-generated radial temperature profile be sampled? The steep increase in temperature near the wall, which had been far less apparent in cluster geometries, could not be fitted by the standard model for the case of a complete $N = 4$ bed. This problem was well illustrated by Von Scala *et al.* (1999) for the structured packing KATAPAK-M®. Fig. 17 shows an example of this difficulty.

In this figure, dimensionless temperature is plotted against dimensionless radial coordinate. Twelve experimental data points are shown, and curve (a) is fitted by the usual methods to these points. It clearly does not fit as well as we would like either in the bed center or near the wall, due to the limitations of the underlying model. The intercept at $r/R = 1$ provides the temperature difference used to define the wall coefficient h_w. If an extra point were available closer to the wall (marked as "speculative" in Fig. 17), such as might be provided by CFD simulations, then the fit to all points results in curve (b). This clearly fits the data set even worse than curve (a) and gives a significantly different intercept and resulting h_w. So, the parameter values that are estimated depend on the location of the measured values. A more consistent approach might be to drop the measurements closest to the wall, as for curve (c) shown, in which this has been done for the three experimental points closest to $r/R = 1$. This would have the merit of at least fitting the bed center temperatures well, and the parameter estimates would have a greatly reduced dependence on the measurement locations. The fitted profile would be quite inaccurate near the wall,

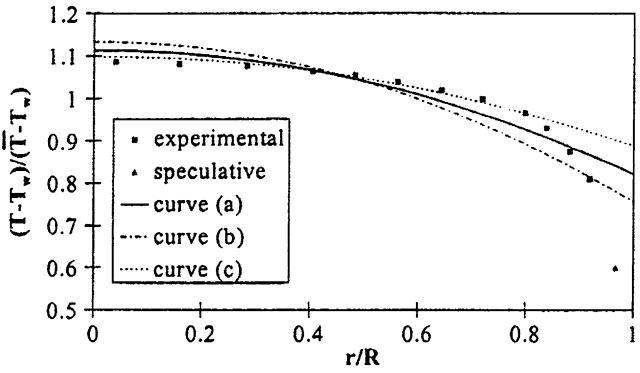

FIG. 17. Least squares fits of the radial temperature profile in KATAPAK-M. Reprinted from Chemical Engineering Science, Vol. 54, von Scala *et al.*, Heat Transfer Measurements and Simulation of KATAPAK-M Catalyst Supports, pp. 1375–1381, Copyright (1999), with permission from Elsevier.

however. A decision would also have to be made as to which measurements to accept for fitting.

From this illustration we can see that the added detail of the radial temperature profile near the wall that could be provided by CFD simulations does not help in obtaining better estimates for the standard heat transfer parameters. It also implies that experimental efforts to measure temperatures closer to the wall are, in fact, counter-productive. Finally, it is clear that the standard model with plug flow and constant effective transport parameters does not fit satisfactorily to temperature profiles in low-N beds. These considerations have led us to look for improved approaches to near-wall heat transfer.

At this stage it seemed clear that to improve near-wall heat transfer modeling would require better representation of the near-wall flow field, and how it was connected to bed structure and wall heat transfer rates. Our early models of full beds of spheres at $N = 4$ were too large for our computational capacity when meshed at the refinement that we anticipated to be necessary for the detailed flow fields that we wanted. We therefore developed the WS approach described above in Section II.B.3.

In Fig. 18, flow path lines are shown in a perspective view of the 3D WS. By displaying the path lines in a perspective view, the 3D structure of the field, and of the path lines, becomes more apparent. To create a better view of the flow field, some particles were removed. For Fig. 18, the particles were released in the bottom plane of the geometry, and the flow paths are calculated from the release point. From the path line plot, we see that the diverging flow around the particle-wall contact points is part of a larger undulating flow through the pores in the near-wall bed structure. Another flow feature is the wake flow behind the middle particle in the bottom near-wall layer. It can also be seen that the fluid is transported radially toward the wall in this wake flow.

The second picture in Fig. 18 shows a temperature map for a vertical plane in the middle of the WS. The tube wall is to the right of the picture, and the scale has been chosen to emphasize the temperature gradients in the near-wall region.

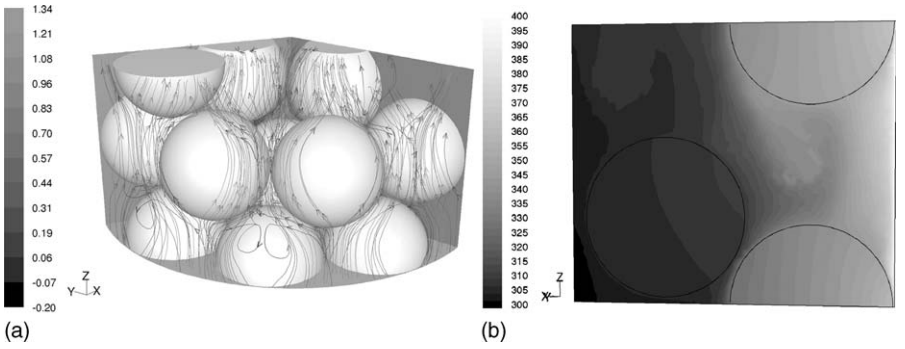

FIG. 18. Path lines and a temperature map in the WS geometry.

Outlines of some of the particles are shown for reference. The boundary layer next to the wall is clearly visible (lightest shade), while the progression of the temperature field through the solid particles can also be seen. The temperature field is observed to be 3D, with features that do not depend on the radial coordinate alone.

When we want to look at the connection between the flow behavior and the amount of heat that is transferred into the fixed bed, the 3D temperature field is not the ideal tool. We can look at a contour map of the heat flux through the wall of the reactor tube. Fig. 19 actually displays a contour map of the global wall heat transfer coefficient, h_0, which is defined by $q_w = h_0(T_w - T_0)$ where T_0 is a global reference temperature. So, for constant wall temperature, q_w and h_0 are proportional, and their contour maps are similar. The map in Fig. 19 shows the local heat transfer coefficient at the tube wall and displays a level of detail that would be hard to obtain from experiment. The features found in the map are the result of the flow features in the bed and the packing structure of the particles.

From Fig. 19, it is clear that the structured packing near the wall causes a pattern in the wall heat flux. To indicate the repeating sections lines were added in Fig. 19. The dotted lines connect the particle–wall contact points, the horizontal line connects these contact points of spheres in the same layer, and the vertical dotted lines connect particle–wall contact points from spheres of alternating layers. The section indicated by the solid box is the repeating section selected for further investigation. The right-hand side of the box is centered at a sphere-wall contact point and the left-hand side of the box is in between contact points. The height of the box is identical to one packing-layer height.

For relating the wall heat flux and the near-wall flow patterns quantitatively the separate pieces of information had to be linked. Detailed information on the

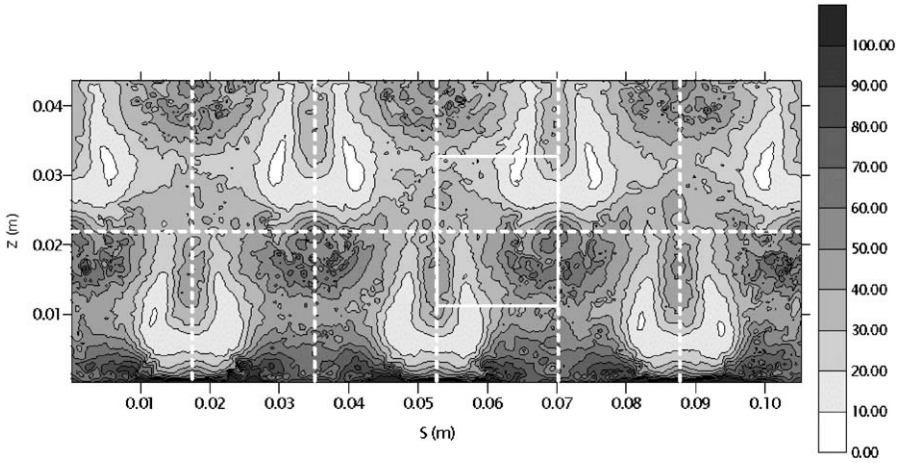

FIG. 19. Map of wall heat transfer coefficient for $N = 4$ bed of spheres.

near-wall flow field was available in conjunction with an equally detailed map of the wall heat flux, similar to Fig. 19. Each surface cell in a repetitive section of the wall was linked directly to a number of fluid volumes with similar tangential and axial coordinates, up to about 5 mm into the fluid. In this way we could probe on a small scale whether the wall heat flux from each surface mesh element (about 1.3 mm in size) could be linked to the corresponding local flow features. Unfortunately, it was found that the quantitative comparison of near-wall flow features with the local wall heat flux by itself did not show enough distinct features to identify any trends. A number of features of the flow field were tried, such as velocity components, vorticity components, helicity, and velocity component derivatives. No correlations were found for any of these quantities, suggesting that we cannot relate wall heat flux to local flow field on this length scale.

By reducing the flow features to simple component magnitudes, larger scale patterns such as the flow path were lost. To test whether wall heat flux could be related to flow patterns on a larger length scale, a conceptual comparison was made using the near-wall repetitive section with the wall heat flux map, as shown in Fig. 19. To capture the 3D volume of the near-wall flow features, the flow field was simplified to a cartoon and the foremost features of the flow were identified. When the flow features were compared to the wall heat flux, it could be seen that the areas of low wall heat flux were located in the parts where the main through-flow and the wake flow met. The high wall heat flux areas were mostly located near the sphere-wall contact point and just upstream from that area. The area just upstream from the contact point had a diverging flow, consisting of strong axial and tangential components; the wake flow, however, was also characterized by strong tangential flow, but combined with radial flow. When the flow features were separated by component, as was done in the quantitative analysis, these connections were lost. So, analysis at the length scale of a particle was able to reveal connections between flow and wall heat flux (Nijemeisland and Dixon, 2004).

The results of the analysis described above have suggested that to lump all the near-wall heat transfer mechanisms into a wall heat transfer coefficient idealized at the wall is too simple an approach for low-N beds. One of our approaches will be based on separating the three main contributions to the extra resistance in the near-wall region: the viscous boundary layer, the decrease in stagnant conductivity of the bed due to decreasing solid fraction, and the reduction in radial convective transport due to increased channeling and changed flow patterns near the wall. We intend to use full-bed simulations to generate temperature fields such as those shown in Fig. 20, for $N = 4$.

The temperature maps shown in Fig. 20 illustrate the development of the temperature field as the flow enters a tube heated at the wall. The first (left-hand) map shows the initial heating of the gas at the tube entrance. The development of the boundary layer near the walls is clear and represents one contribution to the heat transfer resistance in the wall region. The more rapid

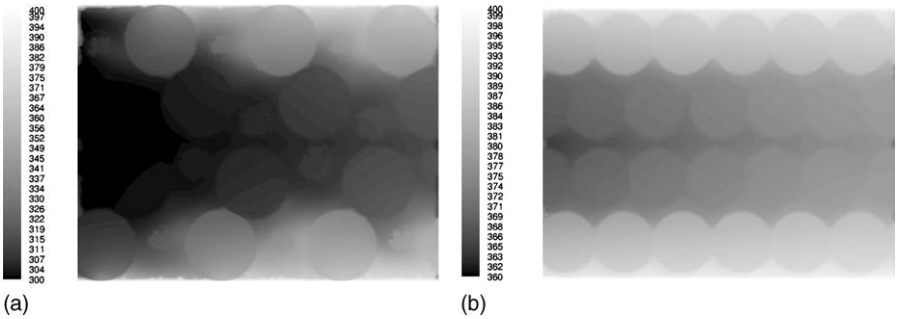

FIG. 20. Temperature contour maps of respectively the $x = 0$ plane of the first stage in the $N = 4$ geometry stacking, and the $y = 0$ plane of the fourth stage. Main axial flow direction moves from left to right in these pictures.

penetration of higher temperatures into the bed through the solid particles due to their higher thermal conductivity is also well shown. In the second (right-hand) temperature map the arrangement of the spherical particles around the tube wall is illustrated, and the more developed temperature field further down the tube. The more uniform temperatures in the bed center, due to convective heat transfer, are evident, as are the temperature gradients across the first layer of particles next to the wall. The proper choice of simulation conditions will allow us to separate the individual contributions due to the separate heat transfer mechanisms, and our early results in this direction are promising (Leising, 2005).

IV. Catalyst Design for Steam Reforming Using CFD

A. Steam Reforming and Principles of Catalyst Design

The steam reforming of methane to produce synthesis gas is becoming a particularly important reaction recently, due to the increased availability of natural gas as a feedstock. The use of reformed gas has historically been dominated by hydrogen manufacture for commercial use, or for ammonia and methanol synthesis. Of increasing importance, however, is the manufacture of liquid fuels from remote or stranded natural gas using Fischer Tropsch chemistry, and the generation of hydrogen from natural gas liquid fuels to power mobile and stationary fuel cells. The syngas generation section of such plants comprises over 50% of the capital cost (Abbott *et al.*, 1989). There is thus a strong economic incentive to develop more efficient steam reforming technology, and a major step in this effort is the optimal design of catalyst particles (Stitt, 2005).

Steam reforming is traditionally carried out in large fired furnaces containing many catalyst-containing tubes. There are several requirements in reforming that might normally be considered mutually incompatible:

- Low pressure drop and thus high voidage and large particles
- High surface area for high activity which normally requires small particles
- Good radial mixing for heat transfer that requires a large particle
- High strength to avoid breakage during handling and charging (Note that no catalyst is strong enough to resist the stresses of tube contraction during cooling but that the fracture patterns are important to preventing pressure drop build up).

The general outcome of this is that the reforming industry uniformly uses pellets of a length to diameter ratio in the range 0.8–1.2 with internal holes. Catalysts ranging from Raschig rings to pellets with 4 to 10 axial holes are now commonly used. Tube-to-particle diameter ratios also vary but at the entry region where good heat transfer is essential they will normally be 5–10. Smaller catalyst particles tend to be used in the lower portion of the tube where the reaction activity becomes a factor next to the heat transfer. This is especially true of top fired reformers.

A randomly packed tube, see Fig. 21 for example, is geometrically extremely complex and thus hard to represent. The randomness of the packing makes it hard to construct mappings with periodicity.

The impact of the tube-side heat transfer coefficients on the tube wall temperature is shown in Fig. 22: a two-fold improvement in the coefficients facilitates approximately a 40°C lowering of the tube wall temperature.

Tube wall temperature is an important parameter in the design and operation of steam reformers. The tubes are exposed to an extreme thermal environment. Creep of the tube material is inevitable, leading to failure of the tubes, which is exacerbated if the tube temperature is not adequately controlled. The effects of tube temperature on the strength of a tube are considered by use of the Larson-Miller parameter, P (Ridler and Twigg, 1996):

$$P = T\frac{\log(t) + K}{1000} \tag{26}$$

where T = material temperature [K], t = time [h] and K is a material-dependent constant. The value of this parameter is plotted against the rupture stress of the material. Fig. 23 shows the Larson-Miller diagram for a typical cast high temperature alloy (K = 15), validated by the results of rupture tests at standard conditions.

A high tube wall temperature also affects the performance of the catalyst. Higher temperatures lead to increased carbon lay-down on the catalyst and a resultant loss of catalytic activity, as well as potential catalyst breakage. Both

FIG. 21. Randomly packed tube packed with reforming catalyst.

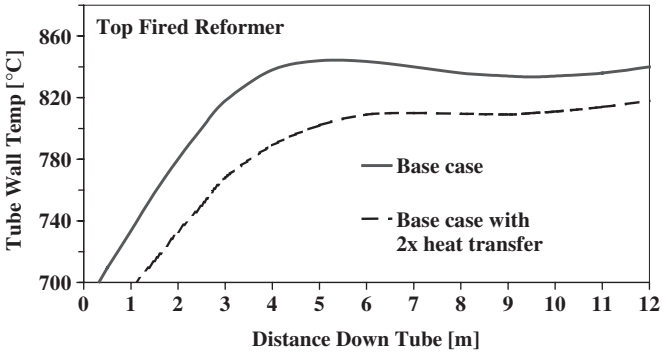

FIG. 22. Impact of tube-side heat transfer coefficients.

lead to a decrease in the local reaction rate. The effective reduction in the reaction-originated heat sink may cause the tube to overheat locally or globally.

The effects of excessive temperatures on reformer tubes are in fact quite dramatic. Fig. 24 shows photographs of reformer tube banks with poor performance and tube over-heating. In Fig. 24a, the flame from the burner is visible in the top of the photograph. On several of the tubes clear evidence of hot bands

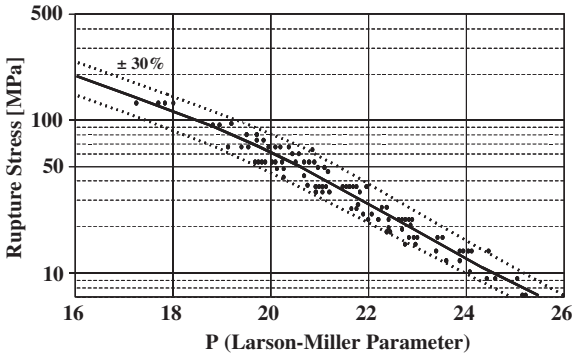

FIG. 23. Larson-Miller diagram summarizing the results of 170 rupture tests on cast 25/20 chrome nickel alloy (adapted from Ridler and Twigg, 1996).

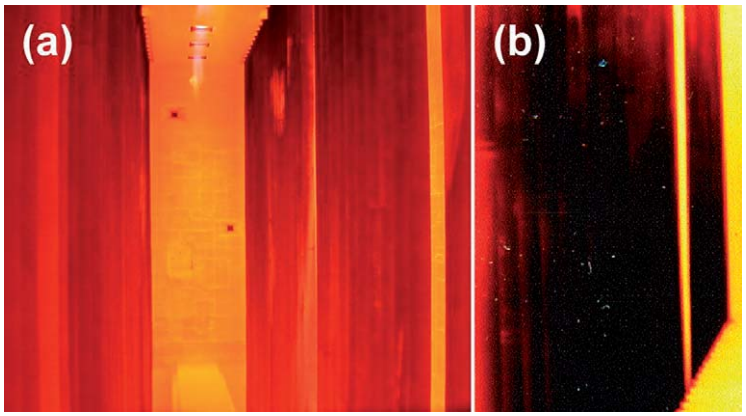

FIG. 24. Photographs of primary steam reformer tube banks showing high tube wall temperature features, (a) showing bands and hot patches and (b) showing an entire tube that has overheated.

and hot patches can be seen. These may be the result of local deactivation, or catalyst voids (settling) which lead to loss of the local endotherm and tube failure. In Fig. 24b, a tube can be seen to have overheated over its entire length. This emphasizes the thermally aggressive environment to which the reformer tube is exposed.

From the Larson-Miller analysis, it is possible to derive more easily interpreted information relating to the effects of sustained high temperature on the life of a tube. A common rule of thumb is that a tube wall temperature increase of 20°C will shorten a tube life by over 50%: from its design period of 10 years to less than 5 years. The cost of a typical reformer tube is USD 6 000–7 000. With typical reformer sizes in the order of 300–400 tubes and taking on-site expenditure into account, this puts the cost of a complete re-tube in the range

TABLE 1
BENEFITS OF MODERN CATALYST PELLET DESIGN ON REFORMER PERFORMANCE

	17 mm Raschig Rings	17 mm Raschig Rings	LxD 19 × 14 mm 4-Hole
Plant rate (relative)	100	112	112
Maximum TWT (°C)	921	940	921
CH_4 slip (mol% dry)	4.4	4.8	4.3
Approach to Equilibrium. (°C)	3	6	2
Pressure Drop (kg/cm^2)	2.3	3.1	2.8

USD 5–8 million. Avoidance of high tube temperatures, both globally and locally is therefore at a premium.

The overall effect of catalyst pellet geometry on heat transfer and reformer performance is shown in the simulation results presented in Table 1. The performance of the traditional Raschig ring (now infrequently used) and a modern 4-hole geometry is compared. The benefits of improved catalyst design in terms of tube wall temperature, methane conversion and pressure drop are self-evident.

B. CFD SIMULATION OF REFORMER TUBE HEAT TRANSFER WITH DIFFERENT CATALYST PARTICLES

For the steam reforming reaction, catalyst particles have been developed with internal voids or holes, so as to increase both bed porosity and particle geometric surface area. This results in a lower bed pressure drop and in increased activity for the reforming reaction, respectively. It is not well established, however, what the effect of these features of the catalyst particle would be on wall heat transfer in the tube. Standard heat transfer models characterize the actual particle by using either the diameter of a sphere of equivalent volume to surface area ratio or the diameter of a sphere of equivalent volume, depending on the quantity being correlated. This is a fairly crude approach that can miss the sometimes subtle effects of the particle design on near-wall fluid flow, and thus on convective heat transfer. Our objective in this work was to use CFD to perform a more detailed assessment of the particle design for heat transfer.

Simulations were run in the WS configuration described earlier. Cylindrical particles with length = diameter = 0.0254 m were placed in the segment in an arrangement that approximated the most common situation seen from a series of experimental packings in a transparent tube, with $N = 4$. The arrangement was constrained by the necessity for it to be axially periodic, so that a periodic flow field could be used. Different cases of the same arrangement were studied, in which the particles had different void structures formed by using various numbers and sizes of holes running parallel to the axis of the cylinder and

placed symmetrically about that axis. A standard hole had diameter slightly larger than a quarter of the particle diameter, a "big" hole had diameter twice the standard diameter, while a "small" hole had diameter reduced by a factor $\sqrt{2}$ of the standard diameter. The particles studied were designated as full, 1-hole, 1-bighole, 3-hole, 4-hole, and 4-small-holes, with the obvious interpretation. Symmetry conditions were retained on the sidewalls of the segment geometry, in default of a better alternative. The focus of the simulations was intended to be the cylinders in the center (horizontally) of the segment, which were only marginally affected by the conditions on the side walls (Leising, 2005). The flow and energy simulations were decoupled, so that the flow field was established under isothermal conditions and the temperature field was then established with a fixed flow field. The dependence of the flow on temperature was judged to be small at industrial conditions. The simulation conditions (T, P, x_i) were for the reaction gas at the inlet conditions of a typical industrial methanol plant steam reformer. Details and parameter values are available in the original reference (Nijemeisland *et al.*, 2004).

The flow simulations were run under isothermal conditions at the inlet temperature of the reactor tube T_{in}, with periodic conditions on top and bottom surfaces. The RNG k–ε model was used for turbulence, with nonequilibrium wall functions. Fig. 25a shows typical flow path lines for the 1-hole particles, obtained by simulating the release of marker particles from the planes $r = 0.045\,\text{m}$ and $r = 0.05\,\text{m}$. Releasing the particles from these planes emphasizes the flow patterns near the tube wall. From the path lines it may be seen that the flow is mostly axial, as expected; however, there are regions of flow with a strong radial component, and also regions of backflow (i.e., flow with a negative axial component). The strongly axial flow is found between particles, such as to the right of the central particle. Strong radial components are found when the flow is displaced by a particle, such as above the central particle. Backflow often occurs in the wake of an obstruction, or where two particles approach closely.

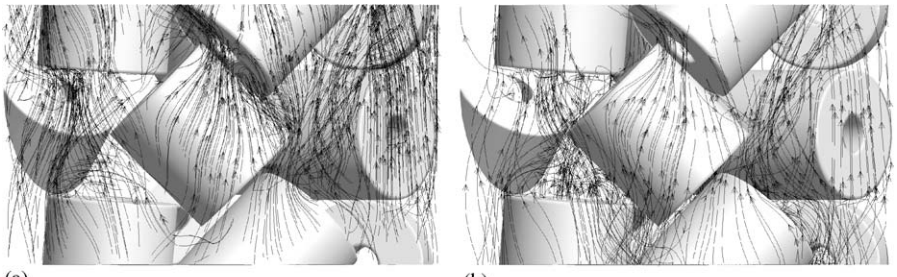

FIG. 25. Wall-segment geometry for 1-hole particles: orthographic projections showing (a) flow path lines for particles released from vertical planes close to the tube wall; (b) flow path lines for particles released from the bottom horizontal plane.

In Fig. 25b, the simulated marker particles were released from the bottom surface, which generates path lines that show more detail of the flow inside the WS, at lower radial coordinate values. The path lines reinforce the trends seen in Fig. 25a, and it is also possible to see some evidence of flow through the center voids of the particles. Most evident is the mix of spiraling and axial flow between the center front and center right particles.

It is of interest to determine the extent to which there is flow through the interior holes of the particles, as the reaction activity is proportional to geometric surface area under these conditions. So, it is important to know whether the extra surface area provided by the holes is accessible to the flow. It is not easy to see this internal flow from the path lines in Fig. 25, although there appears to be flow through the center particle. To determine this more clearly we constructed a surface that passed through the midpoint of the center particle, perpendicular to its axis, for each of the particle geometries. This is shown as the dark square in Fig. 26, which illustrates the results for the 4-hole particle.

The point of view for Fig. 26 is aligned with the axis of the particle, and the perspective causes the sides of the particle to appear as the outer darker ring of cells and the sides of the holes to appear as skewed rings of darker cells around each hole. Contours of velocity magnitude are shown for the midway point of each hole and demonstrate that there is clearly substantial flow through the voids, but it is not symmetric inside the holes. By summing mass flow rates for

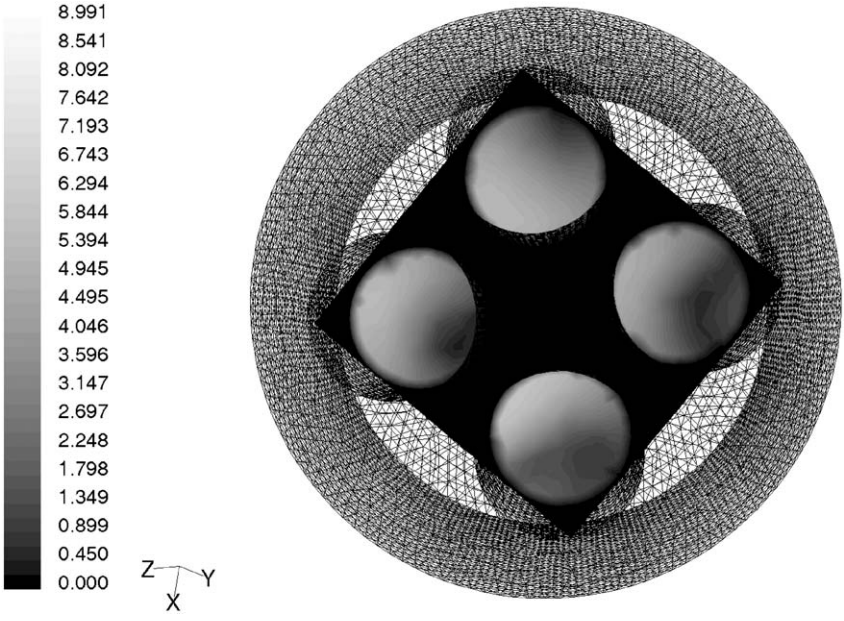

FIG. 26. View of velocity contours down internal voids or holes of the center 4-hole particle.

the four internal cross-sections, we found that slightly over 10% of the total mass flow for the segment actually passed through the interior voids of the center particle. Within each void, the flow rate was higher in that part of the hole that was toward the top of the particle, i.e., at the higher Z-coordinate. It should be noted that the particles simulated here were quite large, and so were the internal voids, as is typical for steam reforming. This result should not be extrapolated to other applications with smaller particles and voids, which may present much higher resistance to internal flow.

The simulations for temperature did not use periodic axial boundary conditions, as the long-term objective was to incorporate heat sinks into the particles (see next subsection). Instead, the technique of virtual stacking was used, as has been described above. All results were from the third segment in the stack and used a tube wall boundary condition of constant wall heat flux, with the inlet fluid temperature for the first stage set to the uniform T_{in} used for the flow simulation, and the top and bottom solid surface heat fluxes set to zero. The outlet fluid required no thermal boundary condition. Each subsequent stage used the outlet temperature field from the previous stage as the inlet fluid temperature field, and the first two stages were regarded as being present to overcome thermal entry effects and to give a more developed radial temperature profile for the third stage comparisons of the particles. The fluids thermal properties were those of the reforming mixture, the solid thermal properties were those of alumina, and radiation was neglected, having been previously determined to be small.

Fig. 27a shows the temperature field in the fluid adjacent to the tube wall, by means of a temperature contour map. The axes of the map are the axial coordinate Z and the arc length along the curved tube wall, S. The contour map shows one hot region and several colder regions in an overall temperature distribution that was quite moderate. The hotter region in the center of the map is associated with the strong axial flow component found there. The cold region to the left of the center of the map (S-coordinate 0.035–0.045, Z-coordinate 0.02–0.04) corresponds to the position of the curved section of the center particle in Fig. 25. In this area the flow is of average velocity, but has a uniform direction and a reasonable radial component, creating the cooler spot.

The weaker hot region at the left side of the segment (S-coordinate 0.01–0.015, Z-coordinate 0.01–0.04) corresponds again to a part of the WS where a strong uniform axial flow was found, but the radial component of the flow was minimal. The energy being put into the system could not be easily transported into the bed, as the flow was more parallel to the tube wall, which resulted in a higher near-wall temperature and lower energy uptake. Similar features could be found near the right-hand side of the temperature plot (S-coordinate 0.08). The cool spot near the right-hand side (S-coordinate 0.09–0.1, Z-coordinate 0–0.03) is a result of the radial flow into the bed around the particles there.

Fig. 27b gives a more quantitative comparison between the radial temperature profiles for the full, 1-hole, and 1-bighole particles. There is a temperature

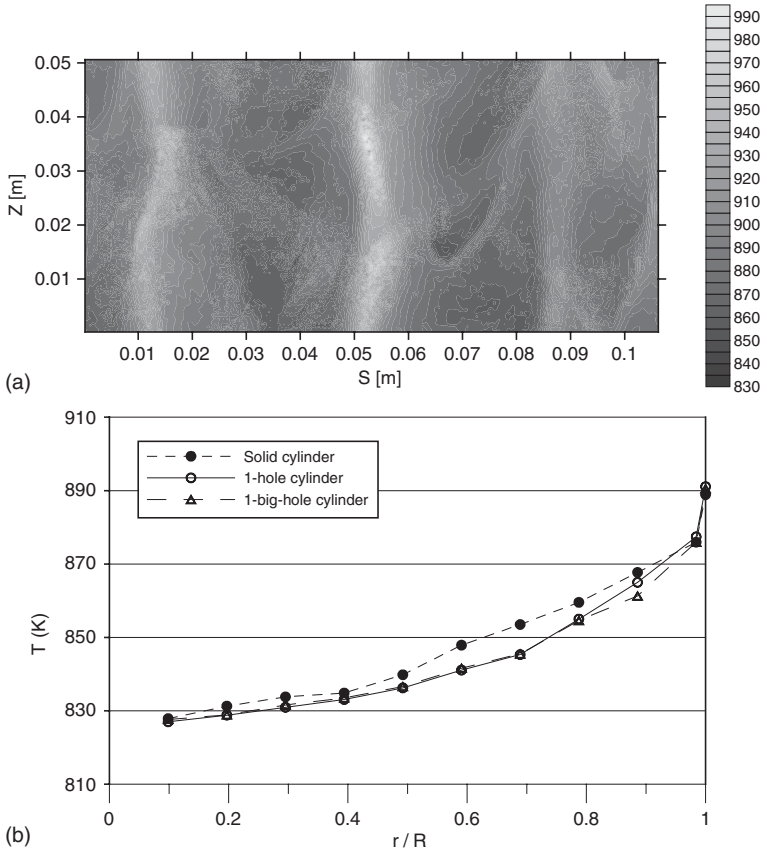

FIG. 27. (a) Near-wall temperature map for the 1-hole particles; (b) radial temperature profiles for solid cylinders and cylinders with two different sizes of internal void.

jump over the viscous boundary layer at the tube wall that is not shown here; the profiles are all for fluid temperatures in the fully turbulent region. The temperature profiles are very similar, with the full cylinders being slightly higher, which implied more effective thermal transport for the simulations shown here. There was little difference between the 1-hole and 1-bighole particles, except toward the tube wall, which was ascribed to the difference in porosity there. It is interesting that there was quite a large difference in flow through the two different 1-hole geometries, which did not translate into a strong difference in heat transfer effectiveness. There is a complex interaction between changes in the amount of solid conduction and radial displacement of flow, which facilitates convective heat transfer. Also, comparisons, such as the above, do not take into consideration the effect of particle geometry on reaction, which will further affect the heat transfer picture by providing heat sinks.

The wall temperature maps shown in Fig. 28 are intended to show the qualitative trends and patterns of wall temperature when conduction is or is not included in the tube wall. The temperatures on the tube wall could be calculated using the wall functions, since the wall heat flux was specified as a boundary condition and the accuracy of the values obtained will depend on their validity, which is related to the y^+ values for the various solid surfaces. For the range of conditions in these simulations, we get $y^+ \approx 13$–14. This is somewhat low for the k–ε model. The values of T_w are in line with industrially observed temperatures, but should not be taken as precise.

Fig. 28a shows the wall temperature map for the 1-hole particles that results if the conduction in the tube wall is omitted from the model. It is quite similar to the temperature map for the near-wall fluid shown in Fig. 27a, and is relatively rich in features such as regions of hot and cold temperatures, which correspond to the local flow field and positions of the particles. The temperatures are considerably higher than in the fluid, reflecting the temperature difference across the viscous boundary layer, which is substantial at the industrial flow rate of this study. There is, correspondingly, a fairly wide range of wall temperatures. Wall conduction was then included in the model, using thermal properties and tube thickness of a typical high-temperature reforming tube made out of a high-alloy steel. The results are presented in Fig. 28b, as a wall temperature map on the same temperature scale as in Fig. 28a. It appears virtually featureless, and all the temperature variations seem to have been smoothed out, due to the thermal conduction in the wall that is now operating. This is misleading, however, as may be seen in Fig. 28c, in which the same temperature field is presented on a scale chosen to bring out the temperature variations. We can see that the features in this map are similar to those of Fig. 28a. The average wall temperatures are the same with or without wall conduction, but the extremes in temperature of Fig. 28a have been strongly mitigated by the wall conduction, as shown in Fig. 28c. The distribution of temperatures still reflects the distribution of temperatures in the neighboring fluid, which in turn reflects the local variation in heat transfer resistance near the wall. Temperature fields within the bed have been shown to be unaffected by the inclusion of conduction in the tube wall (Dixon *et al.*, 2005).

C. Reaction Thermal Effects in Spheres Using CFD

Steam reforming is a heterogeneously catalyzed process, with nickel catalyst deposited throughout a preformed porous support. It is empirically observed in the industry, that conversion is proportional to the geometric surface area of the catalyst particles, rather than the internal pore area. This suggests that the particle behaves as an "egg-shell" type, as if all the catalytic activity were confined to a thin layer at the external surface. It has been demonstrated by conventional reaction-diffusion particle modelling that this behaviour is due to

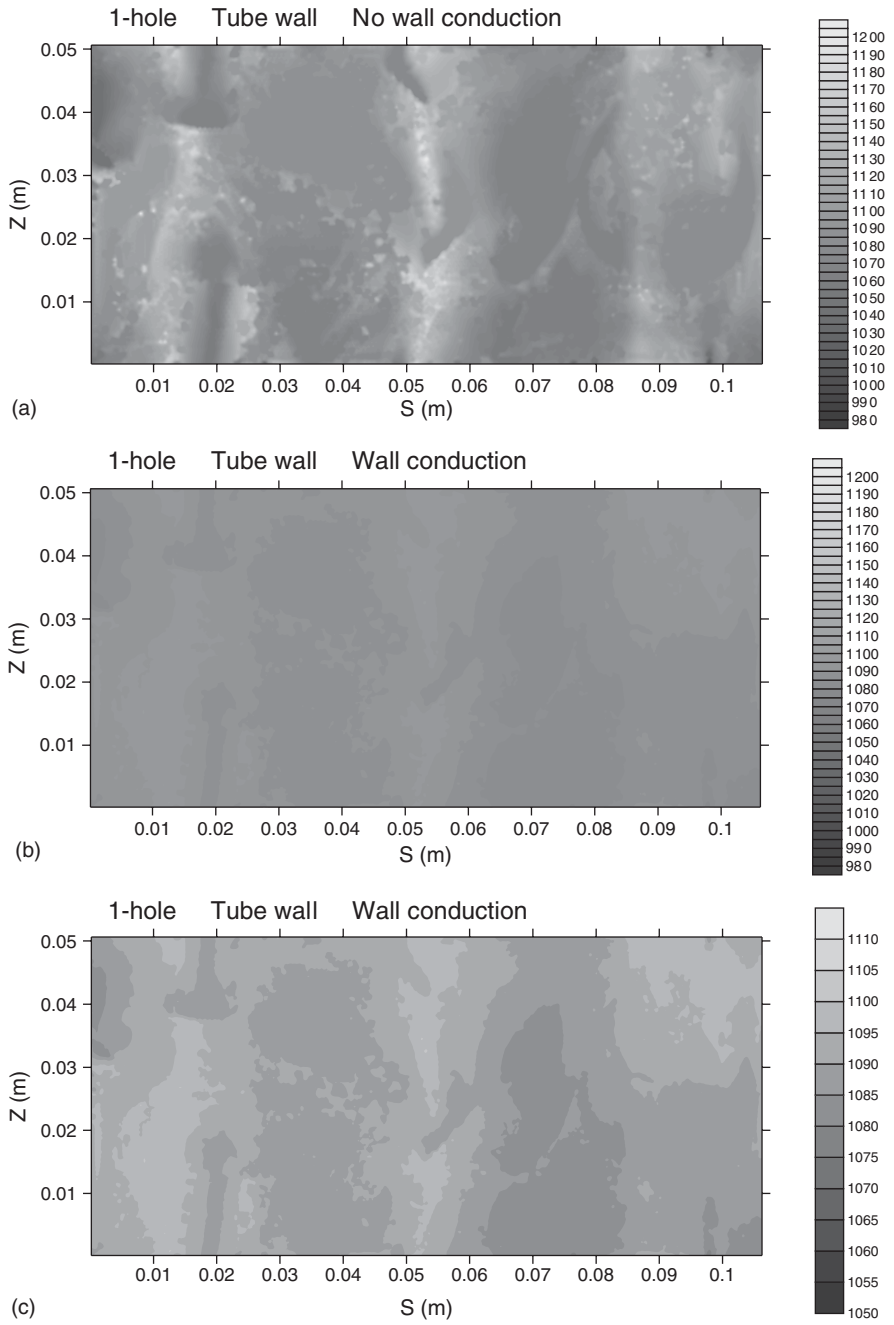

FIG. 28. Wall temperature maps for 1-hole particles (a) without wall conduction; (b) with wall conduction, on the same temperature scale as (a); (c) with wall conduction, on a temperature scale chosen to show nonuniform temperature features.

the extremely strong diffusion limitations under steam reforming conditions (Pedernera *et al.*, 2003).

This study was carried out to simulate the 3D temperature field in and around the large steam reforming catalyst particles at the wall of a reformer tube, under various conditions (Dixon *et al.*, 2003). We wanted to use this study with spherical catalyst particles to find an approach to incorporate thermal effects into the pellets, within reasonable constraints of computational effort and realism. This was our first look at the problem of bringing together CFD and heterogeneously catalyzed reactions. To have included species transport in the particles would have required a 3D diffusion-reaction model for each particle to be included in the flow simulation. The computational burden of this approach would have been very large. For the purposes of this first study, therefore, species transport was not incorporated in the model, and diffusion and mass transfer limitations were not directly represented.

The approach that was used was to represent the energetic effects of reaction through user-defined volumetric heat generation terms. For this approach, the partial pressures of the species in the gas mixture were held constant at the conditions corresponding to the position of interest in the reactor tube, and reaction energy effects were allowed in the catalyst particles in an outer shell only. Thus, the WS was regarded as representing a differential slice of the reactor, with uniform species partial pressures. For each solid phase cell, if the local position of the volume centroid was within an outer shell of the catalyst particle, the reaction rates were calculated at the local solid temperature, and an energy source term was included. The volumetric heat generation rate, Q_p, in units of W/m^3(cat.) was given by the sum of the products of the reaction rates and the heats of reaction. A cut-off value was used so that the reaction heat effects were confined to the outer shell, and a parametric study was carried out on the effects of the choice of the value. This was equivalent to setting the effectiveness factor of the particle.

The simulation was run by first determining the flow solution in the periodic segment, and subsequently determining the energy solution. The solution of flow and energy were decoupled, as the temperature-dependence of the gas properties was not expected to influence flow at the extremely high industrial flow rates simulated here. This assumption allowed the flow to be treated as periodic, independently of the temperature field. The gas heated up slightly as it passed through the segment, and as the reaction rates gave temperature-dependent sinks/sources, the temperature field could not be treated as periodic. The flux through the tube wall of the segment was kept constant. Symmetry conditions were applied to the sides of the WS.

The CFD calculations of the present work used conditions and compositions from a Johnson Matthey detailed reformer model of a methanol plant steam reformer with upwards flow, at typical operating conditions. Conditions were chosen corresponding to three different axial positions along the tube, to reflect reaction rates typical of those close to the inlet, midway down the tube and close

to the outlet. Details of parameter values used in these simulations can be found in the original reference (Dixon *et al.*, 2003).

For our simulations with heat sinks in spheres, we chose not to stack runs, in order to minimize the change in temperature across the WS, and instead carried out a study of the effects of simplified boundary conditions. For most runs, simple boundary conditions were used in which the fluid entering at the base of the segment was set uniformly to T_{in}, and fluxes through the solid areas on the top and bottom planes were set to zero. No thermal boundary condition was required for the flow outlet boundary.

From knowledge of the coordinates of the center points of the spherical particles, we developed a simple criterion to select those control volumes whose centroid lay within the cut-off from the particle surface. We then verified this using a user-defined marker technique as shown in Fig. 29a. In the figure, fluid cells were tagged 0 and are intermediate in shade, solid particle inactive cells were tagged 1 and are the lightest, while the selected solid active cells were tagged 2 and are the darkest. As can be seen, the algorithm correctly selected the cells at the particle edges. The algorithm did not select any interior cells. The appearance of somewhat ragged edges is due to a 2D representation of a 3D situation. A closer look is shown in Fig. 29b. Some tetrahedra appear to be selected that are not at the surface of a particle. In these cases, the centroid of the tetrahedron lies close enough to the surface for the cell to be selected, even though the part of the cell that is intersected by the plane of Fig. 29b appears to lie further from the surface. A similar explanation holds for cells that appear to be next to a surface, but which are not selected, due to the position of the centroid. Examination of the geometry in 3D confirms this interpretation of the picture.

The simulation of the thermal effects of the steam reforming reaction was based on a published reaction model (Hou and Hughes, 2001) for methane

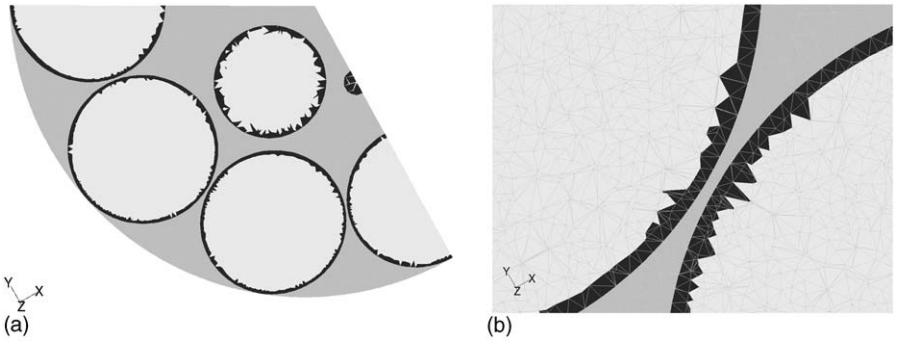

FIG. 29. (a) Midplane cross-section of the WS packed with spheres, showing control volumes found by selection algorithm, marked as darkest cells.; (b) close-up of gap between two spheres, showing cell selection in detail.

reforming over a Ni/Al_2O catalyst. The model is based on the performance of the steam reforming catalyst produced by ICI-Katalco (now Johnson Matthey Catalysts), and consisted of the following three main reactions:

$$1: CH_4 + H_2O = CO + 3H_2$$
$$2: CO + H_2O = CO_2 + H_2$$
$$3: CH_4 + 2H_2O = CO_2 + 4H_2$$

The final rate expressions, which were used in the present work, were given by Hou and Hughes (2001). In these rate expressions all reaction rate and equilibrium constants were defined to be temperature-dependent through the Arrhenius and van't Hoff equations. The particular values for the activation energies, heats of adsorption, and pre-exponential constants are available in the original reference and were used in our work without alteration.

The active shell thickness was determined by the cut-off value r_{cut}, which represented how much of the spherical catalyst particle was active and provided an energy sink/source, depending on the local reaction rates. A position in the particle was regarded as inert if its distance from the particle center was less than r_{cut}. The actual catalyst particles themselves were uniformly impregnated with active metal catalyst. The use of r_{cut} was a device to represent the "egg-shell" nature of the reaction and diffusion in the catalyst particles, in the present study of the energetic effects of steam reforming. It is, therefore, of interest to investigate the effect of different values of r_{cut}, or the equivalent values of the effectiveness factor, η.

The amount of heat actually taken up by the particles was an important quantity, as tubes operate under heat transfer limited conditions near the tube inlet. Fig. 30 shows a plot of Q against η, where Q was the total energy flow into the solid particles, for the entire segment. For inlet conditions, Q varied strongly at lower η, but was almost constant at higher values. As r_{cut}/r_p decreased from 0.95 to 0.0 and the effectiveness factor increased from nearly zero to one, the active solid volume increased by a factor of 7. If the solid temperature had remained the same, the heat sink would also have had to increase sevenfold. This could not be sustained by the heat transfer rate to the particles, so the particle temperature had to decrease. This reduced the heat sink and increased the driving force for heat transfer until a balance was found, which is represented by the curve for the inlet in Fig. 30.

Subsequent to the simulations reported in Dixon *et al.* (2003), some runs were carried out in which the virtual stacking was used, to provide a similar length of heated tube as in the runs without heat sinks, for comparison purposes. Some results for the third segment are given in Fig. 31, which shows a horizontal plane at the vertical midpoint of the WS and a vertical plane at the horizontal midpoint of the WS, under inlet tube conditions. The level of particle activity was $r_{cut}/r_p = 0.95$, which was closest to the egg-shell picture.

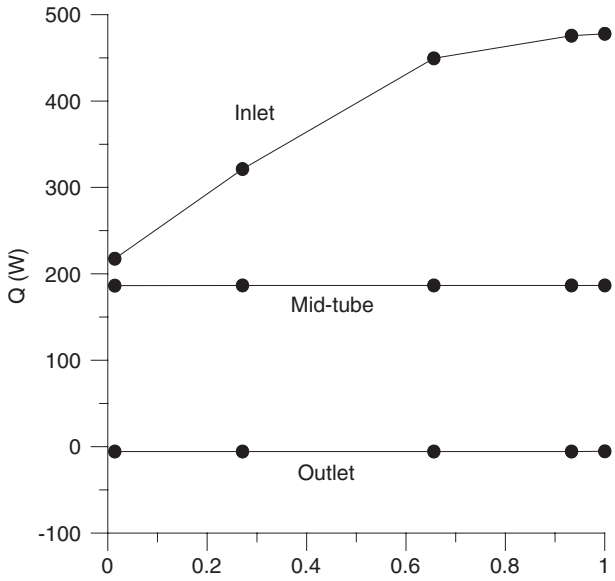

FIG. 30. Heat flow into particles, as a function of effectiveness factor, for the three tube positions studied in Dixon *et al.* (2003).

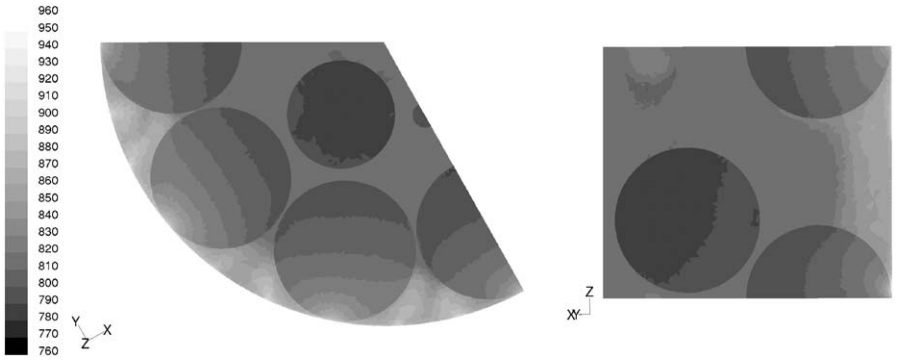

FIG. 31. Horizontal and vertical planes through the third-stacked WS, showing the temperature fields in the fluid and through the spherical catalyst particles, with 5% activity.

We can see that for these conditions, the temperature fields inside the wall particles are far from symmetric. Significant temperature incursions appear inside the spheres, and the influence of the wall is strong. The spheres are hotter close to the tube wall than on the side facing the center of the segment. The interior particles appear to be more symmetrical in temperature. It is noticeable that the particles are considerably lower in temperature than the surrounding

gas, except possibly near a contact point with the wall. This is an expected result of the endothermic reactions.

At the inlet of the reactor tube, the gas mixture is rich in methane and steam with some carbon dioxide. It is also at a relatively low temperature. The water–gas shift reaction (reaction 2) is energetically favored because of its low activation energy, but the reactant carbon monoxide is not present to any significant extent. Of the other two reactions, methane conversion to carbon dioxide (reaction 3) is favored over methane conversion to carbon monoxide (reaction 1) at lower temperatures, as its activation energy E_3 is approximately half the value of that of reaction 1, E_1. Since this is not the desired product mix for synthesis gas, the strategy would be to increase the tube temperatures as quickly as possible to a range where reaction 1 is favored. Reaction 3 is strongly endothermic, and reduces the heat-up rate of the catalyst by providing a heat sink. Thus, efficient heat transfer in the early stages of the tube is essential.

D. Reaction Thermal Effects in Cylinders Using CFD

Our initial work on reaction thermal effects involved CFD simulations of fluid flow and heat transfer with temperature-dependent heat sinks inside spherical particles. These mimicked the heat effects caused by the endothermic steam reforming reaction. The steep activity profiles in the catalyst particles were approximated by a step change from full to zero activity at a point 5% of the sphere radius into the pellet.

To extend these calculations to cylinders is more complicated, as both the position and orientation of a cylinder must be obtained. To do that we followed the sequence of operations used to position each cylinder, as shown in Fig. 32a, for particle 1, the lower front particle in the wall segment (note that wire frames of the previous positions are retained in each sketch for comparison). Similar sequences were available for each of the other particles in the wall segment model.

It was possible to follow the centre point and top centre point under the transformations, and we developed criteria to select those control volumes whose centroid lay within the cut-off from either the curved surface or the flat ends. We then verified this using the same user-defined marker technique as for the spheres, and the results are shown in Fig. 32b. Again, fluid cells were intermediate in shade; solid particle inactive cells were the lightest, while the selected solid active cells were the darkest. As can be seen, the algorithm correctly selected the cells at the particle edges, whether flat or curved. The algorithm did not select any interior cells. The appearance of somewhat ragged edges is again due to a 2D representation of a 3D situation.

Following the verification step, we applied the heat sink methodology to a WS with full cylinders, comprising a flow field solution followed by three virtual

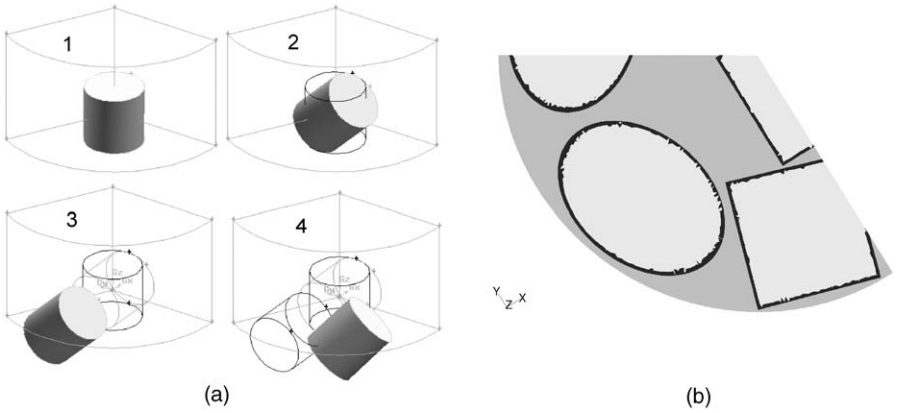

FIG. 32. (a) Sequence of transformations 1→2→3→4 to place bottom front cylindrical particle; (b) Midplane cross-section of the WS packed with cylinders, showing control volumes found by selection algorithm, marked as darkest cells.

stacking thermal simulations. As mentioned previously, the main reason for stacking is to mitigate the effects of a flat inlet temperature profile, and to develop the thermal penetration of the bed. For our simulations with heat sinks in spheres, where we studied the effects of using simplified boundary conditions at the inlet and outlet instead of virtual stacking, we found that the main qualitative features of the solution were not changed, but there was definitely some influence at the detailed level, and on quantitative results. For the work described here, we wished to compare simulations with and without heat sinks, so we chose to use virtual stacking as in our earlier work without heat sinks. This meant that the gas and solids would gradually heat up and depart from the set reactor tube conditions, while the partial pressures stayed constant. We regarded this as one of the simplifications necessary for the heat sinks methodology, which will be eliminated by the development of an improved approach with proper modeling of species diffusion and reaction in the solid particles. We are currently working on such an approach.

Comparisons for the full solid cylinders, with and without heat sinks, were made in Nijemeisland *et al.* (2004) for conditions near the inlet of the reactor tube. These showed that temperature profiles changed drastically when heat sinks were included. In Figs. 33 and 34, we show a similar comparison for conditions typical of the middle of the reactor tube. We compare the planes at the midpoint of the third stage, for the cases where the outer 5% of the particle was active and where the entire particle was inactive. These are shown in Fig. 33.

Both temperature fields shown are on the same temperature scale. As expected, the simulation that included heat sinks resulted in much colder temperatures. With no reaction heat sinks, the temperature field is barely affected by the presence of the particles, despite their higher thermal conductivity, as

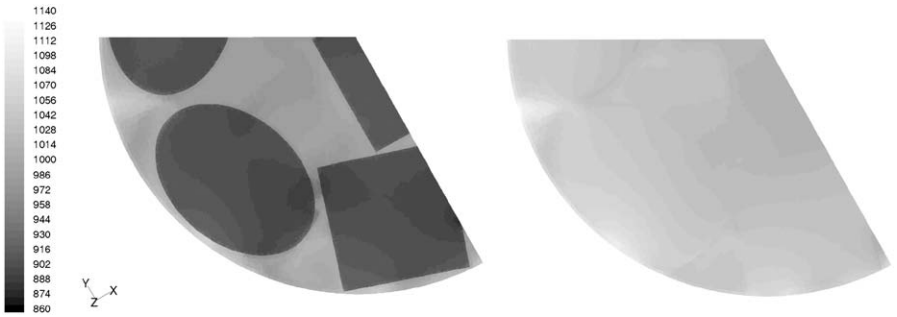

FIG. 33. Comparison of temperature fields in WS midplane for particles with active outer shell (95% inactive, left diagram) and particles with no reaction heat effects (100% inactive, right diagram).

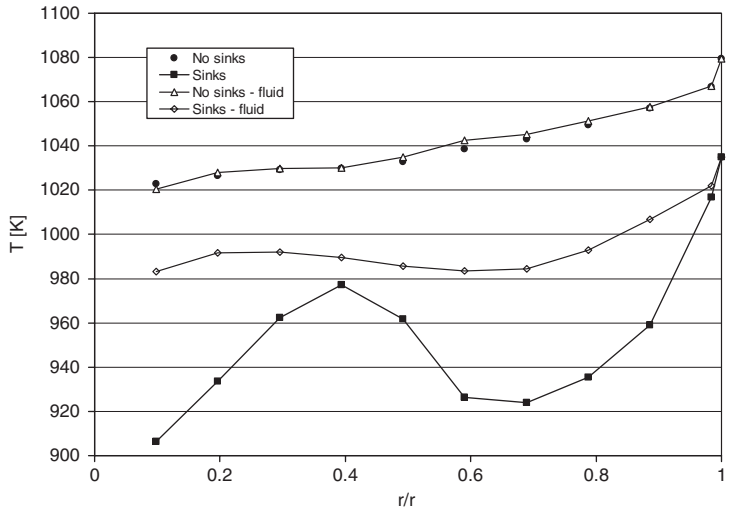

FIG. 34. Comparison of radial temperature profiles for WS packed with full cylinders, with and without heat sinks; solid symbols are for temperatures averaged over fluid and solid, open symbols for temperatures averaged over fluid alone.

shown in the picture on the right. When active pellets are simulated, there is a clear effect resulting in the particles being seen owing to their lower temperatures. It is, however, remarkable that at the level of reaction included in these models, there is still considerable lack of symmetry in the particle temperatures for the cylinders nearest the tube wall. This observation confirms that the assumption of a symmetric temperature field surrounding the catalyst particles could lead to serious errors in estimating reaction rates and modeling the reactor tube.

These qualitative observations can be expressed more quantitatively by examining average radial temperature profiles for the WS, as shown in Fig. 34. The introduction of heat sinks into the catalyst particles decreases the radial temperatures, whether they are averaged over both solid and fluid cells or over the fluid cells alone. If we look at the average fluid temperatures, the heat sinks cause a decrease of about 40–50 K, and the fluid profiles are fairly flat in both cases. For the situation in which there are no heat sinks, the radial temperature profile is almost the same for the fluid and for the fluid and solid combined. This corresponds to the observation in Fig. 32b for the 100% inactive case, in which no differences between fluid and solid could be seen. When heat sinks are included, the solid is much colder, and maxima and minima in the overall averaged profile appear, together with much larger differences in temperature compared to the fluid only profile. It is expected that the shape of the overall temperature profile may be related to the distribution of the solid and its active region; future work will investigate this further.

The extension of this work to include catalyst particles with internal voids is more complex, as there are regions of catalytic activity adjacent to the internal holes, complicating the testing procedure. A comparison of several different catalyst configurations of internal voids has recently been completed, and a description of the method, its verification, and the results obtained will be the subject of a future publication.

V. Future Prospects

This article has attempted to review the issues in applying CFD to simulate interstitial flow in packed tubes, with an emphasis on low-N tubes. The rapid changes in computational capability of today's computers mean that the problems and limitations discussed here will also change rapidly. All we can do is to try to extrapolate where the needs and areas of interest are likely to be in the near future.

There continues to be a need for improved automatic generation of 3D packings, for arbitrary shapes of particles, in cylindrical tubes, and with wall effects present. Since a CFD simulation is based on a single instance of a packing, it is necessary to have the details of that packing readily available. To extend the simulations to consider ensembles of packings, for statistical analysis, would require an easy, inexpensive method of generating the packings.

The LBM has been used to obtain some very interesting results and good insight into packed tube flow, dispersion, and simple reactions. This method however appears to us to have limitations for reactor applications due to its complications in addressing high-Re, nonisothermal situations. Future developments in simulations of catalysis in reactor tubes are likely to be based on the FV-CFD methods. The geometry creation, meshing, and post-processing tools

of the commercial versions of these methods are powerful, and a growing array of turbulence model options promises adequate capability for simulating high-*Re* flows. Abilities to simulate porous regions and species flows are available or are rapidly being added in several packages, in addition to the traditional base of flow and heat transfer.

One area that will be critical for fixed bed modeling is that of wall functions. Owing to the packing, a packed tube flow is dominated by interactions with solid surfaces. As discussed above, resolving turbulent boundary layers will be too expensive for a long time to come, while the demands of the geometry and accurate calculation often make it difficult or impossible to obtain a mesh to satisfy the conditions for wall functions to be strictly applicable. The development of improved wall functions that can work with a range of mesh sizes would be very helpful. Alternatively, several groups have indicated reasonable results and agreement with experimental data from simulations that used meshes and wall functions that were not strictly appropriate. More research is needed on this question.

The research on the flow regimes in packed tubes suggests that laminar flow CFD simulations should be reasonable for $Re < 100$ approximately, and turbulent simulations for $Re > 600$, also approximately. Just as RANS models provide steady solutions that are regarded as time averages of the real time-dependent turbulent flow, it may be suggested that CFD simulations in the unsteady laminar inertial range $100 < Re < 600$ may provide a time-averaged picture of the flow field. As with wall functions, comparisons with experimental data and an improved assessment of what information is really needed from the simulations will inform us as to how to proceed in these areas.

Simulations with representative segments and unit cells employing periodic or symmetry boundary conditions are likely to be necessary for the foreseeable future. Although simulations of complete tube cross-sections would be preferred, these are anticipated to remain too costly for some time to come. This will be especially true for turbulent flows and geometries that require fine meshes or boundary-layer resolution.

The validation of CFD codes by comparison to reliable experiments is of the highest importance. Especially promising is the use of MRI methods to noninvasively provide flow fields and dispersion data. Major challenges will be to extend MRI and similar methods such as LDV and particle tracking to a wider range of conditions, and to develop noninvasive measurements of temperature to improve verification of heat transfer simulations.

Applications of packed tube CFD to improve transport and reaction understanding and models are still in early stages. A number of studies have focused on addressing the technical issues of using CFD for packed tubes, and have presented qualitative results that have yielded insight into the phenomena. Other studies have tried to use CFD simulations to extend experimental data, and provide estimates of familiar transport parameters.

Some of the recent work on structured packings may provide a pointer to future directions for developing models of transport in packed tubes of particles. The identification of REUs in structured packings has provided a fruitful approach to correlating pressure drop. Since low-N packings of particles are also strongly structured due to the wall ordering, can we similarly identify REUs for these tubes, and develop contributions to dispersion and heat transfer? Some of our work on near-wall heat transfer suggests that this may be a way forward, to move on from the current approaches based on neglect of bed structure and empirical correlation of bed effective transport parameters.

The simulation of reacting flows in packed tubes by CFD is still in its earliest stages. So far, only isothermal surface reactions for simplified geometries and elementary reactions have been attempted. Heterogeneous catalysis with diffusion, reaction, and heat transfer in solid particles coupled to the flow, species, and temperature fields external to the particles remains a challenge for the future.

A promising start has been made in packed tube CFD simulation, especially at lower Re and for reduced geometries such as unit cells and bed segments. Applications to transport and catalyst particle assessment are active areas of research. We look forward to the insights that these simulations promise, to more streamlined and easier application of the CFD methods, and to wider applications such as two-phase flow in trickle beds.

Nomenclature

c_p	fluid heat capacity (J/kg$\cdots$K)
C_μ	constant in Eqn. (6) (-)
$C_{1\varepsilon}$, $C_{2\varepsilon}$, $C_{3\varepsilon}$	constants in Eqn. (8) (-)
d_t	tube diameter (m)
d_p	particle diameter (m)
D_i	molecular diffusivity of species I (m^2/s)
E	empirical constant in law of the wall (-)
E_i	activation energy of species i (kJ/mol)
F_i	external body forces component in direction i (N/m^3)
g_i	acceleration due to gravity in coordinate direction i (m/s^2)
G_k	generation of turbulent kinetic energy due to stress ($J/m^3\cdots s$)
G_b	generation of turbulent kinetic energy due to buoyancy ($J/m^3\cdots s$)
h_i	fluid enthalpy of species i (kJ/kg)
H	fluid enthalpy (kJ/kg)
h_o	particle to fluid heat transfer coefficient ($W/m^2\cdots K$)

h_p	particle to fluid heat transfer coefficient ($W/m^2 \cdots K$)
h_w	wall-heat transfer coefficient ($W/m^2 \cdots K$)
J_j	diffusion flux of species i ($kg/m^2 \cdots s$)
k	turbulent kinetic energy (J/kg)
k_P	turbulent kinetic energy at point P (J/kg)
k_f	fluid thermal conductivity ($W/m \cdots K$)
k_r	effective radial thermal conductivity ($W/m \cdots K$)
k_t	turbulent thermal conductivity ($W/m \cdots K$)
K	material-dependent constant (Eqn. 26) (-)
ℓ	eddy length scale (m)
ℓ_d	Kolmogorov dissipation scale (m)
N	tube-to-particle diameter ratio (d_t/d_p) (-)
P	static pressure (Pa)
P	Larson-Miller parameter (K)
q	heat flux (W/m^2)
Q	heat uptake into catalyst particles (W/m^3)
Q_p	heat generation in catalyst particle (W/m^3 (cat.))
r	radial coordinate (m)
r_p	particle radius (m)
R	tube radius (m)
S	arc length (m)
S_h	volumetric heat source ($J/m^3 \cdots s$)
S_m	volumetric mass source ($kg/m^3 \cdots s$)
t	time (s)
T	temperature (K)
T_{in}	tube inlet temperature (K)
T_0	global reference temperature (K)
T_w	tube wall temperature (K)
u'	fluctuating velocity component (m/s)
$\bar{u}$	mean velocity component (m/s)
u^+	dimensionless mean velocity (-)
u^*	dimensionless mean velocity (Eqn. 19) (-)
u_P	mean velocity of fluid at point P (m/s)
v_{in}	inlet velocity (m/s)
v_i	interstitial gas velocity (m/s)
v_0	superficial gas velocity (m/s)
X	coordinate (m)
y	coordinate normal to the wall (m)
y_P	distance from wall to point P (m)
y^+	dimensionless distance from wall (-)
y^*	dimensionless distance from wall (Eqn. 20) (-)
Y_i	mass fraction of species i (-)
Z	axial coordinate (m)

GREEK LETTERS

α_ϕ	relaxation factor for variable ϕ (-)
β	thermal expansion coefficient (K^{-1})
δ_{ij}	Kronecker delta function (= 1 if i = j, 0 otherwise) (-)
ε	turbulence dissipation rate (J/kg$\cdots$s)
ε	bed porosity (-)
θ	dimensionless temperature ($T–T_{in}$)/($T_{wall}–T_{in}$) (-)
κ	von Kármán constant (-)
λ	fluid thermal conductivity (W/m$\cdots$K)
λ_t	turbulent thermal conductivity (W/m$\cdots$K)
μ	fluid dynamic viscosity (kg/m$\cdots$s)
μ_{eff}	effective viscosity (kg/m$\cdots$s)
μ_{mol}	molecular viscosity (kg/m$\cdots$s)
μ_t	turbulent viscosity (kg/m$\cdots$s)
ρ	fluid density (kg/m^3)
σ_k	turbulent Prandtl number for k (-)
σ_ε	turbulent Prandtl number for ε (-)
τ	deviatoric stress tensor (N/m^2)
τ_w	wall shear stress (N/m^2)
υ	fluid kinematic viscosity (m^2/s)
Ω	specific dissipation rate (s^{-1})

DIMENSIONLESS NUMBERS

Particle Nusselt number $Nu = \frac{h_p d_p}{k_f}$

Péclet number $Pe = \frac{\rho v_0 c_p d_p}{k_f}$

Prandtl number $Pr = \frac{c_p \mu}{k_f}$

Turbulent Prandtl number $Pr_{\mathrm{t}} = \frac{c_p \mu_{\mathrm{t}}}{k_f}$

Reynolds number (superficial) $Re = \frac{\rho v_0 d_p}{\mu}$

Reynolds number (interstitial) $Re_i = \frac{\rho v_i d_p}{\mu}$

Reynolds number (effective) $Re_{\mathrm{eff}} = \frac{\rho v_0 d_p}{\mu_{\mathrm{eff}}}$

ABBREVIATIONS

BFD	Brinkman-Forcheimer-Extended Darcy
CFD	Computational Fluid Dynamics
CR	Collective Rearrangement

CSP	Composite Structured Packings
cv	control volume
DEM	Discrete Element Method
DNS	Direct Numerical Simulation
FD	Finite Difference
FE	Finite Element
FV	Finite Volume
LBM	Lattice Boltzmann Method
LDA	Laser Doppler Anemometry
LES	Large Eddy Simulation
MRI	Magnetic Resonance Imaging
RANS	Reynolds-Averaged Navier–Stokes
REU	Representative Elementary Unit
RNG	Renormalized Group
RSM	Reynolds Stress Model
RTD	Residence Time Distribution
SD	Sequential Deposition
TWT	Tube Wall Temperature
WS	Wall Segment

REFERENCES

Abbott, P. E. J., Conduit, M. R., and Mansfield, K. Proceedings of World Methanol Conference, paper 14-1, Crocco & Associates Inc, Houston, TX (1989).
Agarwal, R. *Annual Review of Fluid Mechanics* **31**, 125 (1999).
Benenati, R. F., and Brosilow, C. B. *AIChE J.* **8**, 359 (1962).
Bey, O., and Eigenberger, G. *Chem. Eng. Sci.* **52**, 1365 (1997).
Bode, J. *Comp. & Chem. Eng.*, **18 SUPPL**, S247 (1994).
Bryant, S. L., Mellor, D. W., and Cade, C. A. *AIChE J.* **39**, 387 (1993).
Calis, H. P. A., Nijenhuis, J., Paikert, B. C., Dautzenberg, F. M., and van den Bleek, C. M. *Chem. Eng. Sci.* **56**, 1713 (2001).
Caulkin, R., Fairweather, M., Jia, X., Gopinathan, N., and Williams, R. A. *Comput. Chem. Eng* **30**, 1178 (2006).
Chan, S. K., and Ng, K. M. *Chem. Eng. Comm.* **48**, 215 (1986).
Chen, S., and Doolen, G. D. *Annual Review of Fluid Mechanics* **30**, 329 (1998).
Chu, C. F., and Ng, K. M. *AIChE J.* **35**, 148 (1989).
Craft, T. J., Gerasimov, A. V., Iacovides, H., and Launder, B. E. *Int. J. Heat Fluid Flow* **23**, 148 (2002).
Dalman, M. T., Merkin, J. H., and McGreavy, C. *Computers and Fluids* **14**, 267 (1986).
Debus, C., Nirschl, H., Delgado, A., and Denk, V. *Chem.-Ing.-Tech.* **70**, 415 (1998).
Derkx, O. R., and Dixon, A. G. *Numerical Heat Transfer A* **29**, 777 (1996).
Dhole, S. D., Chhabra, R. P., and Eswaran, V. *Chem. Eng. Res. Des.* **82**(A5), 642 (2004).
Dixon, A. G., and Nijemeisland, M. *Ind. Eng. Chem. Res.* **40**, 5246 (2001).
Dixon, A. G., Nijemeisland, M., and Stitt, E. H. *Int. J. Chemical Reactor Eng.* **1**, A11 (2003).
Dixon, A. G., Nijemeisland, M., and Stitt, E. H. *Ind. Eng. Chem. Res.* **44**, 6342 (2005).

Dybbs, A., and Edwards, R. V., "Fundamentals of Transport Phenomena in Porous Media" (J. Bear, and M. Corapcioglu, Eds.) p. 201. Martinus Nijhoff, Dordrecht (1984).
Ergun, S. *Chem. Eng. Prog.* **48**, 89 (1952).
Esterl, S., Debus, C., Nirschl, H., and Delgado, A., "ECCOMAS 98–4th Eur. Comput. Fluid Dyn. Conf." (K. D. Papailiou, Ed.), p. 692. John Wiley & Sons Ltd, New York (1998).
Fluent, User's Guide version 6.1.2, Fluent Inc., Lebanon, NH (2003).
Freund, H., Bauer, J., Zeiser, T., and Emig, G. *Ind. Eng. Chem. Res.* **44**, 6423 (2005).
Freund, H., Zeiser, T., Huber, F., Klemm, E., Brenner, G., Durst, F., and Emig, G. *Chem. Eng. Sci.* **58**, 903 (2003).
Georgiadis, J., Noble, D. R., Uchanski, M. R., and Buckius, R. O. *ASME J. Fluid Eng.* **118**, 434 (1996).
Giese, M., Rottschäfer, K., and Vortmeyer, D. *AIChE J.* **44**, 484 (1998).
Gladden, L. F., Mantle, M. D., and Sederman, A. J. *Adv. Chem. Eng.* **30**, 63 (2005).
Gladden, L. F. *AIChE J.* **49**, 2 (2003).
Guardo, A., Coussirat, M., Larrayoz, M. A., Recasens, F., and Egusquiza, E. *Ind. Eng. Chem. Res.* **43**, 7049 (2004).
Guardo, A., Coussirat, M., Larrayoz, M. A., Recasens, F., and Egusquiza, E. *Chem. Eng. Sci.* **60**, 1733 (2005).
Gunjal, P. R., Ranade, V. V., and Chaudhari, R. V. *AIChE J.* **51**, 365 (2005).
Harris, C. K., Roekaerts, D., Rosendal, F. J. J., Buitendijk, F. G. J., Daskopoulos, Ph., Vreenegoor, A. J. N., and Wang, H. *Chem. Eng. Sci.* **51**, 1569 (1996).
Hill, R. J., Koch, D. L., and Ladd, A. J. C. *J. Fluid Mech.* **448**, 213 (2001a).
Hill, R. J., Koch, D. L., and Ladd, A. J. C. *J. Fluid Mech.* **448**, 243 (2001b).
Hou, K., and Hughes, R. *Chem. Eng. Journal* **82**, 311 (2001).
Jakobsen, H. A., Lindborg, H., and Handeland, V. *Comput. Chem. Eng.* **26**, 333 (2002).
Jia, X., and Williams, R. A. *Powder Technology* **120**, 175 (2001).
Jiang, Y., Khadilkar, M. R., Al-Dahhan, M. H., and Dudukovic, M. P. *AIChE J.* **48**, 701 (2002).
Jolls, K. R., and Hanratty, T. J. *Chem. Eng. Sci.* **21**, 1185 (1966).
Kays, W. M. *J. Heat Transfer* **116**, 284 (1994).
Kim, S.-E., and Choudhury, D., in "Separated and Complex Flows", ASME FED vol. 217, p. 273. ASME, New York (1995).
Kingston, G., and Nunge, R. *Can. J. Chem. Eng.* **51**, 246 (1973).
Kuipers, J. A. M., and van Swaaij, W. P. M. *Adv. Chem. Eng.* **24**, 227 (1998).
Kutsovsky, Y. E., Scriven, L. E., Davis, H. T., and Hammer, B. E. *Phys. Fluids* **8**, 863 (1996).
Kvamsdal, H. M., Svendsen, H. F., and Hertzberg, T. *O. Olsvik. Chem. Eng. Sci.* **54**, 2697 (1999).
Lahbabi, A., and Chang, H. -C. *Chem. Eng. Sci.* **40**, 435 (1985).
Landon, V. G., Hebert, L. A., and Adams, C. B., in "Heat Transfer—Houston 1996 Proc. 31st National Heat Transfer Conference", p. 134. AIChE Symp. Ser., 1996.
Launder, B. E., and Spalding, D. B., "Lectures in Mathematical Models of Turbulence". Academic Press, London p. 1 (1972).
Launder, B. E., and Spalding, D. B. *Comp. Meth. Appl. Mech. Eng.* **3**, 269 (1974).
Larachi, F., Petre, C. F., Iliuta, I., and Grandjean, B. P. A. *Chem. Eng. & Process.* **42**, 535 (2003).
Latifi, M. A., Midoux, N., Storck, A., and Gence, J. N. *Chem. Eng. Sci.* **44**, 2501 (1989).
Lebon, L., Oger, L., Leblond, J., Hulin, J. P., Martys, N. S., and Schwartz, L. M. *Phys. Fluids* **8**, 293 (1996).
Leising, G., M.S. Thesis, Worcester Polytechnic Institute, Worcester, MA (2005).
Lerou, J. J., and Ng, K. M. *Chem. Eng. Sci.* **51**, 1595 (1996).
Liu, G., and Thompson, K. E. *Powder Technology* **113**, 185 (2000).
Lloyd, B., and Boehm, R. *Numerical Heat Transfer* **26**, 237 (1994).
Logtenberg, S. A., and Dixon, A. G. *Chem. Eng. & Process.* **37**, 7 (1998a).
Logtenberg, S. A., and Dixon, A. G. *Ind. Eng. Chem. Res.* **37**, 739 (1998b).
Logtenberg, S. A., Nijemeisland, M., and Dixon, A. G. *Chem. Eng. Sci.* **54**, 2433 (1999).

Lund, K. O., Nguyen, H., Lord, S. M., and Thompson, C. *Can. J. Chem. Eng.* **77**, 769 (1999).
Magnico, P. *Chem. Eng. Sci.* **58**, 5005 (2003).
Maier, R. S., Kroll, D. M., Bernard, R. S., Howington, S. E., Peters, J. F., and Davis, H. T. *Phys. Fluids* **15**, 3795 (2003).
Maier, R. S., Kroll, D. M., Kutsovsky, Y. E., Davis, H. T., and Bernard, R. S. *Phys. Fluids* **10**, 60 (1998).
Mansoorzadeh, S., Pain, C. C., De Oliveira, C. R. E., and Goddard, A. J. H. *Int. J. Numer. Meth. Fluids* **28**, 903 (1998).
Manz, B., Gladden, L. F., and Warren, P. B. *AIChE J.* **45**, 1845 (1999).
Mathur, S. R., and Murthy, J. Y. *Numerical Heat Transfer* **31**, 195 (1997).
McGreavy, C., Kam, E., Foumeny, E. A., Guidoum, A., and Ikponmwosa, A. N., in "2nd International Symposium on Application of Laser Anemometry to Fluid Mechanics", Lisbon, (1984).
McGreavy, C., Foumeny, E. A., and Javed, K. H. *Chem. Eng. Sci.* **41**, 787 (1986).
McKenna, T. F., Spitz, R., and Cokljat, D. *AIChE J.* **45**, 2392 (1999).
Mickley, H. S., Smith, K. A., and Korchak, E. I. *Chem. Eng. Sci.* **20**, 237 (1965).
Mueller, G. E. *Powder Technology* **92**, 179 (1997).
Mueller, G. E. *Powder Technology* **159**, 105 (2005).
Nandakumar, K., Shu, Y., and Chuang, K. T. *AIChE J.* **45**, 2286 (1999).
Nijemeisland, M., and Dixon, A. G. *Chem. Eng. J.* **82**, 231 (2001).
Nijemeisland, M., and Dixon, A. G. *AIChE J.* **50**, 906 (2004).
Nijemeisland, M., Dixon, A. G., and Stitt, E. H. *Chem. Eng. Sci.* **59**, 5185 (2004).
Nirschl, H., Dwyer, H. A., and Denk, V. *J. Fluid Mech.* **283**, 273 (1995).
Niven, R. K. *Chem. Eng. Sci.* **57**, 527 (2002).
Nolan, G. T., and Kavanagh, P. E. *Powder Technology* **72**, 149 (1992).
Nolan, G. T., and Kavanagh, P. E. *Powder Technology* **84**, 199 (1995).
Park, J., and Gibbs, S. J. *AIChE J.* **45**, 655 (1999).
Patankar, S. V., "Numerical Heat Transfer and Fluid Flow", p. 1 Hemisphere, Washington, D.C. (1980).
Pedernera, M. N., Piña, J., Borio, D. O., and Bucalá, V. *Chem. Eng. J.* **94**, 29 (2003).
Petre, C. F., Larachi, F., Iliuta, I., and Grandjean, B. P. A. *Chem. Eng. Sci.* **58**, 163 (2003).
Ranade, V., "Computational Flow Modeling for Chemical Reactor Engineering", p. 403 Academic Press, New York (2002).
Rashidi, M., Tompson, A., Kulp, T., and Peurrung, L. *J. Fluids Eng.* **118**, 470 (1996).
Ren, X., Stapf, S., and Blumich, B. *AIChE J.* **51**, 392 (2005).
Reyes, S. C., and Iglesia, E. *Chem. Eng. Sci.* **46**, 1089 (1991).
Ridler, D. E., and Twigg, M. V. Steam Reforming. pp. 225–282 in: Twigg, M. V. (Ed.), Catalyst Handbook (2nd Ed.) Manson Publishing, London, 1996.
Rode, S., Midoux, N., Latifi, M. A., Storck, A., and Saatdjian, E. *Chem. Eng. Sci.* **49**, 889 (1994).
Romkes, S. J. P., Dautzenberg, F. M., van den Bleek, C. M., and Calis, H. P. A. *Chem. Eng. J.* **96**, 3 (2003).
Schouten, E. P. S., Borman, P. C., and Westerterp, K. R. *Chem. Eng. Sci.* **49**, 4725 (1994).
Schuster, J., and Vortmeyer, D. *Chemie Ingenieur Technik* **53**, 806 (1981).
Sederman, A. J., Johns, M. L., Bramley, A. S., Alexander, P., and Gladden, L. F. *Chem. Eng. Sci.* **52**, 2239 (1997).
Sederman, A. J., Johns, M. L., Alexander, P., and Gladden, L. F. *Chem. Eng. Sci.* **53**, 2117 (1998).
Seguin, D., Montillet, A., and Comiti, J. *Chem. Eng. Sci.* **53**, 3751 (1998a).
Seguin, D., Montillet, A., Comiti, J., and Huet, F. *Chem. Eng. Sci.* **53**, 3897 (1998b).
Snyder, L. J., and Stewart, W. E. *AIChE J.* **12**, 167 (1966).
Soppe, W. *Powder Technology* **62**, 189 (1990).
Sørensen, J. P., and Stewart, W. E. *Chem. Eng. Sci.* **29**, 819 (1974).
Spedding, P. L., and Spencer, R. M. *Comput. Chem. Eng.* **19**, 43 (1995).

Stephenson, J. L., and Stewart, W. E. *Chem. Eng. Sci.* **41**, 2161 (1986).
Stevenson, P. *Chem. Eng. Sci.* **58**, 5379 (2003).
Stitt, E. H., pp. 185–216 *in* "Sustainable strategies for the upgrading of natural gas: fundamentals, challenges and opportunities" (Derouane, E., Parmon, V., Lemos, F. and Ramoa-Ribiero F., Eds.), NATO Science Series, Vol. 191, Springer, Dordrecht, Netherlands (2005).
Suekane, T., Yokouchi, Y., and Hirai, S. *AIChE J.* **49**, 10 (2003).
Taskin, E., Dixon, A. G., and Stitt, E. H., submitted to *Numerical Heat Transfer A* (2006).
Theuerkauf, J., Witt, P., and Schwesig, D. *Powder Technology* **165**, 92 (2006).
Thompson, K. E., and Fogler, H. S. *AIChE J.* **43**, 1377 (1997).
Tierney, M., Nasr, A., and Quarini, G. *Sep. Purif. Technol.* **13**, 97 (1998).
Tobiś, J. *Chem. Eng. Sci.* **55**, 5359 (2000).
Tobiś, J. *Chem. Eng. Comm.* **184**, 71 (2001).
Tobiś, J. *Ind. Eng. Chem. Res.* **41**, 2552 (2002).
Utyuzhnikov, S. V. *Computers & Fluids* **34**, 771 (2005).
Van Baten, J. M., Ellenberger, J., and Krishna, R. *Chem. Eng. Sci.* **56**, 813 (2001).
Van der Merwe, D. F., and Gauvin, W. H. *AIChE J.* **17**, 519 (1971).
Von Scala, C., Wehrli, M., and Gaiser, G. *Chem. Eng. Sci.* **54**, 1375 (1999).
Wegner, T. H., Karabelas, A. J., and Hanratty, T. J. *Chem. Eng. Sci.* **26**, 59 (1971).
Winterberg, M., Tsotsas, E., Krischke, A., and Vortmeyer, D. *Chem. Eng. Sci.* **55**, 967 (2000).
Yakhot, V., and Orszag, S. A. *J. of Sci. Comput.* **1**, 1 (1986).
Yang, A., Miller, C. T., and Turcoliver, L. D. *Phys. Rev. E.* **53**, 1516 (1996).
Yuen, E. H. L., Sederman, A. J., and F Gladden, L. *Appl. Catal. A.* **232**, 29 (2002).
Yuen, E. H. L., Sederman, A. J., Sani, F., Alexander, P., and Gladden, L. F. *Chem. Eng. Sci.* **58**, 603 (2003).
Zeiser, T., Lammers, P., Klemm, E., Li, Y. W., Bernsdorf, J., and Brenner, G. *Chem. Eng. Sci.* **56**, 1697 (2001).
Zeiser, T., Steven, M., Freund, H., Lammers, P., Brenner, G., Durst, F., and Bernsdorf, J. *Phil. Trans. R. Soc. Lond. A* **360**, 507 (2002).